CASED BOREHOLE EFFECT ON DOWNHOLE SEISMIC MEASUREMENTS

by

Chengbin Peng, C.H. Cheng, M.N. Toksöz, and Zhenya Zhu

Earth Resources Laboratory
Department of Earth, Atmospheric, and Planetary Sciences
Massachusetts Institute of Technology
Cambridge, MA 02139

ABSTRACT

Approximate and exact formulations are presented for the interaction of an incident wave with a cased borehole. In the approximate method, the borehole coupling theory is used to compute pressure in the fluid at a low frequency. The results are simple and explicit. They are useful in the study of cased borehole coupling and as well as borehole radiation. In the exact method, elastic potentials in each annulus are represented as a superposition of fundamental solutions to the Helmholtz equations. Continuity of displacements and stresses across layer boundaries are used to determine unknown coefficients. The global matrix method is employed to simultaneously compute these coefficients in individual layers. This method is advantageous over the Thomson-Haskell propagator matrix method in handling evanescent waves. Our results show that, in a cased borehole, the borehole effects on downhole seismic measurements are more significant than those in an open borehole, especially when the formation is soft and the casing is steel. For hard formations and frequency below 1 kHz, cased borehole influence on downhole geophone measurement is minimal, while at high frequencies, large discrepancies occur, especially at grazing incidence. For soft formations, both the pressure in the fluid and the solid displacement on the borehole wall show strong dependence on frequency and incidence angle, even at very low frequencies. Strong resonance occurs in the fluid for an SV incidence at angle $\delta = cos^{-1}\beta/C_T$ where C_T is the tube wave velocity in a cased borehole. This resonance is prominent even at a very high frequency and large incidence angle because the tube wave velocity is raised well above the formation shear velocity by the steel pipe. This behavior is very different from that in an open borehole. At a particular angle of incidence of a plane P wave, the pressure in the fluid is near zero at low frequencies. This angle is dependent on the casing thickness and can be computed exactly. In general the casing behaves like a shield in such a way that the amplitude of both pressure in the fluid and solid motion on the borehole wall are reduced compared to those in an open borehole.

INTRODUCTION

In VSP and crosshole surveys, measurements are made with geophones/hydrophones placed inside a fluid-filled borehole. Borehole coupling signifies the manner in which incident elastic waves are distorted by the fluid-filled cylinder, in both amplitude and phase as well as the properties of polarization. The coupling theory in an open borehole is extensively studied in the literature, especially in the low frequency limits (White, 1953, 1983; Schoenberg, 1986; Peng et al., 1992). White (1953) proposed a theory of borehole coupling at very long wavelength assumption. Schoenberg (1986) developed a complete theory for the interaction of a plane elastic wave with a fluid-filled borehole and gave explicit formulations at the low-frequency limit. It turns out that the formulation given by Schoenberg (1986) reduces to that of White (1953) as the frequency of an incident wave approaches to zero. Lee (1987) also independently derived the low frequency formulation of borehole coupling by applying the reciprocity relationships with respect to the borehole radiation. Results that are valid at high frequency are recently given by Blair (1984) and Lovell and Hornby (1990). They are applicable to the pressure measurement at the center of the borehole. Peng et al. (1992) presented a complete theory for all frequency and all azimuthally symmetric and nonsymmetric components.

However, the majority of boreholes drilled in industry are cased either by cements or by steel pipes or both, besides the mudcakes that are more or less always present. Borehole coupling in such a complicated environment is rarely studied. The distortion of the incident wave by the presence of radially layered casing and cement around a fluid-filled borehole is less understood. This paper is devoted to the cased borehole effect on a downhole seismic experiment by approximately and exactly solving the problem of an elastic wave impinging on a radially layered borehole.

This paper is organized into seven sections: The first section presents a general solution to the problem in terms of superposition of fundamental modes in a cylindrical coordinate. The second section gives a leading order analysis to the exact solution at a low frequency asymptotic approximation, where explicit expressions for the tube wave velocity and pressure in the cased borehole are derived. This analysis yields correct estimation of pressure in the fluid only at a normal incidence of a plane P wave incidence. In the third section, we develop a quasi-static approach to the borehole coupling in a cased borehole at a low frequency, where simple, explicit and accurate expressions are obtained. In the fourth section, the global matrix method is employed to exactly solve the general formulation developed in the first section. The fifth and sixth sections are devoted to high frequency behaviors of pressure in the fluid and solid displacement on the borehole wall, respectively, which have applications in many downhole experiments where data are collected for waves of higher and higher frequency (Albright and Johnson, 1990; Pratt et al., 1992). In the seventh section, a laboratory experiment is carried out to study the fluid resonance in a cased borehole due to a plane SV incidence in a

glass-cased soil borehole model.

GENERAL SOLUTION

Problems

Consider the case of an elastic plane wave incident on a radially layered borehole, as shown in Figure 1. In each radial layer, the formation is a homogeneous elastic medium with density ρ_m, compressional wave speed α_m and shear wave speed β_m, where m denotes the layer number with $1 \leq m \leq M+1$. M is the number of annuli between the borehole fluid and formation. The borehole is filled with a fluid that has density ρ_f and compressional wave speed α_f. The inner radius of the borehole is r_b where a downhole geophone is placed. The primary goal of this paper is to investigate the pressure in the fluid and the solid motion on the borehole wall due to an incident plane wave from the formation.

The fluid displacement $\vec{u}_f$ inside the borehole and the solid displacement $\vec{u}_m$ in the m-th layer satisfy the elastic wave equations, which, in terms of the corresponding potentials (Tubman et al., 1984; Schoenberg et al., 1981), are

$$\nabla^2\phi_f + \frac{\omega^2}{\alpha_f^2}\phi_f = 0,$$

and

$$\nabla^2\phi_m + \frac{\omega^2}{\alpha^2}\phi_m = 0,$$

$$\nabla^2\xi_m + \frac{\omega^2}{\beta^2}\xi_m = 0,$$

$$\nabla^2\psi_m + \frac{\omega^2}{\beta^2}\psi_m = 0.$$

The displacements and stress vectors are related to these potentials by

$$\vec{u}_f = \nabla\phi_f$$

$$\vec{u}_m = \nabla\phi_m + \nabla\times(\nabla\times(\xi_m\hat{e}_z)) + \nabla\times(\psi_m\hat{e}_z) \tag{1}$$

and

$$\sigma_{rr}^{(m)} = -\rho_m\omega^2\phi_m - 2\rho_m\beta_m^2\left[\left(\frac{1}{r}\frac{\partial\phi_m}{\partial r} + \frac{1}{r^2}\frac{\partial^2\phi_m}{\partial\theta^2} + \frac{\partial^2\phi_m}{\partial z^2}\right)\right.$$

$$+\frac{\partial}{\partial z}(\frac{\omega^2}{\beta_m^2}\xi_m+\frac{1}{r}\frac{\partial \xi_m}{\partial r}+\frac{1}{r^2}\frac{\partial^2\xi_m}{\partial\theta^2}+\frac{\partial^2\xi_m}{\partial z^2})+\frac{1}{r^2}\frac{\partial\psi_m}{\partial\theta}-\frac{1}{r}\frac{\partial^2\psi_m}{\partial r\partial\theta}]$$

$$\sigma_{r\theta}^{(m)} = 2\rho_m\beta_m^2[\frac{\partial}{\partial\theta}(\frac{1}{r}\frac{\partial\phi_m}{\partial r}-\frac{\phi_m}{r^2})+\frac{\partial^2}{\partial z\partial\theta}(\frac{1}{r}\frac{\partial\xi_m}{\partial r}-\frac{\xi_m}{r^2})$$
$$+\frac{1}{r^2}\frac{\partial^2\psi_m}{\partial\theta^2}+\frac{1}{r}\frac{\partial\psi_m}{\partial r}+\frac{1}{2}(\frac{\omega^2}{\beta_m^2}\psi_m+\frac{\partial^2\psi_m}{\partial z^2})]$$

$$\sigma_{rz}^{(m)} = 2\rho_m\beta_m^2[\frac{\partial^2\phi_m}{\partial r\partial z}+\frac{\partial}{\partial r}(\frac{\omega^2}{2\beta_m^2}\xi_m+\frac{\partial^2\xi_m}{\partial z^2})+\frac{1}{2r}\frac{\partial^2\psi_m}{\partial z\partial\theta}]$$

General Solutions

When an incident wave hits the outermost radial layer from the formation, some energy is reflected back and some is transmitted into the casing and cements. The general solution to the problem, in a cylindrical coordinate (r,θ,z) with θ the angle with respect to the azimuth of the incident wave, is

$$\phi_f = -\frac{\alpha_f V(\omega)}{\omega^2}[\,A_0\,J_0(k_f r)+2\sum_{n=1}^{\infty}i^n\,A_n\cos n\theta\,J_n(k_f r)\,]$$

$$\phi_m = -\frac{\alpha V(\omega)}{\omega^2}[\,E_0^{(m)}H_0^{(1)}(k_p{}^{(m)}r)+2\sum_{n=1}^{\infty}i^n\,E_n^{(m)}\cos n\theta\,H_n^{(1)}(k_p{}^{(m)}r)\,]$$
$$-\frac{\alpha V(\omega)}{\omega^2}[\,P_0^{(m)}H_0^{(2)}(k_p{}^{(m)}r)+2\sum_{n=1}^{\infty}i^n\,P_n^{(m)}\cos n\theta\,H_n^{(2)}(k_p{}^{(m)}r)\,]$$

$$\xi_m = -\frac{i\beta^2 V(\omega)}{\omega^3}[\,F_0^{(m)}H_0^{(1)}(k_s{}^{(m)}r)+2\sum_{n=1}^{\infty}i^n\,F_n^{(m)}\cos n\theta\,H_n^{(1)}(k_s{}^{(m)}r)\,]$$
$$-\frac{i\beta^2 V(\omega)}{\omega^3}[\,Q_0^{(m)}H_0^{(2)}(k_s{}^{(m)}r)+2\sum_{n=1}^{\infty}i^n\,Q_n^{(m)}\cos n\theta\,H_n^{(2)}(k_s{}^{(m)}r)\,]$$

$$\psi_m = -\frac{\beta V(\omega)}{\omega^2}[\,-G_0^{(m)}H_0^{(1)}(k_s{}^{(m)}r)-2\sum_{n=1}^{\infty}i^n\,G_n^{(m)}\cos n\theta\,H_n^{(1)}(k_s{}^{(m)}r)\,]$$
$$-\frac{\beta V(\omega)}{\omega^2}[\,-R_0^{(m)}H_0^{(2)}(k_s{}^{(m)}r)-2\sum_{n=1}^{\infty}i^n\,R_n^{(m)}\cos n\theta\,H_n^{(2)}(k_s{}^{(m)}r)\,] \qquad (2)$$

where the z and time dependence $e^{i(k_z z-\omega t)}$ is assumed. In these expressions, $k_f = \sqrt{\omega^2/\alpha_f^2-{k_z}^2}$, $k_p{}^{(m)}=\sqrt{\omega^2/\alpha_m^2-{k_z}^2}$ and $k_s{}^{(m)}=\sqrt{\omega^2/\beta_m^2-{k_z}^2}$, and signs of $k_f, k_p{}^{(m)}, k_s{}^{(m)}$ are chosen such that $Im(k_p{}^{(m)}, k_s{}^{(m)}, k_f)\geq 0$. $V(\omega)$ denotes the source function at a given frequency ω. $H_n^{(1)}(x)$ is the Hankel function of the first kind, representing energy traveling outward. $H_n^{(2)}(x)$ is the Hankel function of the second kind, representing energy traveling inward. $E_n^{(m)}, P_n^{(m)}, F_n^{(m)}, Q_n^{(m)}, G_n^{(m)}$ and $R_n^{(m)}$ are dimensionless, unknown constants in the m-th layer. A_n is that in the fluid. They are determined by satisfying boundary conditions.

Given the potentials in Eq. (2), the displacement and stress components are computed by equations in Eq. (1). Let $u_{r_n}^{(m)}$, for an example, denote the n-th harmonic component (mode n) in the complete expansion Eq. (2) in layer m (the borehole fluid column corresponds to m=0). The radial, tangential and vertical displacements $u_{r_n}^{(m)}$, $u_{\theta_n}^{(m)}$ and $u_{z_n}^{(m)}$ are

$$\begin{aligned} u_{r_n}^{(m)} = -\frac{V(\omega)}{\omega^2} \quad \{ \quad & [\, \mathcal{U}_{rn}^{\phi(1)}(r)\, E_n^{(m)} + \mathcal{U}_{rn}^{\phi(2)}(r)\, P_n^{(m)} \,] \cos n\theta \\ + \quad & [\, \mathcal{U}_{rn}^{\xi(1)}(r)\, F_n^{(m)} + \mathcal{U}_{rn}^{\xi(2)}(r)\, Q_n^{(m)} \,] \cos n\theta \\ + \quad & [\, \mathcal{U}_{rn}^{\psi(1)}(r)\, G_n^{(m)} + \mathcal{U}_{rn}^{\psi(2)}(r)\, R_n^{(m)} \,] \sin n\theta \ \} \end{aligned} \tag{3}$$

$$\begin{aligned} u_{\theta_n}^{(m)} = -\frac{V(\omega)}{\omega^2} \quad \{ \quad & [\, \mathcal{U}_{\theta n}^{\phi(1)}(r)\, E_n^{(m)} + \mathcal{U}_{\theta n}^{\phi(2)}(r)\, P_n^{(m)} \,] (-\sin n\theta) \\ + \quad & [\, \mathcal{U}_{\theta n}^{\xi(1)}(r)\, F_n^{(m)} + \mathcal{U}_{\theta n}^{\xi(2)}(r)\, Q_n^{(m)} \,] (-\sin n\theta) \\ + \quad & [\, \mathcal{U}_{rn}^{\psi(1)}(r)\, G_n^{(m)} + \mathcal{U}_{rn}^{\psi(2)}(r)\, R_n^{(m)} \,] \cos n\theta \ \} \end{aligned}$$

$$\begin{aligned} u_{z_n}^{(m)} = -\frac{V(\omega)}{\omega^2} \quad \{ \quad & [\, \mathcal{U}_{zn}^{\phi(1)}(r)\, E_n^{(m)} + \mathcal{U}_{zn}^{\phi(2)}(r)\, P_n^{(m)} \,] \cos n\theta \\ + \quad & [\, \mathcal{U}_{zn}^{\xi(1)}(r)\, F_n^{(m)} + \mathcal{U}_{zn}^{\xi(2)}(r)\, Q_n^{(m)} \,] \cos n\theta \ \} \end{aligned}$$

and the stresses on the surface where r is a constant are

$$\begin{aligned} \sigma_{rr_n}^{(m)} = -\frac{V(\omega)}{\omega^2} \quad \{ \quad & [\, \mathcal{R}_{\phi n}^{(1)}(r)\, E_n^{(m)} + \mathcal{R}_{\phi n}^{(2)}(r)\, P_n^{(m)} \,] \cos n\theta \\ + \quad & [\, \mathcal{R}_{\xi n}^{(1)}(r)\, F_n^{(m)} + \mathcal{R}_{\xi n}^{(2)}(r)\, Q_n^{(m)} \,] \cos n\theta \\ + \quad & [\, \mathcal{R}_{\psi n}^{(1)}(r)\, G_n^{(m)} + \mathcal{R}_{\psi n}^{(2)}(r)\, R_n^{(m)} \,] \sin n\theta \ \} \end{aligned} \tag{4}$$

$$\begin{aligned} \sigma_{r\theta_n}^{(m)} = -\frac{V(\omega)}{\omega^2} \quad \{ \quad & [\, \mathcal{T}_{\phi n}^{(1)}(r)\, E_n^{(m)} + \mathcal{T}_{\phi n}^{(2)}(r)\, P_n^{(m)} \,] (-\sin n\theta) \\ + \quad & [\, \mathcal{T}_{\xi n}^{(1)}(r)\, F_n^{(m)} + \mathcal{T}_{\xi n}^{(2)}(r)\, Q_n^{(m)} \,] (-\sin n\theta) \\ + \quad & [\, \mathcal{T}_{\psi n}^{(1)}(r)\, G_n^{(m)} + \mathcal{T}_{\psi n}^{(2)}(r)\, R_n^{(m)} \,] \cos n\theta \ \} \end{aligned}$$

$$\begin{aligned} \sigma_{rz_n}^{(m)} = -\frac{V(\omega)}{\omega^2} \quad \{ \quad & [\, \mathcal{Z}_{\phi n}^{(1)}(r)\, E_n^{(m)} + \mathcal{Z}_{\phi n}^{(2)}(r)\, P_n^{(m)} \,] \cos n\theta \\ + \quad & [\, \mathcal{Z}_{\xi n}^{(1)}(r)\, F_n^{(m)} + \mathcal{Z}_{\xi n}^{(2)}(r)\, Q_n^{(m)} \,] \cos n\theta \\ + \quad & [\, \mathcal{Z}_{\psi n}^{(1)}(r)\, G_n^{(m)} + \mathcal{Z}_{\psi n}^{(2)}(r)\, R_n^{(m)} \,] \sin n\theta \ \} \end{aligned}$$

where the details are given in Appendix A.

The boundary conditions for determining $A_n, E_n^{(m)}, P_n^{(m)}, F_n^{(m)}, Q_n^{(m)}, G_n^{(m)}$ and $R_n^{(m)}$ are the continuities of radial displacement and normal stress, and vanishing of tangential stresses at the fluid-solid interface, and the continuities of displacements and tractions at the solid-solid interfaces. In the outermost layer M + 1, i.e., the formation, $P_n^{(M+1)}, Q_n^{(M+1)}$ and $R_n^{(M+1)}$ are zero because of the radiation boundary condition at infinity. After the coefficients $A_n, E_n^{(m)}, P_n^{(m)}, F_n^{(m)}, Q_n^{(m)}, G_n^{(m)}$ and $R_n^{(m)}$ are known, the displacement on the borehole wall and pressure in the fluid can be easily computed from Eq. (3) and Eq. (4).

LOW FREQUENCY REGIME: A LEADING ORDER ANALYSIS

Pressure in the Fluid

At a low frequency, the mathematically involved expressions in the previous section can be greatly simplified. The pressure in the fluid is homogeneous across the borehole section and is related to the axial fluid motion v and the radial solid motion u_r by the equations of conservation of vertical momentum and the constitutive law (White, 1983)

$$\frac{\partial P}{\partial z} = \rho_f \omega^2 v, \tag{5}$$

and

$$P = -K_f\left(\frac{\partial v}{\partial z} + \frac{2u_r(r_b, z)}{r_b}\right) \tag{6}$$

where $K_f = \rho_f \alpha_f^2$ is the fluid bulk modulus and r_b the borehole radius.

Eliminating v in Eq. (5) and Eq. (6) results in, written in the time domain, the following equation

$$\frac{\partial^2 P}{\partial t^2} - \alpha_f^2 \frac{\partial^2 P}{\partial z^2} = 2\rho_f \alpha_f^2 \frac{\partial^2 \epsilon_r(r_b, z)}{\partial t^2} \tag{7}$$

where $\epsilon_r(r_b, z) = u_r(r_b, z)/r_b$ is the change of borehole radius, which acts like a source for pressure in the fluid-filled borehole.

Leading Order Analysis

Since only the symmetric mode $n = 0$ in Eq. (2) will contribute to pressure in the fluid at a low frequency (noting $J_0(x) \to 1$ and $J_n(x) \to 0$ as $x \to 0$). Assuming only one annulus is presented, we use the following approximation to the displacements in the

casing and the scattered displacements in the formation:

$$\begin{aligned} u_r^{(c)} &= C_1/r + C_2 r \log k_\beta r \\ u_z^{(c)} &= \frac{C_3}{ik_z} \log k_\beta r \end{aligned}$$

in the casing with $r_b \le r \le r_c$ where r_c is the outer radius of the casing, and

$$\begin{aligned} u_r^{(\infty)} &= D_1/r \\ u_z^{(\infty)} &= 0 \end{aligned}$$

in the formation with $r \ge r_c$. These expressions come directly from Eq. (3), where only the first two most singular terms in the asymptotic expansions of the Hankel functions $H_0^{(1,2)}(\cdot)$ and $H_1^{(1,2)}(\cdot)$ for a very small argument are kept. Here $k_\beta r$ is maintained to make the argument of the log function dimensionless. The $\log k_\beta r$ term in the formation is excluded because it diverges at ∞, which is an assumption we make in this leading order analysis.

The stresses are directly determined from the constitutive relationship between stress and strain and the geometric relationship between strain and displacement, yielding

$$\begin{aligned} \sigma_{rr}^{(c)} &= -2\mu_c \frac{C_1}{r^2} + [\, 2(\lambda_c + \mu_c)C_2 + \lambda_c C_3 \,] \log k_\beta r \\ \sigma_{rz}^{(c)} &= \mu_c [\, \frac{ik_z}{r}(C_1 - \frac{C_3}{k_z{}^2}) + ik_z\, r \log k_\beta r\, C_2 \,] \end{aligned}$$

in the casing, and

$$\begin{aligned} \sigma_{rr}^{(\infty)} &= -2\mu \frac{D_1}{r^2} \\ \sigma_{rz}^{(\infty)} &= ik_z\, \mu \frac{D_1}{r} \end{aligned}$$

in the formation.

Boundary Conditions

The boundary conditions to determine the unknown coefficients C_1, C_2, C_3 and D_1 are assumed to be

(i) $\sigma_{rr}^{(c)}(r_b^+) = -P$

(ii) $\sigma_{rr}^{(c)}(r_c^-) = \sigma_{rr}^{(\infty)}(r_c^+) + \sigma_{rr}^{(inc)}(r_c^+)$

(iii) $\sigma_{rz}^{(c)}(r_c^-) = \sigma_{rz}^{(\infty)}(r_c^+) + \sigma_{rz}^{(inc)}(r_c^+)$

$$\text{(iv)} \quad u_r^{(c)}(r_c^-) = u_r^{(\infty)}(r_c^+) + u_r^{(inc)}(r_c^+)$$

where the superscript (inc) denotes a quantity associated with the incident wave. P is the pressure in the fluid-filled borehole. The continuity of u_z at $r = r_c$ and vanishing of $\sigma_{rz}^{(c)}$ at $r = r_b$ are not imposed since they are less singular compared to the others as $\omega \to 0$, assuming $C_1 \neq 0$.

Pressure in the Borehole

The pressure in the fluid-filled borehole due to an incident wave in the formation, by solving the four equations associated with the boundary conditions above, is found to be

$$P = \frac{w(\lambda_c + 2\mu_c)\,[\,2\mu\, u_r^{(inc)}(r_c)/r_c + \sigma_{rr}^{(inc)}(r_c)\,]}{(\mu - \mu_c)(\lambda_c + \mu_c + w)\frac{r_b^2}{r_c^2} + (\mu_c - w)(\lambda_c + \mu_c + \mu)} \tag{8}$$

where $w = \rho_f \alpha_f^2/(\alpha_f^2 {k_z}^2/\omega^2 - 1)$. ω/k_z is the vertical phase velocity. It is interesting to note that, under the assumptions made in this section, $\sigma_{rz}^{(inc)}$ does not contribute to the pressure in the borehole. In general, the terms σ_{rr} and u_r are decoupled from σ_{rz} and u_z in the limit $\omega \to 0$ (Winbow, 1991). As will be shown later, Eq. (8) is accurate only at a normal incidence for an incident P wave, where $\sigma_{rz}^{(inc)} \approx 0$ and $u_z^{(inc)} \approx 0$, i.e., the assumptions are well justified.

Zero Frequency Tube Wave Velocity

The zero frequency tube wave velocity in a cased borehole is computed by letting the denominator in Eq. (8) vanish, which yields

$$C_T = \frac{\alpha_f}{\sqrt{1 + \rho_f \alpha_f^2/W}} \tag{9}$$

where

$$W = \mu_c \frac{\mu + (\mu_c - \mu)(1 - \gamma_c)(1 - \frac{r_b^2}{r_c^2})}{\mu_c - (\mu_c - \mu)\gamma_c(1 - \frac{r_b^2}{r_c^2})}, \tag{10}$$

is the effective modulus of a cased borehole. Here $\gamma_c = \beta_c^2/\alpha_c^2$. This expression is identical with those of Marzzeta and Shoenberg (1985) and Norris (1990). It turns out that Eq. (9) is extremely accurate in estimating the tube wave velocity in a cased borehole. Table 1 shows a comparison of the tube wave velocities computed by Eq. (9) and by the exact formulation given in the latter section at 1 Hz.

Table 1: Tube wave velocity in cased and open boreholes (the inner radius is 10.16 cm, the outer radius is 12.09 cm; the fluid is water with compressional velocity 1500 m/s and density 1000 kg/m^3; the casing is steel with $\alpha_c = 6100\ m/s$, $\beta_c = 3350\ m/s$ and $\rho_c = 7500\ kg/m^3$)

				C_T in an open borehole		C_T in a cased borehole	
Lithology	α	β	ρ	by (9)	exact at 1 Hz	by (9)	exact at 1 Hz
Pierre Shale	2074	869	2000	950.634	950.636	1425.701	1425.706
Berea Sandstone	4206	2664	2140	1399.884	1399.885	1450.390	1450.392
Limestone	5970	2880	2656	1428.809	1428.809	1457.314	1457.317
Soil	1670	170	1290	191.503	191.499	1421.411	1421.401

Plane P wave Incidence

For an incident compressional plane wave, we have (Peng et al., 1992)

$$u_r^{(p)} = -\alpha\ k_p\ J_1(k_p r)$$

$$u_z^{(p)} = \alpha\ ik_z\ J_0(k_p r)$$

$$\sigma_{rr}^{(p)} = -\rho\alpha[\ (\omega^2 - 2\beta^2 {k_z}^2) J_0(k_p r) - 2\beta^2 k_p \frac{1}{r} J_1(k_p r)\ ]$$

and

$$\sigma_{rz}^{(p)} = -\rho\alpha[\ 2\beta^2\ ik_z\ k_p\ J_1(k_p r)\ ]$$

Therefore, it is easy to show that

$$2\mu\ u_r^{(inc)}(r_c)/r_c + \sigma_{rr}^{(inc)}(r_c) = P_0\ (\ 1 - 2\beta^2/\alpha^2 \cos^2\delta\ )$$

where $P_0 = -\rho\alpha\omega^2$ is proportional to the pressure of the incident P wave if no borehole exists. Substituting this expression in Eq. (8) yields the pressure in the fluid, scaled by P_0, as

$$\frac{P}{P_0} = \frac{1 - C_T^2/\alpha_f^2}{1 - (\frac{\beta_c^2}{\alpha_c^2} - \frac{\rho}{\rho_c}\frac{\beta^2}{\alpha_c^2})\,(1 - \frac{r_b^2}{r_c^2})}\ \frac{1 - 2\beta^2/\alpha^2\cos^2\delta}{1 - C_T^2/\alpha^2\cos^2\delta} \tag{11}$$

where, as a reminder, C_T is the tube wave velocity, δ is the angle of incidence. Comparing with the result given by White (1983) for an open borehole, we find that, in a cased borehole, the dependence of the fluid pressure on angle of incidence has the same form as that in an open borehole. The existence of casing modifies the amplitude and

the tube wave velocity. Actually, when $\alpha_c = \alpha$, $\beta_c = \beta$ and $\rho_c = \rho$, or $r_b = r_c$, i.e, the casing diminishes, Eq. (11) reduces to

$$\frac{P}{P_0} = \frac{\rho_f C_T^2}{\rho \beta^2} \frac{1 - 2\beta^2/\alpha^2 \cos^2 \delta}{1 - C_T^2/\alpha^2 \cos^2 \delta}, \tag{12}$$

the pressure in an open borehole caused by an incident compressional plane wave (White, 1953, 1983; Lovell and Hornby, 1990).

Figure 2a plots the pressure in the fluid as a function of the incident angle for a plane P wave. The pressures are computed both by Eq. (11) (referred to as *approximation* in the figure) and by the exact solution given in the latter sections (referred to as *exact* in the figure). The exact solution is computed for a frequency at 1 Hz. The formation is Berea sandstone (hard). The parameters are listed on the top of the figure. Only pressures in a cased borehole are shown, since, in an open borehole, the pressure computed by Eq. (11) agrees exactly with that by the complete solution. It is obvious that, in a cased borehole, agreement between the approximation and the exact only prevails at a normal incidence where $k_z = 0$. This has been pointed out previously. Generally in a cased borehole, Eq. (11) overestimates the pressure in the fluid.

Figure 2b plots the pressure in the fluid for the soft formation (Pierre shale). In this case, the discrepancy between Eq. (11) and the exact solution is significant. An exception occurs at a normal incidence where, again, the *approximation* agrees with the *exact*.

In a borehole with steel casing, the pressure in the fluid is significantly affected by the casing. At a particular angle of incidence, there will be no pressure in the fluid for an incident P wave, as is shown by the *exact* solution. This is because, in this case, there is no net change of the borehole cross section and the fluid is not squeezed at all. The particular incidence angle can be exactly estimated by the analysis given in the next section.

Plane SV wave Incidence

For an incident plane SV wave, we have (Peng et al., 1992)

$$u_r^{(sv)} = \beta \; k_z \; J_1(k_s r)$$

$$u_z^{(sv)} = \beta \; ik_s \; J_0(k_s r)$$

$$\sigma_{rr}^{(sv)} = 2\rho \; \beta^3 \; k_z k_s \; [J_0(k_s r) - \frac{1}{k_s r} J_1(k_s r) \;]$$

and

$$\sigma_{rz}^{(sv)} = -i\ \rho\beta^3\ ({k_s}^2 - {k_z}^2) J_1(k_s r)\ ]$$

. Then, simple substitution into Eq. (8) leads to

$$2\mu\ u_r^{(inc)}(r_c)/r_c + \sigma_{rr}^{(inc)}(r_c) = P_0\ \sin\delta\cos\delta$$

where $P_0 = \rho\beta$. In this case, the pressure in the fluid, scaled by P_0, is found to be

$$\frac{P}{P_0} = \frac{1 - C_T^2/\alpha_f^2}{1 - (\frac{\beta_c^2}{\alpha_c^2} - \frac{\rho}{\rho_c}\frac{\beta^2}{\alpha_c^2})\,(1 - \frac{r_b^2}{r_c^2})}\ \ \frac{\sin 2\delta}{1 - C_T^2/\beta^2\cos^2\delta} \tag{13}$$

which has the same amplitude factor as Eq. (11) and exhibits a familiar dependence on the angle of incidence. When the casing ceases to exist, i.e., either $\alpha_c = \alpha$, $\beta_c = \beta$ and $\rho_c = \rho$ or $r_b = r_c$, Eq. (13) reduces to

$$\frac{P}{P_0} = \frac{\rho_f C_T^2}{\rho\beta^2}\ \ \frac{\sin 2\delta}{1 - C_T^2/\beta^2\cos^2\delta}, \tag{14}$$

the pressure in an open borehole caused by an incident plane SV wave (White, 1953, 1983; Lovell and Hornby, 1990).

In Figure 3, we plot the pressure in a cased borehole computed by both Eq. (13) and the exact solution (at 1 Hz). The incident wave is a plane SV wave. The formation is either hard (Berea sandstone) or soft (Pierre shale). The difference between the *approximation* and the *exact* is evident, especially in a soft formation. At both the normal and grazing incidences, the *approximation* and *exact* turn out to be the same and are zero. We find that Eq. (13) underestimates the pressure in the fluid by a constant factor independent of the angle of incidence. Also evidently, there is a fluid resonance at incidence angle $\delta = \cos^{-1}\beta/C_T$ in the soft formation, where the tube wave is excited in the fluid.

Summary

The leading order analysis presented in this section yields correct estimation of pressure in the fluid in an open borehole. In a cased borehole, the estimation of pressure is only accurate for a P wave at a normal incidence and an S wave at both normal and grazing incidences. This analysis also leads to an accurate estimation of low frequency tube wave velocity in both open and cased boreholes. Yet, the approach is not accurate for both the P wave and the S wave at an oblique incidence. This is because the continuities of vertical displacement u_z and shear stress σ_{rz} across the casing-formation boundary are not satisfied.

LOW FREQUENCY REGIME: A QUASI-STATIC APPROACH

In this section, we give a quasi-static approach to the theory of borehole coupling in a cased borehole. Superior to the previous analysis, this approach has a profound physical insight to the interaction of a fluid-filled borehole with the formation. Furthermore, it yields simple and explicit formula for the pressure in the cased borehole at a low frequency, where analytical solutions are of little use and the numerical solution is too cumbersome. The results given in this section can be as well applied to study the radiation of an air gun source in a cased borehole, using the reciprocity relationships.

Borehole Coupling Equation

The $\epsilon_r(r_b, z)$ in Eq. (7) can be decomposed into two parts:

$$\epsilon_r(r_b, z) = (\frac{\bar{u}_r(r_b, z)}{r_b})^{(inc)} - \frac{P}{2W}$$

where the first term on the right-hand side is the deformation of an empty borehole due to an incident wave from the formation, the second term is the fluid resistance against borehole deformation (White, 1983). W is the effective modulus of a cased borehole given in Eq. (10). The $\bar{u}_r$ in the above equation is the azimuthal average of the radial displacement on the borehole wall, representing net change of the borehole cross section. An alternative form of Eq. (7) will be

$$\frac{1}{C_T^2}\frac{\partial^2 P}{\partial t^2} - \frac{\partial^2 P}{\partial z^2} = 2\rho_f \frac{\partial^2 \epsilon_r^{(inc)}(z)}{\partial t^2} \tag{15}$$

where $\epsilon_r^{(inc)}(z) = (\bar{u}_r(r_b, z)/r_b)^{(inc)}$ is called the borehole squeeze strain. The definition is different from that of Marzetta (1992) by a factor of 2. Eq. (15) is also referred to as the *borehole coupling equation.* It should be pointed out that the borehole squeeze strain is different from the radial strain $\partial u_r/\partial r$ on the borehole wall, rather it is the average change of cross section when an incident wave impinges on an *empty* borehole.

If $\epsilon_r^{(inc)}$ is known, the pressure in the fluid can be determined by

$$P(z, \omega) = -\rho_f \omega^2 \int_{-\infty}^{\infty} \epsilon_r^{(inc)}(z') \frac{i}{k_T} e^{-ik_T|z-z'|} dz'$$

where $k_T = \omega/C_T$ is the wavenumber of a tube wave. For an incident plane wave, the z dependence can be assumed to be $e^{ik_z z}$ where k_z is the vertical wavenumber. Then the above equation, neglecting terms associated with energy coming from infinity, yields

$$P(z, \omega) = 2\rho_f \omega^2 \frac{\epsilon_r^{(inc)}(z)}{{k_z}^2 - k_T^2}\,. \tag{16}$$

Borehole Squeeze Strain

The borehole squeeze strain is the azimuthally averaged radial displacement on the wall divided by the radius, i.e.,

$$\epsilon_r^{(inc)} = \frac{1}{2\pi}\int_0^{2\pi} u_r(r_b,\theta,z)d\theta \;/\; r_b \;.$$

It depends only on the net change of borehole section, not the details of deformation. In the case where the borehole deformation is equivoluminal, i.e., $\epsilon_r^{(inc)} = 0$, Eq. (16) implies that no pressure will be set up in the fluid-filled borehole.

To determine the borehole squeeze strain, we need to compute the average change in borehole radius for an empty borehole. A quasi-static approach will be adopted here, which is in line with the method used by White (1983) for an open borehole.

As the frequency $\omega \to 0$, the wavelength becomes much larger than the size of the borehole. In a vicinity around the borehole that is much larger than the borehole radius and at the same time much smaller than the wavelength, the stresses are nearly homogeneous and equal to those of the incident wave. Introduction of a cased borehole only locally disturbs the stress field at the expense of borehole deformation. The volume change of the borehole sets up a pressure inside the fluid in the same way as a piston source does. In an open borehole, the change of borehole radius due to an incident wave is easily calculated by the known results (White, 1983). In a cased borehole, extra work is needed to derive the effective moduli in a radially layered setting. In Appendix C, we give a derivation of the borehole squeeze strain by using the Airy function method in static elasticity, and the result is

$$\epsilon_r^{(inc)} = \frac{\sigma_{xx}+\sigma_{yy}}{E_{\|}} - \frac{\nu\sigma_{zz}}{E_{\perp}} \tag{17}$$

where σ_{xx}, σ_{yy} and σ_{zz} are the principal stresses of an incident wave. $E_{\|}$ is the effective modulus of the cased borehole against horizontal deformation, and is given by

$$E_{\|} = \frac{E}{1+(\zeta-1)\nu}\left[\,1+(\frac{\mu_c}{\mu}-1)(1-\gamma_c)(1-\frac{r_b^2}{r_c^2})\,\right]$$

and $E_{\perp}$ is the effective modulus of the cased borehole against vertical deformation, and is given by

$$E_{\perp} = \frac{E}{1+(\zeta-1)\nu^{-1}}\left[\,1+(\frac{\mu_c}{\mu}-1)(1-\gamma_c)(1-\frac{r_b^2}{r_c^2})\,\right]$$

where

$$\zeta = 1+\frac{\nu_c}{2(1-\nu_c)}\,(\frac{\mu_c}{\mu}-1)\,(1-\frac{r_b^2}{r_c^2})\;.$$

In these equations, E and ν are the Young's modulus and the Poisson ratio in the formation; E_c and ν_c are the Young's modulus and the Poisson ratio in the casing. As a reminder, $\gamma_c = \beta_c^2/\alpha_c^2$, r_b is the inner radius of the casing and r_c is the outer radius of the casing. In the case $r_b = r_c$ or $E_c = E$ and $\nu_c = \nu$, $E_\parallel$ and $E_\perp$ reduce to E, the Young's modulus in the formation. In this case, Eq. (17) is identical with that given by White (1983).

Figures 4 and 5 show the effective moduli of a cased borehole as a function of the casing thickness $(r_c - r_b)/r_b$ for the hard and soft formations, respectively. Evidently, $E_\perp \leq E_\parallel$ when the casing is harder than the formation. This implies that the cased borehole is stronger horizontally than vertically. $E_\parallel$ increases rapidly with the increase of casing thickness, while $E_\perp$ decreases slowly in the hard formation and increases slowly in the soft formation.

Figure 6 shows the effective moduli of a cased borehole as a function of the formation rigidity μ. The formation is assumed to be the Poisson's solid. As the formation becomes harder, $E_\parallel$ decreases rapidly, while $E_\perp$ is almost unchanged.

Plane P Wave Incidence

From Eq. (16) and Eq. (17), using the principal stresses σ_{xx}, σ_{yy} and σ_{zz} given by White (1983), we obtain, for an incident compressional plane wave,

$$\frac{P}{P_0} = \frac{\rho_f C_T^2}{\rho\beta^2} \frac{E}{(1-\nu^2)E_\perp} \frac{\eta[\,1-(1-2\nu)\cos^2\delta\,] - \nu[\,\nu+(1-2\nu)\cos^2\delta\,]}{1 - C_T^2/\alpha^2\cos^2\delta} \tag{18}$$

where P is the pressure in a cased borehole. $\eta = E_\perp/E_\parallel$ is the ratio of the horizontal and vertical effective moduli. When the casing thickness vanishes or its physical properties are the same as the formation, this equation reduces exactly to Eq. (12), the pressure in an open borehole.

A particular angle of incidence exists where the pressure in the fluid vanishes if

$$\eta < \frac{1-\nu}{2},$$

and this angle δ_0 is given by

$$\delta_0 = \cos^{-1}\sqrt{\frac{\eta-\nu^2}{(\eta+\nu)(1-2\nu)}} \tag{19}$$

at which there is no change of borehole cross section due to the passage of an incident P wave. In this case, the casing acts like a shield such that a hydrophone cannot see

the incident compressional wave. For the hard formation (Berea sandstone) with steel casing, this angle occurs at $\delta_0 = 8.64^o$; for the soft formation (Pierre shale), it is at $\delta_0 = 35.67^o$, where $r_b = 0.1016\ m$ and $r_c = 0.1219\ m$ are used. These estimations agree with the exact solutions shown in Figure 2.

The critical thickness $h_c = r_c - r_b$ is given by

$$r_b/r_c = \sqrt{1 - \frac{2\nu(1-\nu_c)}{\nu_c(1-2\nu)}\frac{\mu}{\mu_c - \mu}}$$

below which the shielding effect disappears. If $h \ll r_b$, the above equation can be simplified as

$$h_c/r_b = \frac{\nu(1-\nu_c)}{\nu_c(1-2\nu)}\frac{\mu}{\mu_c - \mu}\ .$$

As examples, taking the formation to be Berea sandstone and casing to be steel with the same geometry as in Figure 2, the above analysis yields a critical casing thickness $h_c = 0.1731\ r_b$, beyond which there is an angle δ_0 given by Eq. (19) where the pressure in the fluid vanishes for an incident P wave. In the case where the formation is Pierre shale, the critical thickness is $h_c = 0.0978\ r_b$. These estimations have been confirmed by solving the exact equations given in the next section. It is interesting to note that the critical thickness is smaller in the soft formation than in the hard formation, implying the shielding effect occurs easily in a cased borehole with a soft formation.

The following two examples are to show that Eq. (18) agrees with the exact solution at a low frequency at all angles of incidence. Figure 7 shows two calculations for the hard formation and the P wave incidence: the left one is by the exact method at 1 Hz, the right one is by Eq. (18). These two calculations are indistinguishable. They both show a zero of pressure in the fluid at 8.6^o. Figure 8 is the same as that in Figure 7 except for the soft formation. Again, one cannot tell the difference between the exact solution and the quasi-static approximation. They both show a zero at $\delta = 35.7^o$.

Plane S Wave Incidence

The pressure in a cased borehole due to an incidence plane SV wave will be

$$\frac{P}{P_0} = \frac{\rho_f C_T^2}{\rho\beta^2}\ \frac{(\eta+\nu)E}{(1+\nu)E_\perp}\ \frac{\sin 2\delta}{1 - C_T^2/\beta^2\cos^2\delta} \tag{20}$$

where P is the pressure in the fluid. When the casing diminishes, Eq. (20) reduces to the Eq. (13) in an open borehole.

Figures 9 and 10 show the pressures in the fluid for both the hard and the soft formations. The incident wave is a plane SV wave. The plot on the left is calculated

by the exact solution at 1 Hz. The plot on the right is computed by Eq. (20). No discrepancies can be identified, as expected. For the hard formation, the pressure has a lobe around 45^o. For the soft formation, strong fluid resonance occurs at 54^o for the SV incidence.

Summary

The quasi-static approach given in this section yields correct estimation of pressure in the fluid-filled borehole due to a source in the formation, both for cased and open boreholes. The resulting equations are simple and explicit. They can be used in the study of cased borehole coupling and radiation. Yet, the approach is accurate only at low frequencies. At high frequencies, complete solution must be sought and is given in the following section.

EXACT SOLUTION BY THE GLOBAL MATRIX METHOD

Displacement-Stress Vector

For a fixed harmonic component or mode n in Eq. (2), the displacement-stress vector $\vec{\mathrm{b}}_n^{(m)}(r)$ in layer m and at position r is related to the unknown coefficient vector $\vec{\mathrm{c}}_n^{(m)}$ by

$$\vec{\mathrm{b}}_n^{(m)}(r) = \mathrm{D}_n^{(m)}(r)\, \vec{\mathrm{c}}_n^{(m)} \tag{21}$$

where

$$\vec{\mathrm{b}}_n^{(m)}(r) = \begin{pmatrix} u_{r_n}^{(m)} \\ u_{\theta_n}^{(m)} \\ u_{z_n}^{(m)} \\ \sigma_{rr_n}^{(m)} \\ \sigma_{r\theta_n}^{(m)} \\ \sigma_{rz_n}^{(m)} \end{pmatrix} (r)$$

and

$$\vec{\mathrm{c}}_n^{(m)} = \begin{pmatrix} E_n^{(m)} \\ P_n^{(m)} \\ F_n^{(m)} \\ Q_n^{(m)} \\ G_n^{(m)} \\ R_n^{(m)} \end{pmatrix}.$$

The coefficient matrix $\mathrm{D}_n^{(m)}(r)$ is given in Appendix A. As a reminder, the superscript (m) is the layer index and the subscript n is the harmonic mode number.

Boundary Conditions

The boundary conditions at the interface between radial layer i and $i+1$ require that the displacements and stresses be continuous, i.e.,

$$\vec{\mathrm{b}}_n^{(i)}(r_{i+1}) = \vec{\mathrm{b}}_n^{(i+1)}(r_{i+1}) \tag{22}$$

when both sides are solids, or the normal stresses and displacements are continuous and the tangential stresses vanish when either side is a fluid, e.g., at $r = r_b$,

$$\mathrm{S}\,\vec{\mathrm{b}}_n^{(1)}(r_b) = \begin{bmatrix} u_{r_n}^f(r_b) \\ -p_n^f(r_b) \\ 0 \\ 0 \end{bmatrix} = \vec{\mathrm{f}}\,A_n \tag{23}$$

where $u_{r_n}^f$ and p_n^f are the radial displacement and pressure inside the fluid, respectively. S is an index matrix defined as

$$\mathrm{S} = \begin{bmatrix} 1 & 0 & 0 & 0 & 0 & 0 \\ 0 & 0 & 0 & 1 & 0 & 0 \\ 0 & 0 & 0 & 0 & 1 & 0 \\ 0 & 0 & 0 & 0 & 0 & 1 \end{bmatrix}_{4\times 6}$$

and $\vec{\mathrm{f}} = (\alpha_f k_f J_n'(k_f r_b), -\rho_f \alpha_f \omega^2 J_n(k_f r_b), 0, 0)^T$. In Eq. (23), A_n is the unknown coefficient in the fluid displacement potential.

At the outermost layer $i = M+1$, radiation conditions must be satisfied for a source free problem, i.e.,

$$P_n^{(M+1)} = Q_n^{(M+1)} = R_n^{(M+1)} = 0$$

such that no energy comes from infinity.

Propagator Matrix Method

Let

$$\vec{\mathrm{w}}_n(r) = \begin{bmatrix} u_{r_n}^{(inc)} \\ u_{\theta_n}^{(inc)} \\ u_{z_n}^{(inc)} \\ \sigma_{rr_n}^{(inc)} \\ \sigma_{r\theta_n}^{(inc)} \\ \sigma_{rz_n}^{(inc)} \end{bmatrix}(r)$$

be the displacement-stress vector of an incident plane wave from the formation (i.e., $r \geq r_{M+1}$). For a plane wave of either P, SV, or SV type, this vector is explicitly given in Appendix B.

The boundary condition at $r = r_{M+1}$ can be written as

$$\mathrm{D}_n^{(M+1)}(r_{M+1})\vec{\mathrm{c}}_n^{(M+1)} + \vec{\mathrm{w}}_n(r_{M+1}) = \mathrm{D}_n^{(M)}(r_{M+1})\vec{\mathrm{c}}_n^{(M)}. \tag{24}$$

While at an interior interface $r = r_i$, assuming the casing layers are well-bonded to each other, we have

$$\mathrm{D}_n^{(i)}(r_i)\vec{\mathrm{c}}_n^{(i)} = \mathrm{D}_n^{(i-1)}(r_i)\vec{\mathrm{c}}_n^{(i-1)} \tag{25}$$

for $2 \leq i \leq M$.

By recursively applying Eq. (24) and Eq. (25), we obtain

$$\mathrm{D}_n^{(1)}(r_b)\vec{\mathrm{c}}_n^{(1)} = \mathrm{G}_n\,[\,\mathrm{D}_n^{(M+1)}(r_{M+1})\vec{\mathrm{c}}_n^{(M+1)} + \vec{\mathrm{w}}_n(r_{M+1})\,] \tag{26}$$

which relates the wave fields at the borehole wall ($r = r_b$) with those in the formation $r = r_{M+1}$, where

$$\mathrm{G}_n = \Pi_{i=1}^{M}\mathrm{D}_n^{(i)}(r_i)[\mathrm{D}_n^{(i)}(r_{i+1})]^{-1}$$

is a matrix that propagates energy across boundaries.

The coupling of energy into the borehole fluid is accomplished by substituting Eq. (26) into the fluid-solid boundary condition Eq. (23) at $r = r_b$, yielding

$$\mathrm{S}\,\mathrm{G}_n\,[\,\mathrm{D}_n^{(M+1)}(r_{M+1})\vec{\mathrm{c}}_n^{(M+1)} + \vec{\mathrm{w}}_n(r_{M+1})\,] = \vec{\mathrm{f}}\,A_n$$

from which, in addition to the radiation condition in the outermost layer, the coefficients A_n, $E_n^{(M+1)}$, $F_n^{(M+1)}$ and $G_n^{(M+1)}$ can be solved. This equation can be further simplified as

$$\vec{\mathrm{f}}_E\,E_n^{(M+1)} + \vec{\mathrm{f}}_F\,F_n^{(M+1)} + \vec{\mathrm{f}}_G\,G_n^{(M+1)} + \vec{\mathrm{f}}_w = \vec{\mathrm{f}}\,A_n \tag{27}$$

where

$$\vec{\mathrm{f}}_w = \begin{bmatrix} (\mathrm{G}_n)_{1i}\,(\vec{\mathrm{w}}_n)_i \\ (\mathrm{G}_n)_{4i}\,(\vec{\mathrm{w}}_n)_i \\ (\mathrm{G}_n)_{5i}\,(\vec{\mathrm{w}}_n)_i \\ (\mathrm{G}_n)_{6i}\,(\vec{\mathrm{w}}_n)_i \end{bmatrix} (r_{M+1})$$

$$\vec{\mathrm{f}}_E = \begin{bmatrix} (\mathrm{G}_n)_{1i}\,(\mathrm{D}_n^{(M+1)})_{i1} \\ (\mathrm{G}_n)_{4i}\,(\mathrm{D}_n^{(M+1)})_{i1} \\ (\mathrm{G}_n)_{5i}\,(\mathrm{D}_n^{(M+1)})_{i1} \\ (\mathrm{G}_n)_{6i}\,(\mathrm{D}_n^{(M+1)})_{i1} \end{bmatrix} (r_{M+1})$$

$$\vec{\mathrm{f}}_F = \begin{bmatrix} (\mathrm{G}_n)_{1i}\,(\mathrm{D}_n^{(\mathrm{M}+1)})_{i3} \\ (\mathrm{G}_n)_{4i}\,(\mathrm{D}_n^{(\mathrm{M}+1)})_{i3} \\ (\mathrm{G}_n)_{5i}\,(\mathrm{D}_n^{(\mathrm{M}+1)})_{i3} \\ (\mathrm{G}_n)_{6i}\,(\mathrm{D}_n^{(\mathrm{M}+1)})_{i3} \end{bmatrix} (r_{\mathrm{M}+1})$$

and

$$\vec{\mathrm{f}}_G = \begin{bmatrix} (\mathrm{G}_n)_{1i}\,(\mathrm{D}_n^{(\mathrm{M}+1)})_{i5} \\ (\mathrm{G}_n)_{4i}\,(\mathrm{D}_n^{(\mathrm{M}+1)})_{i5} \\ (\mathrm{G}_n)_{5i}\,(\mathrm{D}_n^{(\mathrm{M}+1)})_{i5} \\ (\mathrm{G}_n)_{6i}\,(\mathrm{D}_n^{(\mathrm{M}+1)})_{i5} \end{bmatrix} (r_{\mathrm{M}+1})\ .$$

In the intermediate layers, a solution can be obtained by recursively applying Eq. (24) and Eq. (25) in a backward matching fashion.

As in any integral transform method to solve the elastic wave equation in a layered medium, instability and loss of accuracy are problematic when the vertical number k_z exceeds the medium wavenumbers such that the radial wavenumbers become imaginary. In this case, the wave field is evanescent. The matrix equation involves both negative and positive exponentials. Theoretically terms having positive exponentials exactly cancel each other, but numerically this never happens (Dunkin, 1965). The Thomson-Haskell type propagator matrix method described here has a block bidiagonal form in nature and is a two-point shooting algorithm (Chin et al., 1984). This technique is difficult to handle this type of instability (Schmidt and Tango, 1986). On the other hand, the global matrix method proposed by Chin et al. (1984) is well suited to this problem.

Global Matrix Method

We adopt a special kind of the global matrix method to solve A_n, $E_n^{(1)}$, $P_n^{(1)}$, $F_n^{(1)}$, $Q_n^{(1)}$, $G_n^{(1)}$ and $R_n^{(1)}$, which are coefficients needed to compute pressure in the fluid and wall displacement in the casing. The pressure yields a hydrophone output, and the wall displacement is measured by a downhole geophone.

The starting equations for this method are

$$\mathrm{B}_0\mathrm{D}_n^{(1)}(r_b)\vec{\mathrm{c}}_n^{(1)} = \mathrm{B}_0\mathrm{G}_n\mathrm{B}_0^{-1}\left[\,\mathrm{B}_0\,\mathrm{D}_n^{(\mathrm{M}+1)}(r_{\mathrm{M}+1})\,\vec{\mathrm{c}}_n^{(\mathrm{M}+1)} + \mathrm{B}_0\,\vec{\mathrm{w}}_n(r_{\mathrm{M}+1})\,\right] \tag{28}$$

and

$$\mathrm{b}_0\mathrm{S}\,\mathrm{D}_n^{(1)}(r_b)\vec{\mathrm{c}}_n^{(1)} = \mathrm{b}_0\vec{\mathrm{f}}\,A_n \tag{29}$$

where Eq. (23) and Eq. (26) have been used, and where

$$\mathrm{b}_0 = \begin{pmatrix} (\mathrm{B}_0)_{11} & & & \\ & (\mathrm{B}_0)_{44} & & \\ & & (\mathrm{B}_0)_{55} & \\ & & & (\mathrm{B}_0)_{66} \end{pmatrix}_{4\times 4}$$

and

$$\mathrm{B}_0 = \begin{pmatrix} \frac{1}{\lambda_1} & & & & & \\ & \frac{1}{\lambda_2} & & & & \\ & & \frac{1}{\lambda_3} & & & \\ & & & \frac{1}{\lambda_4} & & \\ & & & & \frac{1}{\lambda_5} & \\ & & & & & \frac{1}{\lambda_6} \end{pmatrix}_{6\times 6}$$

with $\lambda_i = \max_{j\in[1,6]} |(\mathrm{D}_n^{(1)})_{ij}|$ being the absolute maximum in the i-th row. The matrices B_0 and b_0 are introduced to precondition the propagator matrix equations.

Let us define a coefficient vector that has ten elements as

$$\vec{\mathrm{x}}_n = (A_n, E_n^{(1)}, P_n^{(1)}, F_n^{(1)}, Q_n^{(1)}, G_n^{(1)}, R_n^{(1)}, E_n^{(\mathrm{M}+1)}, F_n^{(\mathrm{M}+1)}, G_n^{(\mathrm{M}+1)})^T$$

where the first entry is the coefficient of potential in the fluid, the next six entries are those in the first casing layer and the last three are those in the formation. Using Eq. (28) and Eq. (29), we can solve this vector by the following set of linear equations

$$\mathrm{L}_n \vec{\mathrm{x}}_n = \begin{bmatrix} \vec{0} \\ \vec{\mathrm{w}}_n^* \end{bmatrix} \tag{30}$$

where

$$\mathrm{L}_n = \begin{bmatrix} \vec{\mathrm{f}}_0 & -\widetilde{\mathrm{K}} \\ \widetilde{\mathrm{D}_1} & -\widetilde{\mathrm{D}_2} \end{bmatrix}_{10\times 10}$$

and where

$$\widetilde{\mathrm{G}}_n = \mathrm{B}_0\, \mathrm{G}_n\, \mathrm{B}_0^{-1}$$
$$\widetilde{\mathrm{D}_1} = \mathrm{B}_0\, \mathrm{D}_n^{(1)}(r_1)$$
$$\widetilde{\mathrm{D}_2} = \widetilde{\mathrm{G}}_n \mathrm{B}_0\, \mathrm{D}_n^{(\mathrm{M}+1)}(r_{\mathrm{M}+1})$$
$$\widetilde{\mathrm{K}} = \mathrm{b}_0\, \mathrm{S}\, \mathrm{B}_0^{-1}\, \widetilde{\mathrm{D}}_n^{(1)}$$
$$\vec{\mathrm{f}}_0 = \mathrm{b}_0\, \vec{\mathrm{f}}$$
$$\vec{\mathrm{w}}_n^* = \widetilde{\mathrm{G}}_n\, \mathrm{B}_0\, \vec{\mathrm{w}}_n(r_{\mathrm{M}+1}) \,,$$

The advantage of the global matrix method is that, after $\bar{c}_n^{(1)}$ and $\bar{c}_n^{(M+1)}$ are known, the $\bar{c}_n^{(i)}$ in the i-th annulus can be determined by either a backward matching from the outermost layer or a forward matching from the innermost layer. In terms of the matrix structure, as is shown in Chin et al. (1984), L_n has a block tridiagonal form and its inversion can be adequately computed by the Gaussian elimination method with partial pivoting (Schmidt and Tango, 1986). This method tends to yield great accuracy compared to the Thompson-Haskell propagator matrix algorithm.

Dispersion Equation

The dispersion equation in a cased borehole is given by

$$\det \mathrm{L}_n = 0 \tag{31}$$

i.e., the determinant of the 10×10 matrix L_n is zero.

Suppose $\mathrm{L}_n = \mathrm{L} \cdot \mathrm{U}$ is the LU decomposition of the matrix L_n by the Crout's algorithm (Press et al., 1989), and let γ_{ii} be the diagonal elements of the upper triangle matrix U , then Eq. (31) is equivalent to

$$F(k_z) = \Pi_{i=1}^{10} \gamma_{ii} = 0 .$$

We are concerned with possible excitation of surface and trapped modes due to complication of casing. A fluid resonance occurs whenever the vertical wavenumber of the incident wave is equal to the wavenumber of a particular mode whose pole is located on or near the real axis. Instead of solving the above nonlinear equation for its roots, we contour the amplitude of $F(k_z)$ on a logarithmic scale in the complex k_z plane for a frequency up to 2 kHz. The purpose of this analysis is to identify all singularities along the path of $k_z = \omega/\alpha \cos\delta$, for example, as δ varies from $0^o - 90^o$.

Figure 11 shows contour plots of $F(k_z)$ for the monopole mode $n = 0$ for the hard formation (Berea sandstone). The formation and casing properties as well as the borehole geometry are listed on the top of this figure. The horizontal axis is $Re(k_z)$, the real part of k_z. The vertical axis is $Im(k_z)$, the imaginary part of k_z. For a frequency at 100 Hz (top), singularities are associated with the tube wave pole k_T and the formation and casing branch cuts k_α, k_β, k_{α_c} and k_{β_c}. No other type of pole or branch cut can be identified. As the frequency increases to 2 kHz (bottom), evidently a pole (pseudo-Rayleigh mode) comes close to the real axis from the first quadrant. This pole is of less concern because it stays above the real axis for frequency below a cutoff value that is usually greater than 2 kHz.

Figure 12 shows contour plots of $F(k_z)$ for the dipole mode $n = 1$ for the hard formation (Berea sandstone). Different from those of the monopole mode, the tube

wave pole is replaced by the fluid branch cut k_f. There is no such fluid branch cut in the monopole mode as is shown by Kurkjian (1985). At a frequency equal to 2 kHz (bottom), a complex dipole pole appears in the first quadrant, which moves toward the formation shear branch cut at its cutoff frequency (greater than 2 kHz).

Figure 13 shows contour plots of $F(k_z)$ for the monopole mode $n = 0$ for the soft formation (Pierre shale). Different from that in the hard formation, in this case, the tube wave wavenumber k_T is in between the compressional branch cut k_α and the shear wavenumber branch cut k_β. As is shown by Peng et al. (1992), a significant fluid resonance occurs for an SV wave incidence at

$$\delta = \cos^{-1} \beta / C_T(\omega) \tag{32}$$

where the tube wave wavelength is equal to the vertical wavelength of the incident shear wave. In the soft formation with steel casing, the surface modes associated with the existence of the casing are evident at 2 kHz (bottom). They are dispersive and attenuative, and lie above the real axis.

Figure 14 shows contour plots of $F(k_z)$ for the dipole mode $n = 1$ for the soft formation (Pierre shale). In this case, the fluid branch cut is in between the compressional branch cut k_α and the shear wavenumber branch cut k_β. At a low frequency (100 Hz), no surface or trapped mode is evident in this plot. At a high frequency (2 kHz), the complex dipole pole appears in the first quadrant with a small phase velocity, which also moves toward the formation shear branch cut at its cutoff frequency that is greater than 2 kHz.

The above analyses show that, for a frequency up to 2 kHz, no mode other than the tube wave has potential impact on the fluid-solid motion in a cased borehole for both the hard and soft formations. The Stoneley wave dispersion in a cased borehole is extensively studied previously (Tubman, 1984; Tubman et al., 1984). Figure 15 shows the dispersion of a tube wave in an open and a cased borehole, computed by solving the above dispersion equation using a root finding algorithm (Press et al., 1989). This figure clearly shows that the tube wave in a cased borehole is less dispersive than in an open borehole. The casing significantly increases the tube wave phase velocity, implying the fluid resonance phenomenon associated with an SV incidence in a soft formation is more easily observable in a cased borehole than in an open borehole.

CASED BOREHOLE EFFECT ON DOWNHOLE HYDROPHONE MEASUREMENTS

At a low frequency, the pressure in a cased borehole due to a source in the formation is studied in the previous sections, where explicit and close form expressions have

been given. However, at high frequencies, no such expressions can be easily obtained. Numerical investigation by the global matrix method is needed to study how and by how much the cased borehole can influence a downhole hydrophone measurement. In this and the following sections, calculations are made with the benchmark formations Berea sandstone (fast, $\alpha = 4206\ m/s$, $\beta = 2664\ m/s$ and $\rho = 2140\ kg/m^3$) and Pierre shale (slow, $\alpha = 2074\ m/s$, $\beta = 869\ m/s$ and $\rho = 2000\ kg/m^3$). The casing is steel ($\alpha = 6100\ m/s$, $\beta = 3350\ m/s$ and $\rho = 7500\ kg/m^3$) with thickness 2.03 cm. The inner radius of the borehole is assumed to be 10.16 cm.

Plane P Wave Incidence

Figure 16 shows the pressure at the center of the fluid as a function of angle of incidence at frequencies 100 Hz, 500 Hz, 1000 Hz and 2000 Hz. The incident wave is a plane P wave. The casing is steel, and the formation is Berea sandstone. The physical parameters are listed on the top of the figure. The pressure is scaled by the P_0, the pressure of the incident P wave when the borehole is absent (Lovell and Hornby, 1990). Evidently, the pressure in the fluid has a main lobe at the normal incidence $\delta = 90^o$. At a low frequency ($< 500\ Hz$), there is a particular angle of incidence where the pressure in the cased borehole is nearly zero. This angle can be well predicted by equation Eq. (19). The frequency dependence is very small, although the pressure increases with the increase of frequency.

For the soft formation (Pierre shale), as is shown in Figure 17, the pressure in the fluid shows strong dependence on both frequency and incidence angle. At a low frequency, it has two lobes at normal incidence and grazing incidence. A minimum occurs at 35^o, which is in fair agreement with the angle predicted by equation Eq. (19). This minimum disappears as the frequency increases. It is interesting to note that, near the normal incidence, the pressure shows a similar behavior as that for the hard formation, while away from the normal incidence, it is strongly dependent on both frequency and angle of incidence.

Plane S Wave Incidence

Figure 18 shows the pressure at the center of the fluid as a function of angle of incidence at frequencies 100 Hz, 500 Hz, 1000 Hz and 2000 Hz for a plane SV wave incidence. The casing is steel and the formation is Berea sandstone. In this case, the pressure in the fluid shows a main lobe at $\delta \sim 40^o$ incidence and is almost independent of frequency.

When it comes to the soft formation with a plane SV wave incidence, a significant

fluid resonance occurs at $\delta = \cos^{-1} \beta/C_T(\omega) \sim 52.4^o$, as is shown in Figure 19. Different from the case with an open borehole (Peng et al., 1992), in the steel cased borehole the resonance is at a large angle of incidence and is prominent at very high frequency. This is because the tube wave velocity is raised well above the formation shear velocity. The kink at $\delta = 65^o$ and at 2 kHz is associated with the critical reflection of the P wave at the formation-casing interface.

Summary

Two phenomena are of interest for the pressure in a cased borehole: one is the vanishing of pressure at a particular angle of incidence for an incident plane P wave; the other is the fluid resonance in a soft formation for an incident plane SV wave. The former occurs at a low frequency when the casing thickness exceeds the critical thickness. The latter is prominent at all frequencies and is associated with excitation of the tube wave in the fluid. The critical angles for both of them can be well estimated by the simple and explicit relationships in Eq. (19) and Eq. (32).

CASED BOREHOLE EFFECT ON DOWNHOLE GEOPHONE MEASUREMENTS

This section is devoted to the study of the cased borehole effect on the downhole geophone measurements. Three aspects are of interest: the borehole reception pattern which signifies the influence of a fluid-filled borehole on the solid displacement as a function of angle of incidence; the borehole effect on particle motion which is important for horizontal component rotation from data itself; and the effect of geophone orientation since, generally, the exact location of the geophone at the borehole wall is unknown.

Borehole Reception Pattern

The *borehole reception pattern* is defined as the dependence of pressure in the fluid and solid displacement in the formation on the angle of incidence. Calculations in the following examples are made with a geophone at the forward direction ($r = r_b, \theta = 0^o$).

Plane P Wave Incidence

Figure 20 shows the borehole reception pattern for the radial component of solid displacement at the borehole wall. The incident wave is a plane P wave. The formation

is Berea sandstone (hard). As expected, the radial component is zero at the grazing incidence and is maximum at the normal incidence. It increases with the increase of frequency, especially at the normal incidence.

Figure 21 shows the borehole reception pattern for the vertical component of solid displacement at the borehole wall. In this case, the vertical component is zero at the normal incidence and possesses a lobe at the grazing incidence. Unexpectedly, it decreases with the increase of frequency, especially at the grazing incidence.

Figure 22 shows the borehole reception pattern for the radial component of solid displacement at the borehole wall for the soft formation (Pierre shale). Different from that in Figure 20, the radial component increases with the increase of frequency up to 1 kHz. Beyond 1 kHz, it evidently decreases, especially at the normal incidence.

Figure 23 shows the borehole reception pattern for the vertical component of solid displacement at the borehole wall. The formation is also Pierre shale (soft). Evidently, the low frequency behavior is the same as that in Figure 21. However, at a high frequency, the vertical component becomes significantly smaller than the incident wave, decreasing with the increase of frequency. The transition zone is between the angles of critical P→S refraction and P→P refraction in the casing-formation interface.

Plane S Wave Incidence

Shown in Figure 24 is the borehole reception pattern for the radial component of solid displacement at the borehole wall for the hard formation. The incident wave is a plane shear wave of SV type. As expected, at a low frequency, the reception pattern has a lobe at the grazing incidence. Increase of frequency will increase the radial component of solid displacement, especially at the grazing incidence.

Figure 25 shows the borehole reception pattern for the vertical component of solid displacement at the borehole wall for the hard formation and SV incidence. In this case, the lobe is at the normal incidence. The reception pattern shows little dependence on frequency.

For a soft formation and a plane SV wave incidence, the solid displacement on the borehole wall is also strongly affected by the excitation of the tube wave in the fluid. Away from the resonance angle, at low frequencies, the borehole reception patterns are similar to those for the hard formation. Figures 26 and 27 show the radial and vertical components of solid displacement at the borehole wall. The arrows mark the place where the fluid resonance occurs. Evidently, the impact of the tube wave is strong on the vertical component at low frequencies. However, at a high frequency, the influence

on the radial component becomes significant. At high frequencies and away from the fluid resonance regime, the radial and vertical components of solid displacement both decrease rapidly with the increase of frequency. The solid displacement on the borehole wall is significantly less than the incident wave.

Borehole Effect on Particle Motion

The borehole distorts not only the magnitude of solid displacement on the borehole wall but also its polarization, including the direction of particle motion and rectilinearity (Peng et al., 1992; Esmersoy, 1984). We are interested in the deviation of particle motion direction of the geophone measurement from that of the incident wave. The following examples show, in a polar coordinate, the solid displacement vector on the borehole wall for plane P wave and SV wave incidence. Calculations are made at $(r = r_b, \theta = 0^o)$.

Plane P Wave Incidence

Figure 28 shows the solid displacement on the borehole wall for a plane P wave incidence. The formation is Berea sandstone (hard); the casing is steel. Shown in these figures are the displacement vector as a function of angle of incidence for frequencies at 100 Hz, 500 Hz, 1000 Hz and 2000 Hz. The dashed lines radiating from the origin are the directions of the incident plane P wave. The angle of incidence is labeled along the circle. Since the P wave is polarized along the direction of propagation, the dashed lines also represent the polarization directions of the incident energy. The displacement vector on the borehole wall, which is the output of a downhole geophone, is represented by a solid arrow. Its length is the amplitude of the displacement vector, and its direction is the particle motion direction. The deviation of the arrow from the corresponding dashed line is the inclination deviation of 3-component measurements from that of the incident wave at the presence of a cased borehole. Evidently, the borehole effect on particle motion is minimal for a frequency below 1 kHz for the hard formation. At 2 kHz, noticeable inclination deviation can be found around 40^o incidence. Also, in this case, the amplitude of solid displacement is smaller than unity at grazing incidence, while at normal incidence the measurement is less affected by the cased borehole.

For the soft formation (Pierre shale), as is shown in Figure 29, the effect of the cased borehole on the downhole geophone measurement is more prominent except at a very low frequency ($\sim$ 100 Hz). For a frequency above 500 Hz, significant deviations of both the amplitude and particle motion direction are obvious. The inclination deviation can reach 25^o round $\delta = 45^o$ incidence at 2 kHz. The measurement is significantly smaller than the incident wave in amplitude especially at a grazing incidence and at

high frequencies. Since the geophone is at $\theta = 0^o$, i.e., the forward scattering direction where the borehole scattered energy is out of phase with the incident wave, especially at a high frequency, the behaviors shown in this figure are not unexpected at all.

Plane S Wave Incidence

Unlike a plane P wave, the S wave is polarized perpendicular to the incident ray direction. For the sake of graphic presentation, we rotate the direction by 90^o so that it is in line with the direction of incidence. Figure 30 shows the solid displacement on the borehole wall for a plane SV wave incidence at 100 Hz, 500 Hz, 1000 Hz and 2000 Hz. The formation is Berea sandstone (hard). In this case, the dashed lines are the ray direction of the incident plane SV wave; the arrows are the displacement vectors at the solid side of the borehole wall after a 90^o rotation. It is easy to show that the deviation of the arrow from the corresponding dashed line represents the inclination deviation of measurement particle motion direction from that of incident wave. As is shown in the figure, for the hard formation, the borehole effect on particle motion is small for a frequency below 1 kHz. At 2 kHz, large inclination deviation by as much as 12^o can be found around 40^o incidence. Different from the case of the P wave, at a high frequency, the amplitude tends to be larger than unity at grazing incidence and smaller than unity at normal incidence.

Figure 31 shows the solid displacement on the borehole wall for the soft formation (Pierre shale) for a plane SV wave incidence. In this case, the amplitude of solid displacement is significantly smaller than the incidence wave, even at a low frequency. This is because the geophone is in the shadow zone of the fluid-filled borehole. Calculations show that, if the geophone is at the backward scattering direction, i.e., $\theta = 180^o$, the amplitude of solid displacement is much larger than that with $\theta = 0^o$ as it is in this example. Nevertheless, the deviation of particle motion direction is prominent, reaching 70^o for a frequency above 1 kHz except at the normal and the grazing incidences.

Effect of Geophone Orientation

Borehole coupling is nonsymmetric in nature. Measurements are dependent on the position of a geophone around the borehole wall. This position is generally unknown. The following examples are used to study the variations of solid displacement as the geophone moves azimuthally around the borehole wall.

Plane P Wave Incidence

Figure 32 shows the solid displacement on the borehole wall as a function of the azimuthal orientation of the geophone for the hard formation. The incident wave is a plane P wave at a fixed angle of incidence $\delta = 45^o$. The frequency of the incident wave is chosen to be 1 kHz. Five plots are shown here: the middle one is a 3D presentation of the borehole deformation when a plane P wave impinges on the cased borehole; the one on the upper-left corner shows the magnitude of solid displacement as a function of geophone orientation; the upper-right one is the polarization characteristics – rectilinearity – as a function of the geophone orientation; the lower-left and lower-right ones show the azimuthal and inclination deviations between the solid displacement and the incident wave, respectively. Evidently, for the hard formation at 1 kHz, the geophone measurement is almost identical to that of the incident wave. The azimuthal deviation is negligible. The inclination deviation is less than 2^o. The solid motion is dominantly linear.

When it comes to the soft formation, the story is quite different. Figure 33 shows the solid displacement on the borehole wall as a function of the geophone orientation for the soft formation. Again, the incident wave is a plane P wave at a fixed angle of incidence $\delta = 45^o$. In this case, obviously, the solid displacement vector deflects horizontally. The deviation in inclination reaches 26^o to 30^o depending on the exact location of the geophone. The polarization in the forward scattering direction becomes elliptic with rectilinearity being 0.65 at $\theta = 0^o$, while in the backward scattering direction, the particle motion is linear. It is interesting to note that the azimuthal deviation is negligibly small.

Plane S Wave Incidence

Figure 34 shows the solid displacement on the borehole wall as a function of the azimuthal orientation of the geophone for the hard formation at 1 kHz. The incident wave is a plane SV wave at a fixed angle of incidence $\delta = 45^o$. In this case, the solid motion is linear and perpendicular to the direction of incidence. The maximum inclination deviation is about 4^o in the forward scattering direction. The borehole corruption to the geophone measurement is minimal.

Figure 35 shows the solid displacement on the borehole wall for a plane SV incidence at 1 kHz. The formation is Pierre shale (soft). As in the case of P incidence, the solid motion is dominantly horizontal, and the inclination deviation reaches more than 32^o. Unlike the previous examples, in this case the azimuthal deviation is also significant and is about 21^o at $\theta = 90^o$ where the solid motion is no longer linear (see the drop

in rectilinearity in the upper-right plot). The amplitude of solid displacement is much smaller in the forward scattering direction than in the backward scattering direction.

Summary

The examples in this section show that: (1) the cased borehole effect on downhole geophone measurements is minimal for frequency below 1 kHz for the hard formation and 500 Hz for the soft formation; (2) the fluid resonance in the borehole for the soft formation and the SV incidence also affects the solid displacement on the borehole wall; (3) for the soft formation and at high frequencies, significant deviations of particle motion direction exist for both the P wave and S wave incidences, the solid motion deflects to the horizontal plane; (4) generally, the steel casing reduces the solid displacement on the borehole wall, especially at a high frequency and in the soft formation.

A LABORATORY EXPERIMENT

To verify the phenomenon of fluid resonance in a cased borehole due to a plane SV incidence, we carry out a laboratory experiment to measure the pressure in the fluid due to a shear source in the formation. Figure 36 shows the laboratory setup. The model is a glass tube buried in a dry soil. The inner diameter of the glass tube is 0.95 cm, the outer radius is 1.20 cm. The overall size of the model is 19.0 cm (diameter) $\times$ 34.0 cm (height). The model is cut to form two steps in the upper-right corner. A shear transducer (v152) is used as a source, which vibrates in the vertical direction. Its operating frequency is between 50–100 kHz. The two steps are at 3.1 cm and 4.9 cm offsets from the center of the borehole. We measured the compressional and shear velocities in the soil. They are $1800 \pm 10\ m/s$ and $1140 \pm 40\, m/s$ respectively. The shear velocity is less accurate because of the size of the model and the interference of the P wave. The Stoneley wave velocity is measured from the recorded logging seismograms as is shown in Figure 37. This data is obtained with the source and the receiver inside the borehole. The estimated Stoneley velocity is $1190 \pm 20\, m/s$. We also measured the attenuation of S waves in the soil by the method described by Toksöz and Johnston (1979), and the result is 15.7 m^{-1} at 100 kHz. Theoretically, using these parameters, we predicted that the measured pressure in the fluid due to an S wave incidence has a peak at

$$\delta = \cos^{-1} \beta / C_T \approx 16^o \pm 5^o \ .$$

The goal of this experiment is to compare the theoretical prediction with experimental results.

Shown in Figures 38 and 39 are the measured pressures in the fluid for a shear source at horizontal offset 4.9 *cm* and 3.1 *cm*, respectively. The center frequency is 50 kHz in the first measurement and 100 kHz in the second one. The traces are sampled at 5 *mm* intervals. A total of 40 traces are shown in each plot. The P and S arrivals are identified using their travel times and are marked on the seismograms. When the source frequency is high (Figure 39), the casing P and S waves are excited and they are clearly shown in the seismograms. However, at a low frequency (Figure 38), these waves are hardly seen.

We are interested in the region where δ, the incident angle with respect to the borehole axis, is small ($< 35^o$). We measure the amplitude of the shear wave directly from the individual seismogram. The results are plotted in Figure 40 (solid circle, also referred to as *raw data* in this figure) as a function of angle of incidence.

Since traces with smaller incidence angle travel longer distances, a geometrical correction (multiplying the source-receiver distance R) must be applied. Also attenuation compensation for energy traveling in the soil must be applied by multiplying the raw data by $e^{\gamma R}$ where γ is the attenuation coefficient. The most difficult correction is the source radiation pattern. The shear transducer will radiate most shear energy in the direction where δ is large. Tang et al. (1992) studied the radiation of a shear transducer at the surface of an elastic half space. Their results show that, at least, a $\sin\delta$ correction should be applied to compensate loss of amplitude due to shear source radiation.

The attenuation, geometrical spreading and radiation correction by $\sin\delta$ are made to the raw data with a reference at the trace having the shortest source-receiver distance. The shear wave amplitude after these corrections is shown in Figure 40 with an open circle. To the extreme, we also show the open triangles, which are the shear wave amplitude after an additional $\sin\delta$ correction, since we believe a sine correction alone may not be adequate at a regime where δ is small. Nevertheless, in the experiment with $4.9cm$ offset, a peak at 18^o is evident; and in the experiment with $3.1cm$ offset, the peak is at 12^o. Within the accuracy of this experiment, these results are in fair agreement with the theoretical prediction.

DISCUSSIONS AND CONCLUSIONS

In this paper, approximate and exact formulations have been presented for borehole coupling in a cased borehole. The approximate solutions are simple, explicit, and accurate at a low frequency. They tend to yield more physical insights into the coupling of energy into the borehole fluid. The approximate solutions can be as well applied to the study of cased borehole radiation by using the reciprocity principle. This statement

is justified by a comparison with the generalized stationary phase approximation for a volume source in the cased borehole (Gibson, 1993). Winbow (1991) gave an explicit low frequency formulation for the cased borehole radiation problem, and it turns out his formulation is erroneous except at the direction normal to the borehole axis.

On the other hand, the exact solution is valid for all frequency and azimuthally symmetric and nonsymmetric components. It can handle many radial layers such as casing and cements. It is useful to study numerically the dependence of downhole seismic measurements on frequency, angle of incidence, polarization of incident wave, and geophone orientation.

In summary, we found

- For the hard formation and plane P wave incidence, the cased borehole effect on downhole geophone measurements is minimal for a frequency below 1 kHz. Above 1 kHz, the radial component becomes larger in magnitude than that of the incident wave and the vertical component becomes smaller. The deviation of particle motion direction can reach several degrees at 2 kHz.
- For the hard formation and plane SV wave incidence, the downhole geophone measurements are almost not affected by the presence of a fluid-filled borehole for a frequency below 1 kHz. Above 1 kHz, the radial component increases with the increase of frequency and the vertical component is less dependent on frequency. The particle motion direction may differ from that of the incident wave by as much as 12^o at 2 kHz.
- For the soft formation and plane P wave incidence, the cased borehole effect on downhole geophone measurements is significant for a frequency above hundreds of hertz ($< 500\ Hz$). The radial and vertical components are much smaller than those of the incident wave at high frequencies. The inclination deviation can reach 25^o at around 45^o incidence at 2 kHz. The solid displacement vector deflects horizontally. The measurements show strong dependence on the geophone orientation. The polarization becomes elliptic in the forward scattering direction and remains linear in the backward scattering direction.
- For the soft formation and plane SV wave incidence, the fluid resonance inside the borehole at $\delta = \cos^{-1}\beta/C_T$ exerts strong influence on the solid displacement at the borehole wall, even at very low frequencies. Away from the resonance angle, the radial and vertical components of solid displacement decrease rapidly with the increase of frequency. The deviation of particle motion direction from that of the incident wave is large. It reaches 70^o at 2 kHz. The solid motion becomes dominantly horizontal at high frequency. The azimuthal deviation is also significant, reaching 21^o at $\theta = 90^o$ at 1 kHz.

- The pressure in the fluid shows two interesting behaviors, depending on the type of the incident wave. For a plane SV incidence in the soft formation, a significant fluid resonance occurs in the borehole where the pressure can be significantly large. This phenomenon is prominent at all frequencies. For a plane P wave incidence at a low frequency, the pressure in the fluid vanishes at a particular angle of incidence if the casing thickness exceeds a critical value. This behavior prevails in both the hard and soft formations.
- The fluid resonance due to an SV incidence in the soft formation is verified by the laboratory experiment with the glass-soil borehole model.

ACKNOWLEDGMENTS

This work is supported by the ERL/nCUBE Geophysical Center for Parallel Processing and the Borehole Acoustics and Logging Consortium at the Earth Resources Laboratory, M.I.T. Chengbin Peng holds an nCUBE graduate student fellowship.

REFERENCES

Albright, J.N., and P.AJohnson, 1990, Cross-borehole observation of mode conversion from borehole Stoneley waves to channel waves at a coal layer, *Geophysical Prospecting, 38*, 607–620.

Blair, D.P., 1984, Rise times of attenuated seismic pulse detected in both empty and fluid-filled cylindrical boreholes, *Geophysics, 49,* 398–410.

Chin, R.C.Y., G.W. Hedstrom, and L. Thigpen, 1984, Matrix methods in synthetic seismograms, *Geophys. J. R. Astr. Soc., 77,* 483–502.

Dunkin, J.W., 1965, Computation of modal solutions in layered, elastic media at high frequencies, *Bull. Seism. Soc. Am., 55,* 335–358.

Esmersoy, C., 1984., Polarization analysis, rotation and velocity estimation in three component VSP, *Vertical Seismic Profiling*, M.N., Toksöz and R.R., Stewart (ed.), 14B, 236–255. Geophysical Press.

Gibson, R.L., 1993, Radiation from seismic sources in cased and cemented boreholes, *submitted to Geophysics.*

Kurkjian, A.L., 1985, Numerical computation of individual far-field arrivals excited by an acoustic source in a borehole, *Geophysics, 50,* 852–866.

Lee, M.W., 1987, Particle displacement on the wall of a borehole from incident plane wave, *Geophysics, 52,* 1290–1296.

Love, A.E.H., 1927, *A Treatise on the Mathematical Theory of Elasticity*, 4th Revised Edition, Cambridge University Press, Cambrdige, UK.

Lovell, J.R., and B.E. Hornby, 1990, Borehole coupling at sonic frequencies, *Geophysics, 55,* 806–814.

Marzetta, T.L., and M., Schoenberg, 1985, Tube waves in cased boreholes, *SEG Extended Abstract, Washington D.C.,* 34–36.

Marzetta, T.L., 1992, Inverse borehole coupling theory and its application to hydrophone vertical seismic profiling, *SEG Extended Abstract, New Orleans,* 145–147.

Norris, A., 1990, The speed of a tube wave, *J. Acoust. Soc. Am., 87,* 414–417.

Peng, C., C.H. Cheng, and M.N. Toksöz, 1992, Borehole effect on downhole seismic measurements: *Geophys. Prosp.,* in press.

Pratt, R.G., G.F. West, P.A. Hurley, and Z. Zeng, 1992, Crosshole seismology in the Athabasca tar sands, *SEG Extended Abstract, New Orleans,* 63–66.

Press, W.H., B.P. Flannery, S.A. Teukolsky, and W.T. Vetterling, 1989. *Numerical Recipes: the Art of Scientific Computing, Cambridge University Press*, 301–307.

Schmidt, H., and G. Tango, 1986, Efficient global matrix approach to the computation of synthetic seismograms, *Geophys. J. R. Astr. Soc., 84,* 331–359.

Schoenberg, M., T.L. Marzetta,, J. Aron, and R. Porter, 1981, Space-time dependence of acoustic waves in a borehole, *J. Acoust. Soc. Am., 70,* 1496–1507.

Schoenberg, M, 1986, Fluid and solid motion on the neighborhood of a fluid-filled borehole due to the passage of a low frequency elastic plane wave, *Geophysics, 51,* 1191–1205.

Tang, X.M., Z. Zhu, and M.N. Toksöz, 1992, Radiation patterns of compressional and shear transducers at the surface of an elastic half space, Borehole Acoustics and Logging Consortium Annual Report, M.I.T., 249–272.

Toksöz, M.N., and D.H. Johnston, 1979, *Seismic Wave Attenuation, Geophysics Reprint Series,* SEG.

Tubman, K, 1984, Full waveform acoustic logs in radially layered boreholes, Ph.D. thesis, M.I.T., Cambridge, Massachusetts

Tubman, K., C.H. Cheng, and M.N. Toksöz, 1984, Synthetic full-waveform acoustic logs in cased boreholes, *Geophysics, 49,* 1051–1059.

White, J.E., 1953, Signals in a borehole due to plane waves in the solid, *J. Acoust. Soc. Amer., 25,* 906–915.

White, J.E., 1983, *Underground Sound: Application of Seismic Waves,* Elsevier.

Winbow, G.A., 1991, Seismic sources in open and cased boreholes, *Geophysics, 56,* 1040–1050.

APPENDIX A

$$\mathrm{D} = \begin{bmatrix} \mathcal{U}_{rn}^{\phi(1)}(r) & \mathcal{U}_{rn}^{\phi(2)}(r) & \mathcal{U}_{rn}^{\xi(1)}(r) & \mathcal{U}_{rn}^{\xi(2)}(r) & \mathcal{U}_{rn}^{\psi(1)}(r) & \mathcal{U}_{rn}^{\psi(2)}(r) \\ \mathcal{U}_{\theta n}^{\phi(1)}(r) & \mathcal{U}_{\theta n}^{\phi(2)}(r) & \mathcal{U}_{\theta n}^{\xi(1)}(r) & \mathcal{U}_{\theta n}^{\xi(2)}(r) & \mathcal{U}_{\theta n}^{\psi(1)}(r) & \mathcal{U}_{\theta n}^{\psi(2)}(r) \\ \mathcal{U}_{zn}^{\phi(1)}(r) & \mathcal{U}_{zn}^{\phi(2)}(r) & \mathcal{U}_{zn}^{\xi(1)}(r) & \mathcal{U}_{zn}^{\xi(2)}(r) & \mathcal{U}_{zn}^{\psi(1)}(r) & \mathcal{U}_{zn}^{\psi(2)}(r) \\ \mathcal{R}_{\phi n}^{(1)}(r) & \mathcal{R}_{\phi n}^{(2)}(r) & \mathcal{R}_{\xi n}^{(1)}(r) & \mathcal{R}_{\xi n}^{(2)}(r) & \mathcal{R}_{\psi n}^{(1)}(r) & \mathcal{R}_{\psi n}^{(2)}(r) \\ \mathcal{T}_{\phi n}^{(1)}(r) & \mathcal{T}_{\phi n}^{(2)}(r) & \mathcal{T}_{\xi n}^{(1)}(r) & \mathcal{T}_{\xi n}^{(2)}(r) & \mathcal{T}_{\psi n}^{(1)}(r) & \mathcal{T}_{\psi n}^{(2)}(r) \\ \mathcal{Z}_{\phi n}^{(1)}(r) & \mathcal{Z}_{\phi n}^{(2)}(r) & \mathcal{Z}_{\xi n}^{(1)}(r) & \mathcal{Z}_{\xi n}^{(2)}(r) & \mathcal{Z}_{\psi n}^{(1)}(r) & \mathcal{Z}_{\psi n}^{(2)}(r) \end{bmatrix}$$

where

$$\mathcal{U}_{rn}^{\phi(1)}(r) = \alpha k_p H_n^{(1)'}(k_p r), \qquad \mathcal{U}_{rn}^{\phi(2)}(r) = \alpha k_p H_n^{(2)'}(k_p r)$$
$$\mathcal{U}_{rn}^{\xi(1)}(r) = -\beta \frac{k_z k_s}{k_\beta} H_n^{(1)'}(k_s r), \qquad \mathcal{U}_{rn}^{\xi(2)}(r) = -\beta \frac{k_z k_s}{k_\beta} H_n^{(2)'}(k_s r)$$
$$\mathcal{U}_{rn}^{\psi(1)}(r) = \beta \frac{k_s}{k_s r} n H_n^{(1)}(k_s r), \qquad \mathcal{U}_{rn}^{\psi(2)}(r) = \beta \frac{k_s}{k_s r} n H_n^{(2)}(k_s r)$$

$$\mathcal{U}_{\theta n}^{\phi(1)}(r) = \alpha \frac{k_p}{k_p r} n H_n^{(1)}(k_p r), \qquad \mathcal{U}_{\theta n}^{\phi(2)}(r) = \alpha \frac{k_p}{k_p r} n H_n^{(2)}(k_p r)$$
$$\mathcal{U}_{\theta n}^{\xi(1)}(r) = -\beta \frac{k_z}{k_\beta r} n H_n^{(1)}(k_s r), \qquad \mathcal{U}_{\theta n}^{\xi(2)}(r) = -\beta \frac{k_z}{k_\beta r} n H_n^{(2)}(k_s r)$$
$$\mathcal{U}_{\theta n}^{\psi(1)}(r) = \beta k_s H_n^{(1)'}(k_s r), \qquad \mathcal{U}_{\theta n}^{\psi(2)}(r) = \beta k_s H_n^{(2)'}(k_s r)$$

$$\mathcal{U}_{zn}^{\phi(1)}(r) = \alpha i k_z H_n^{(1)}(k_p r), \qquad \mathcal{U}_{zn}^{\phi(2)}(r) = \alpha i k_z H_n^{(2)}(k_p r)$$
$$\mathcal{U}_{zn}^{\xi(1)}(r) = -\beta i \frac{{k_s}^2}{k_\beta} H_n^{(1)}(k_s r), \qquad \mathcal{U}_{zn}^{\xi(2)}(r) = -\beta i \frac{{k_s}^2}{k_\beta} H_n^{(2)}(k_s r)$$
$$\mathcal{U}_{zn}^{\psi(1)}(r) = 0, \qquad \mathcal{U}_{zn}^{\psi(2)}(r) = 0$$

$$\mathcal{R}_{\phi n}^{(1)}(r) = -\rho\alpha[(\omega^2 - 2\beta^2 {k_z}^2) H_n^{(1)}(k_p r) + \frac{2\beta^2 {k_p}^2}{k_p r}(H_n^{(1)'}(k_p r) - \frac{n^2}{k_p r} H_n^{(1)}(k_p r))]$$
$$\mathcal{R}_{\phi n}^{(2)}(r) = -\rho\alpha[(\omega^2 - 2\beta^2 {k_z}^2) H_n^{(2)}(k_p r) + \frac{2\beta^2 {k_p}^2}{k_p r}(H_n^{(2)'}(k_p r) - \frac{n^2}{k_p r} H_n^{(2)}(k_p r))]$$
$$\mathcal{R}_{\xi n}^{(1)}(r) = \rho\beta \frac{2 k_z {k_s}^2 \beta^2}{k_\beta}[H_n^{(1)}(k_s r) + \frac{1}{k_s r} H_n^{(1)'}(k_s r) - \frac{n^2}{{k_s}^2 r^2} H_n^{(1)}(k_s r)]$$
$$\mathcal{R}_{\xi n}^{(2)}(r) = \rho\beta \frac{2 k_z {k_s}^2 \beta^2}{k_\beta}[H_n^{(2)}(k_s r) + \frac{1}{k_s r} H_n^{(2)'}(k_s r) - \frac{n^2}{{k_s}^2 r^2} H_n^{(2)}(k_s r)]$$
$$\mathcal{R}_{\psi n}^{(1)}(r) = -\rho\beta 2\beta^2 {k_s}^2 n[\frac{1}{{k_s}^2 r^2} H_n^{(1)}(k_s r) - \frac{1}{k_s r} H_n^{(1)'}(k_s r)]$$
$$\mathcal{R}_{\psi n}^{(2)}(r) = -\rho\beta 2\beta^2 {k_s}^2 n[\frac{1}{{k_s}^2 r^2} H_n^{(2)}(k_s r) - \frac{1}{k_s r} H_n^{(2)'}(k_s r)]$$

$$\mathcal{T}_{\phi n}^{(1)}(r) = -\rho\alpha 2\beta^2 {k_p}^2 n[\tfrac{1}{{k_p}^2 r^2} H_n^{(1)}(k_p r) - \tfrac{1}{k_p r} H_n^{(1)'}(k_p r)]$$
$$\mathcal{T}_{\phi n}^{(2)}(r) = -\rho\alpha 2\beta^2 {k_p}^2 n[\tfrac{1}{{k_p}^2 r^2} H_n^{(2)}(k_p r) - \tfrac{1}{k_p r} H_n^{(2)'}(k_p r)]$$
$$\mathcal{T}_{\xi n}^{(1)}(r) = \rho\beta \tfrac{2k_z {k_s}^2 \beta^2}{k_\beta} n[\tfrac{1}{{k_s}^2 r^2} H_n^{(1)}(k_s r) - \tfrac{1}{k_s r} H_n^{(1)'}(k_s r)]$$
$$\mathcal{T}_{\xi n}^{(2)}(r) = \rho\beta \tfrac{2k_z {k_s}^2 \beta^2}{k_\beta} n[\tfrac{1}{{k_s}^2 r^2} H_n^{(2)}(k_s r) - \tfrac{1}{k_s r} H_n^{(2)'}(k_s r)]$$
$$\mathcal{T}_{\psi n}^{(1)}(r) = -\rho\beta\beta^2 {k_s}^2 [H_n^{(1)}(k_s r) + \tfrac{2}{k_s r} H_n^{(1)'}(k_s r) - \tfrac{2n^2}{{k_s}^2 r^2} H_n^{(1)}(k_s r)]$$
$$\mathcal{T}_{\psi n}^{(2)}(r) = -\rho\beta\beta^2 {k_s}^2 [H_n^{(2)}(k_s r) + \tfrac{2}{k_s r} H_n^{(2)'}(k_s r) - \tfrac{2n^2}{{k_s}^2 r^2} H_n^{(2)}(k_s r)]$$

$$\mathcal{Z}_{\phi n}^{(1)}(r) = \rho\alpha 2ik_z k_p \beta^2 H_n^{(1)'}(k_p r)$$
$$\mathcal{Z}_{\phi n}^{(2)}(r) = \rho\alpha 2ik_z k_p \beta^2 H_n^{(2)'}(k_p r)$$
$$\mathcal{Z}_{\xi n}^{(1)}(r) = -\rho\beta i \tfrac{({k_z}^2 - {k_s}^2) k_s \beta^2}{k_\beta} H_n^{(1)'}(k_s r)$$
$$\mathcal{Z}_{\xi n}^{(2)}(r) = -\rho\beta i \tfrac{({k_z}^2 - {k_s}^2) k_s \beta^2}{k_\beta} H_n^{(2)'}(k_s r)$$
$$\mathcal{Z}_{\psi n}^{(1)}(r) = \rho\beta i k_z k_s \beta^2 \tfrac{n}{k_s r} H_n^{(1)}(k_s r)$$
$$\mathcal{Z}_{\psi n}^{(2)}(r) = \rho\beta i k_z k_s \beta^2 \tfrac{n}{k_s r} H_n^{(2)}(k_s r)$$

where α, β and ρ are compressional velocity, shear velocity and density in the each layer respectively. $k_\alpha = \frac{\omega}{\alpha}$, $k_\beta = \frac{\omega}{\beta}$, $k_p = \sqrt{{k_\alpha}^2 - {k_z}^2}$, $k_s = \sqrt{{k_\beta}^2 - {k_z}^2}$ and $k_f = \sqrt{\frac{\omega^2}{\alpha_f^2} - {k_z}^2}$. k_z is the vertical wavenumber which should be preserved upon reflection or refraction according to the Snell's law, and $k_z = k_{\alpha N+1} \cos\delta$ for a plane P wave incidence and $k_z = k_{\beta_{N+1}} \cos\delta$ for a plane shear wave incidence. δ is the incidence angle with respect to the borehole axis (i.e., $\delta = 90^o$ corresponds to normal incidence on the borehole).

APPENDIX B

The displacement-stress vector $\vec{\mathrm{w}}(r)$ due to the incident waves can be easily computed from the displacement potentials given in Schoenberg (1986). The n-th harmonic component can be written as

$$\vec{\mathrm{w}}(r) = \left[\mathcal{U}^P_{rn}(r), \mathcal{U}^P_{\theta n}(r), \mathcal{U}^P_{zn}(r), \mathcal{R}_{Pn}(r), \mathcal{T}_{Pn}(r), \mathcal{Z}_{Pn}(r)\right]^T$$

for a plane P wave incidence, and

$$\vec{\mathrm{w}}(r) = \left[\mathcal{U}^{SV}_{rn}(r), \mathcal{U}^{SV}_{\theta n}(r), \mathcal{U}^{SV}_{zn}(r), \mathcal{R}_{SVn}(r), \mathcal{T}_{SVn}(r), \mathcal{Z}_{SVn}(r)\right]^T$$

for a plane SV wave incidence and

$$\vec{\mathrm{w}}(r) = \left[\mathcal{U}^{SH}_{rn}(r), \mathcal{U}^{SH}_{\theta n}(r), \mathcal{U}^{SH}_{zn}(r), \mathcal{R}_{SHn}(r), \mathcal{T}_{SHn}(r), \mathcal{Z}_{SHn}(r)\right]^T$$

for a plane SH wave incidence.

The coefficients are given below

$$\mathcal{U}^P_{rn}(r) = \alpha k_p J_n'(k_p r), \quad \mathcal{U}^P_{\theta n}(r) = \alpha \frac{k_p}{k_p r} n J_n(k_p r), \quad \mathcal{U}^P_{zn}(r) = \alpha i k_z J_n(k_p r)$$

$$\mathcal{U}^{SV}_{rn}(r) = -\beta k_z J_n'(k_s r), \quad \mathcal{U}^{SV}_{\theta n}(r) = -\beta \frac{k_z}{k_s r} n J_n(k_s r), \quad \mathcal{U}^{SV}_{zn}(r) = \beta i k_s J_n(k_s r)$$

$$\mathcal{U}^{SH}_{rn}(r) = \beta \frac{k_\beta}{k_s r} n J_n(k_s r), \quad \mathcal{U}^{SH}_{\theta n}(r) = -\beta k_\beta J_n'(k_s r), \quad \mathcal{U}^{SH}_{zn}(r) = 0$$

$$\mathcal{R}_{Pn}(r) = -\rho\alpha[(\omega^2 - 2\beta^2 k_z{}^2) J_n(k_p r) + 2\beta^2 \frac{k_p{}^2}{k_p r}(J_n'(k_p r) - \frac{n^2}{k_p r} J_n(k_p r))]$$

$$\mathcal{T}_{Pn}(r) = -\rho\alpha 2\beta^2 k_p{}^2 n[\frac{1}{k_p{}^2 r^2} J_n(k_p r) - \frac{1}{k_p r} J_n'(k_p r)]$$

$$\mathcal{Z}_{Pn}(r) = \rho\alpha 2i\beta^2 k_z k_p J_n'(k_p r)$$

$$\mathcal{R}_{SVn}(r) = 2\rho\beta^3 k_z k_s[J_n(k_s r) + \frac{1}{k_s r} J_n'(k_s r) - \frac{n^2}{k_s{}^2 r^2} J_n(k_s r)]$$

$$\mathcal{T}_{SVn}(r) = -2\rho\beta^3 k_s k_z n[\frac{1}{k_s r} J_n'(k_s r) - \frac{1}{k_s{}^2 r^2} J_n(k_s r)]$$

$$\mathcal{Z}_{SVn}(r) = i\rho\beta^3 (k_s{}^2 - k_z{}^2) J_n'(k_s r)$$

$$\mathcal{R}_{SHn}(r) = 2\rho\beta^3 k_s{}^2 n[\frac{1}{k_s r} J_n'(k_s r) - \frac{1}{k_s{}^2 r^2} J_n(k_s r)]$$

$$\mathcal{T}_{SHn}(r) = \rho\beta^3 k_s{}^2[J_n(k_s r) + \frac{2}{k_s r} J_n'(k_s r) - \frac{2n^2}{k_s{}^2 r^2} J_n(k_s r)]$$

$$\mathcal{Z}_{SHn}(r) = i\rho\beta^3 k_s k_z \frac{n}{k_s r} J_n(k_s r).$$

APPENDIX C

In this appendix, we outline the methods we used in deriving the effective moduli $E_\parallel$ and $E_\perp$ of a cased borehole. First consider an empty cased borehole subject to a stress state at infinity: $\sigma_{rr} = \sigma_{\theta\theta} = \sigma_0$ and $\sigma_{zz} = 2\nu\sigma_0$. The radial displacement on the borehole wall can be obtained by using the Airy function method (Love, 1927), yielding

$$u_r/r_b = \frac{2(1-\nu^2)}{E} \frac{\sigma_0}{1+(\frac{\mu_c}{\mu}-1)(1-\gamma_c)(1-\frac{r_b^2}{r_c^2})} .$$

Next consider a stress state at infinity: $\sigma_{rr} = \sigma_{\theta\theta} = 0$ and $\sigma_{zz} = \sigma_0$. In this case, the radial displacement on the borehole wall is found to be

$$u_r/r_b = -\frac{\nu\sigma_0}{E} \frac{1}{1+(\frac{\mu_c}{\mu}-1)(1-\gamma_c)(1-\frac{r_b^2}{r_c^2})} - \frac{\sigma_0}{2E} \frac{(\frac{\mu_c}{\mu}-1)(1-2\gamma_c)(1-\frac{r_b^2}{r_c^2})}{1+(\frac{\mu_c}{\mu}-1)(1-\gamma_c)(1-\frac{r_b^2}{r_c^2})} .$$

Comparison with Eq. (17) leads to the expressions for $E_\parallel$ and $E_\perp$ given in the text.

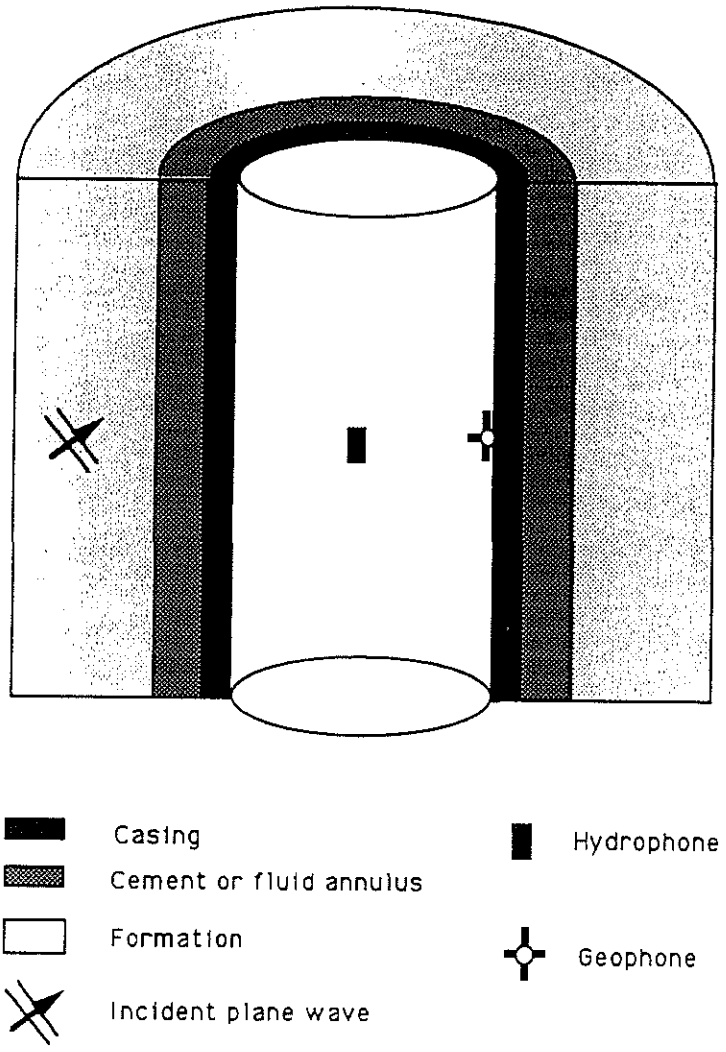

Figure 1: A fluid-filled borehole in a radially layered formation. An elastic wave impinges on the cased and cemented borehole with an angle of incidence δ (with respect to the borehole axis). A hydrophone measures pressure at the center of the borehole. A geophone measures the three component displacement at $(r = r_b, \theta)$, where r_b is the borehole radius. The direction with $-90^o \leq \theta < 90^o$ is referred to as the forward scattering direction and $90^o \leq \theta < 270^o$ the backward scattering direction.

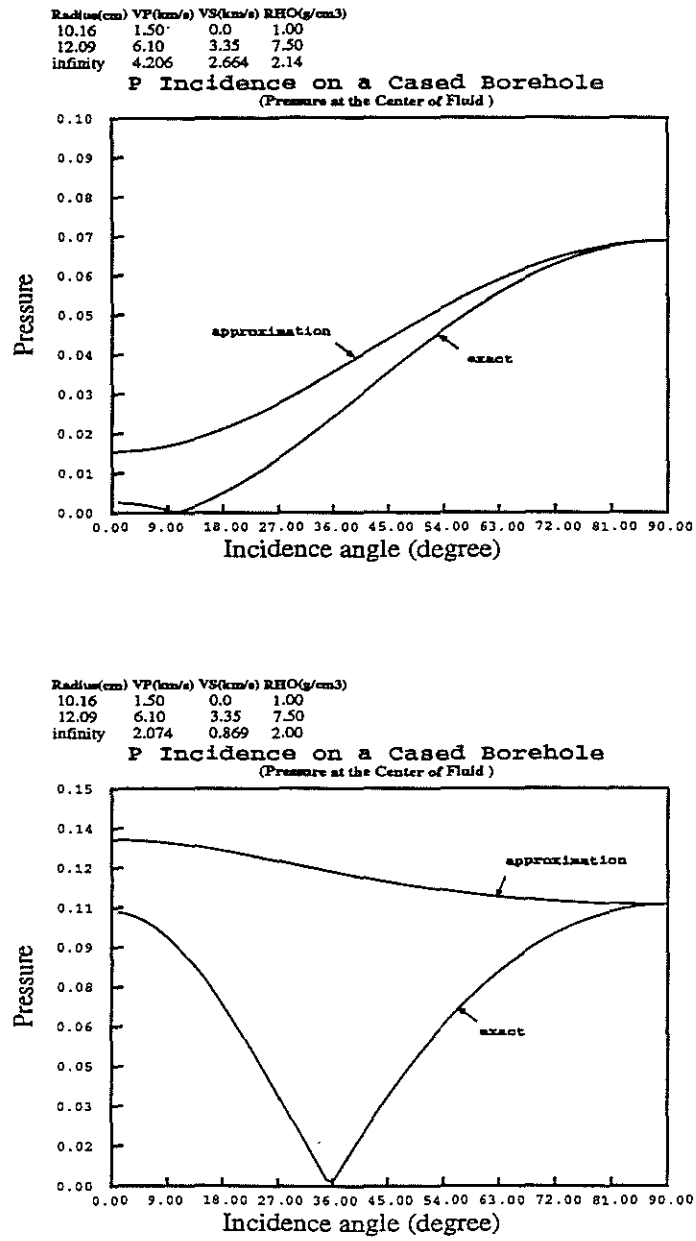

Figure 2: Pressure at the borehole fluid for an incident plane P wave at a low frequency. The *approximation* is obtained by the leading order analysis. The *exact* is from numerical calculation by the global matrix method. The top one is for the hard formation; the bottom one is for the soft formation. By comparison, one can see that the leading order approximation is accurate only around normal incidence of the plane P wave.

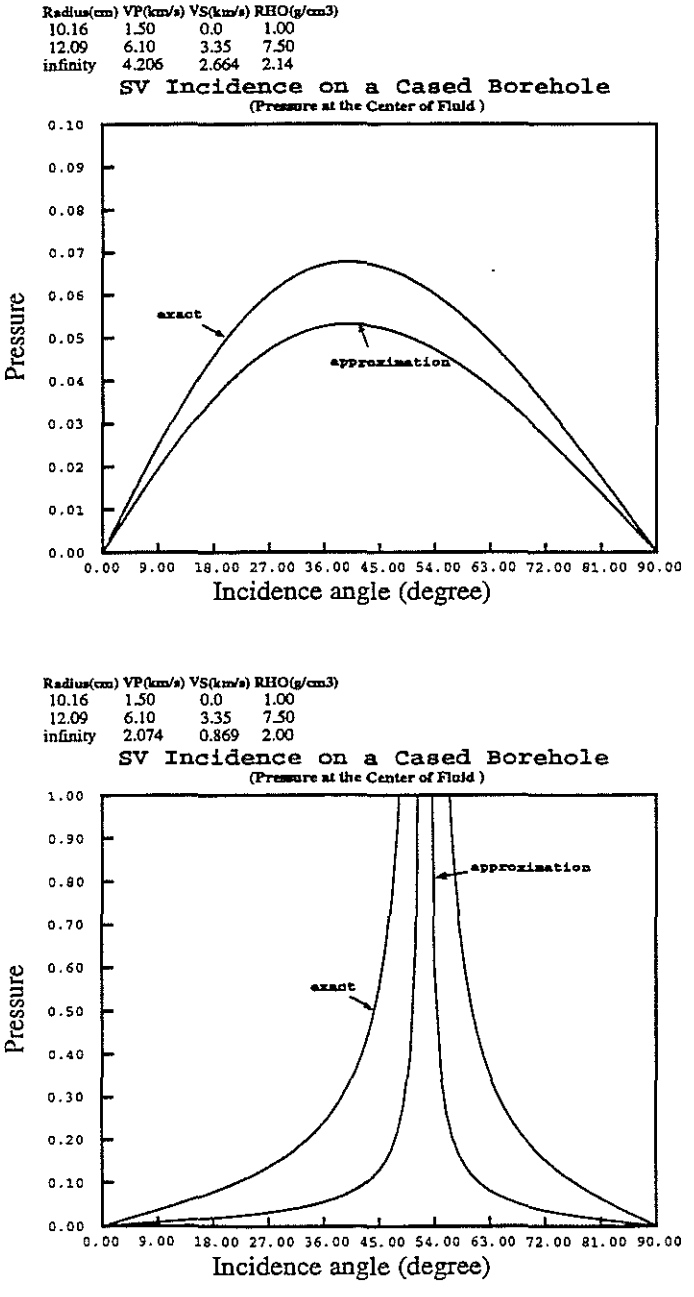

Figure 3: Same as those in Figure 2 except, in this case, the incident wave is a plane SV wave. The fluid resonance in the soft formation is evident.

Radius(cm)	VP(km/s)	VS(km/s)	RHO(g/cm3)
10.16	1.50	0.0	1.00
?????	6.10	3.35	7.50
infinity	4.206	2.664	2.14

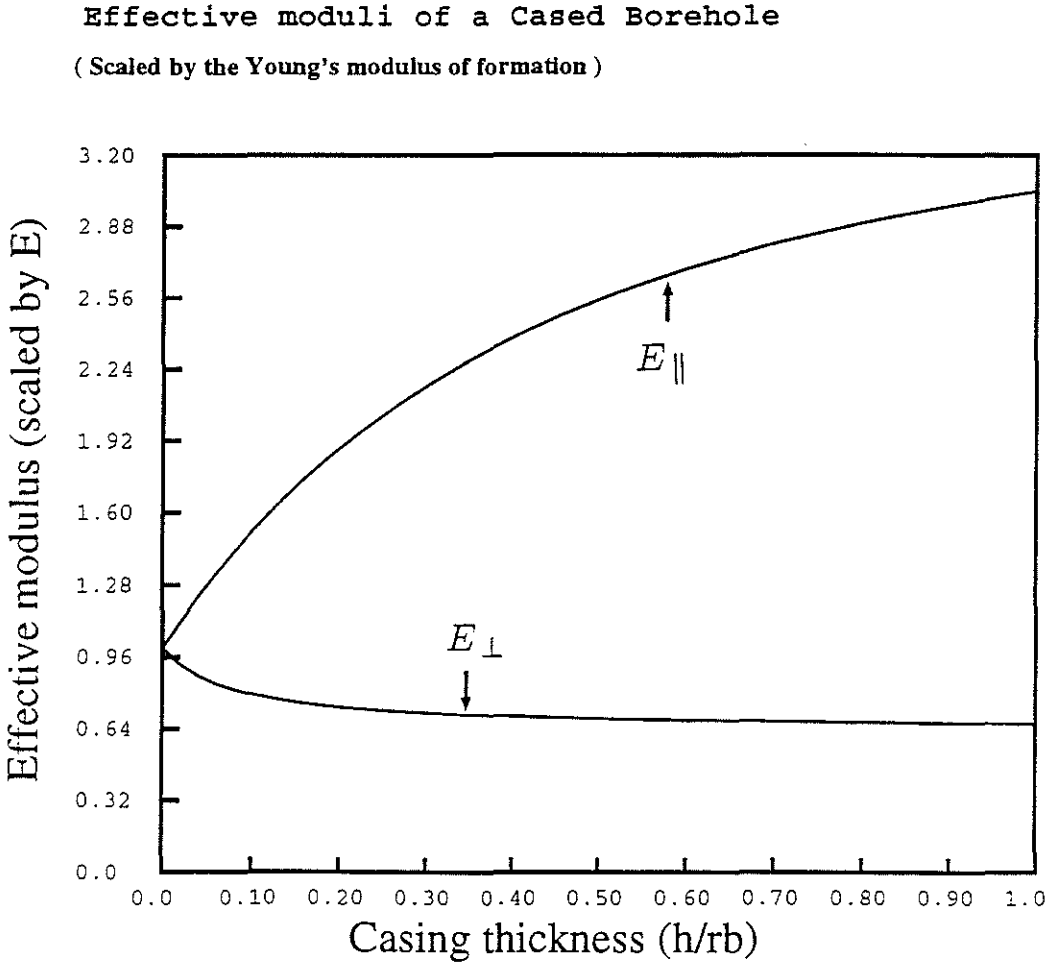

Figure 4: Effective moduli of a cased borehole as a function of casing thickness. The formation is Berea sandstone (hard).

Radius(cm)	VP(km/s)	VS(km/s)	RHO(g/cm3)
10.16	1.50	0.0	1.00
?????	6.10	3.35	7.50
infinity	2.074	0.869	2.00

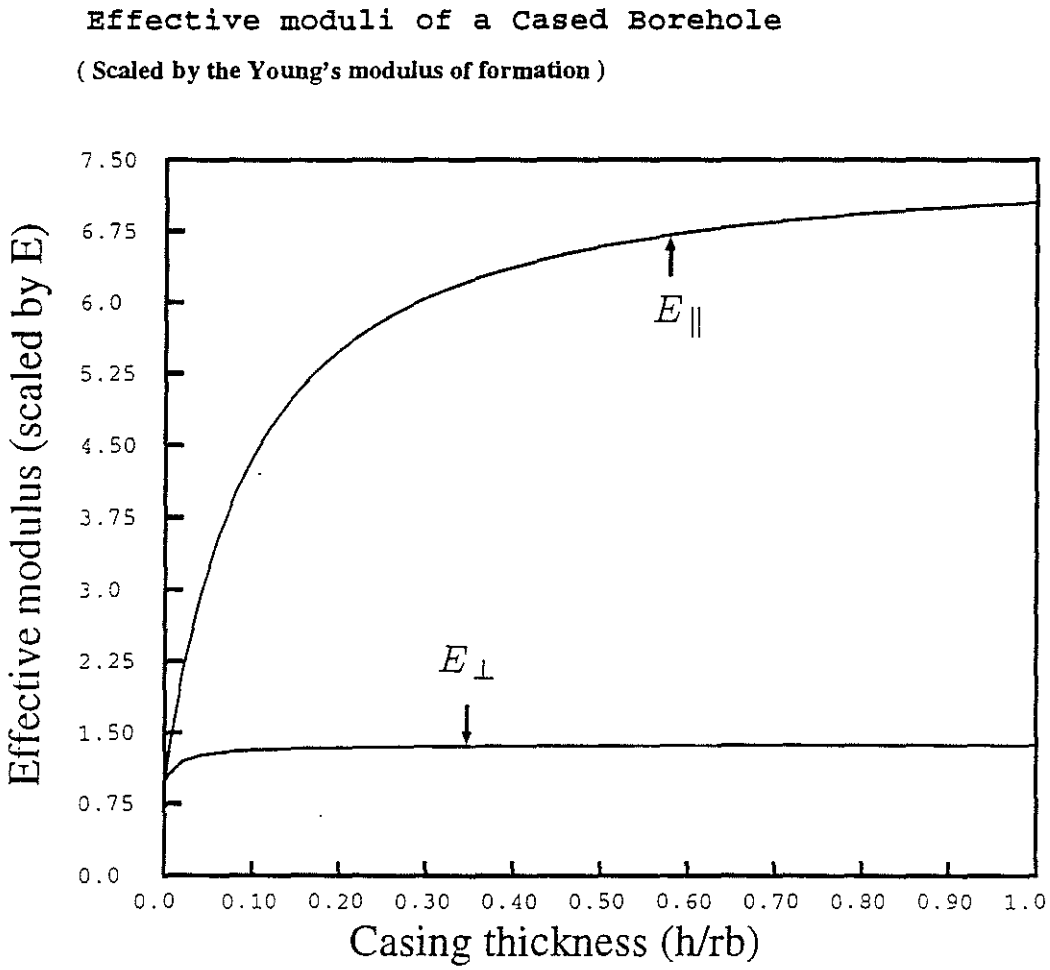

Figure 5: Effective moduli of a cased borehole as a function of casing thickness. The formation is Pierre shale (soft).

Radius(cm)	VP(km/s)	VS(km/s)	RHO(g/cm3)
10.16	1.50	0.0	1.00
12.19	6.10	3.35	7.50
infinity	Poisson's solid		

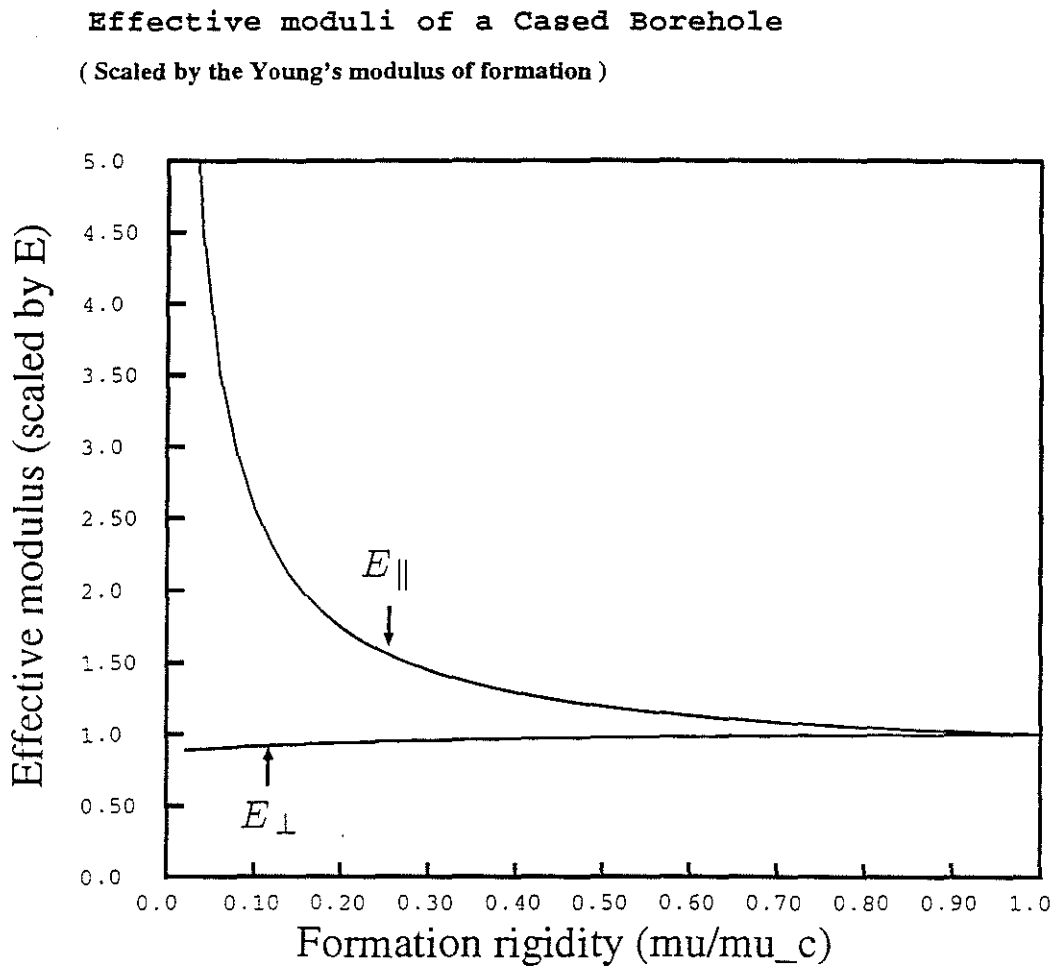

Figure 6: Effective moduli of a cased borehole as a function of formation rigidity.

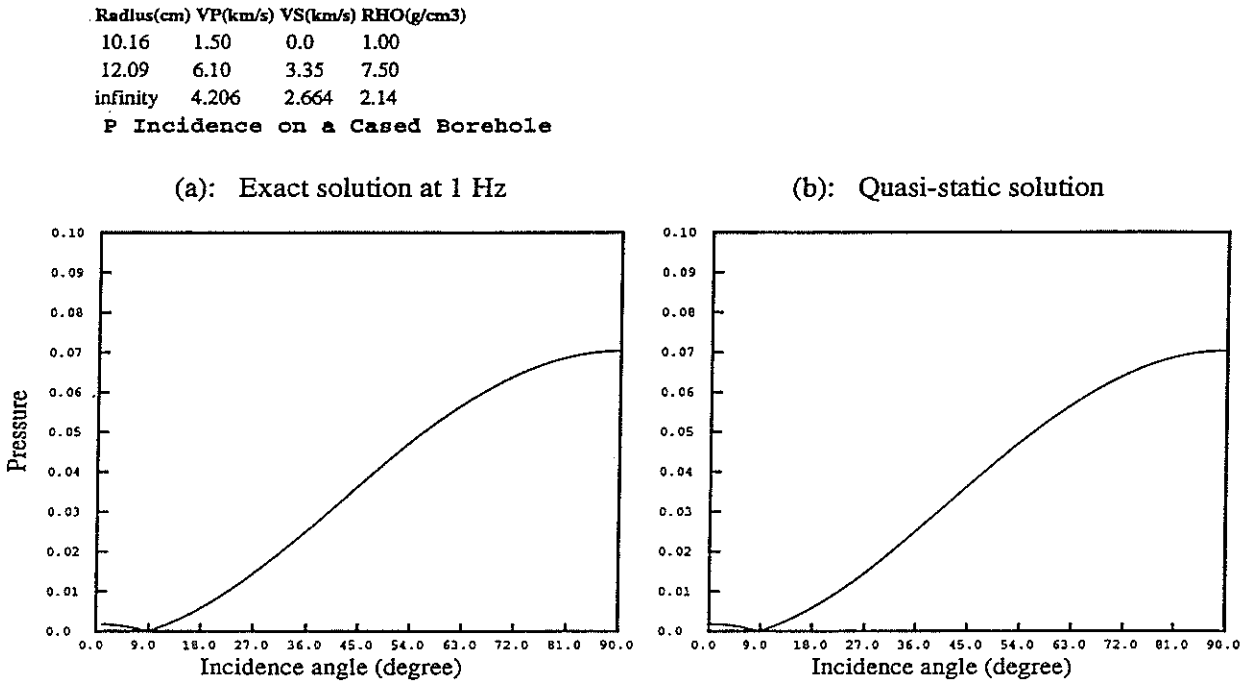

Figure 7: Comparison between the exact solution and the quasi-static approximation. The formation is Berea sandstone (hard). The incident wave is a plane P wave. The exact solution is computed by the global matrix method at 1 Hz.

Radius(cm)	VP(km/s)	VS(km/s)	RHO(g/cm3)
10.16	1.50	0.0	1.00
12.09	6.10	3.35	7.50
infinity	2.074	0.869	2.00

P Incidence on a Cased Borehole

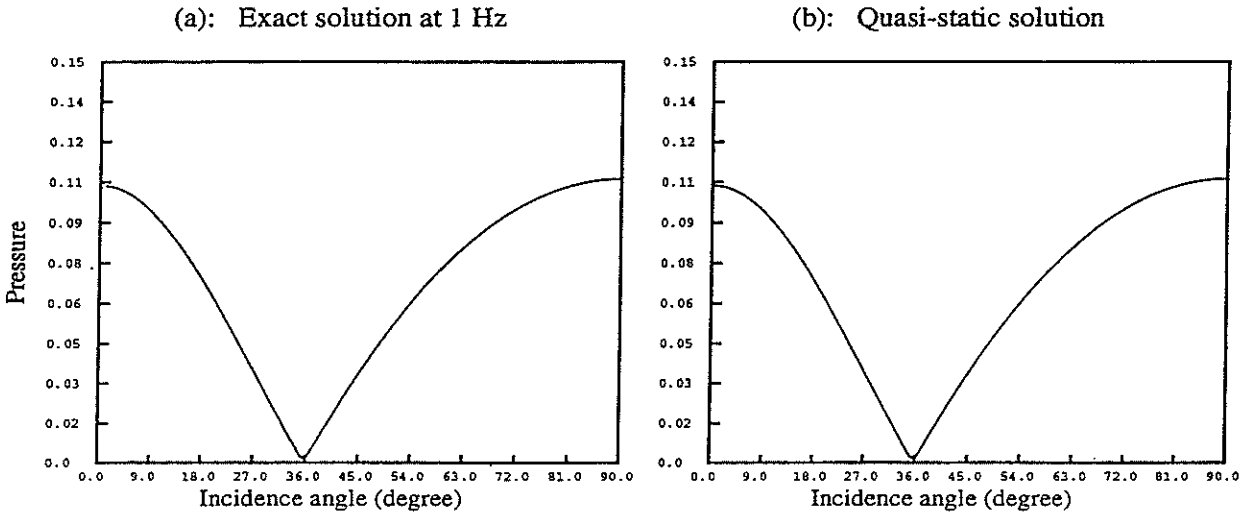

Figure 8: Same as that in Figure 7 except the formation is Pierre shale (soft).

Radius(cm)	VP(km/s)	VS(km/s)	RHO(g/cm3)
10.16	1.50	0.0	1.00
12.09	6.10	3.35	7.50
infinity	4.206	2.664	2.14

SV Incidence on a Cased Borehole

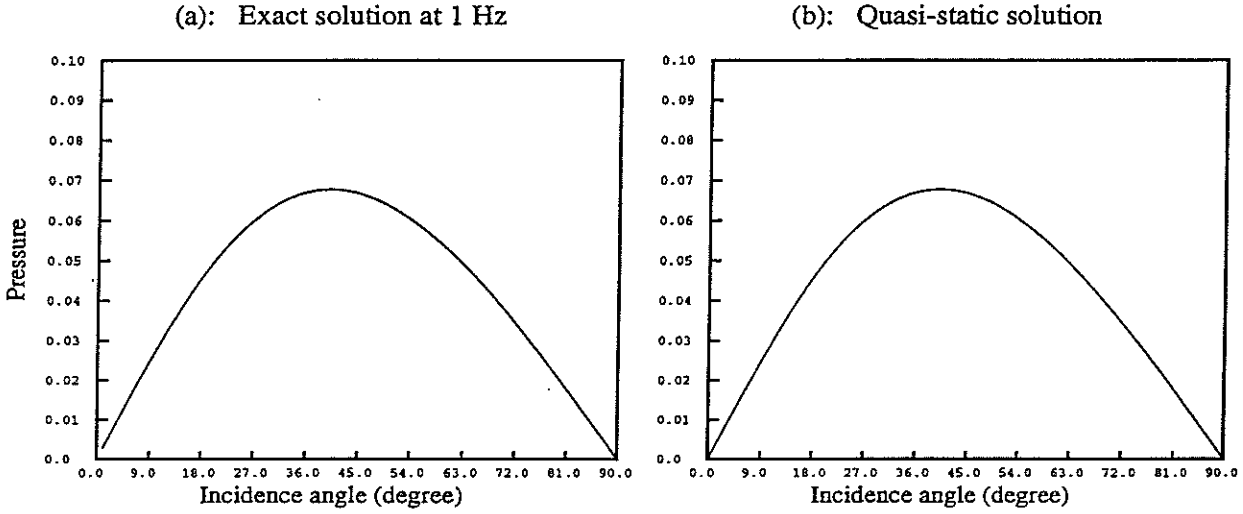

Figure 9: Same as that in Figure 7 except the incident wave is a plane SV wave.

Radius(cm)	VP(km/s)	VS(km/s)	RHO(g/cm3)
10.16	1.50	0.0	1.00
12.09	6.10	3.35	7.50
infinity	2.074	0.869	2.00

SV Incidence on a Cased Borehole

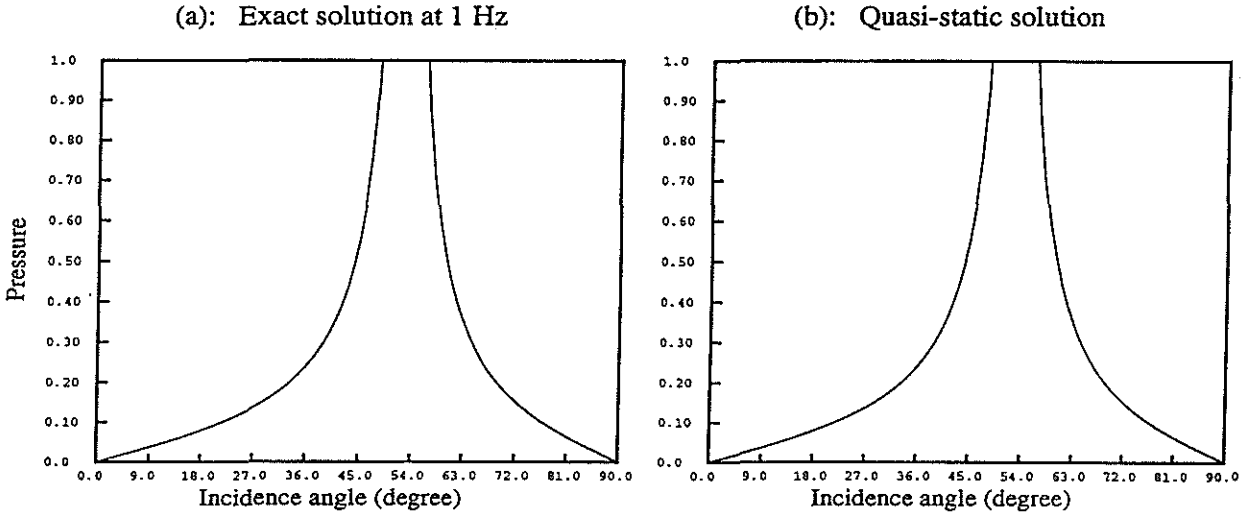

Figure 10: Same as that in Figure 8 except the incident wave is a plane SV wave.

Radius(cm)	VP(km/s)	VS(km/s)	RHO(g/cm3)
10.16	1.50	0.0	1.00
12.09	6.10	3.35	7.50
infinity	4.206	2.664	2.14

mode = 0, frequency = 100 Hz

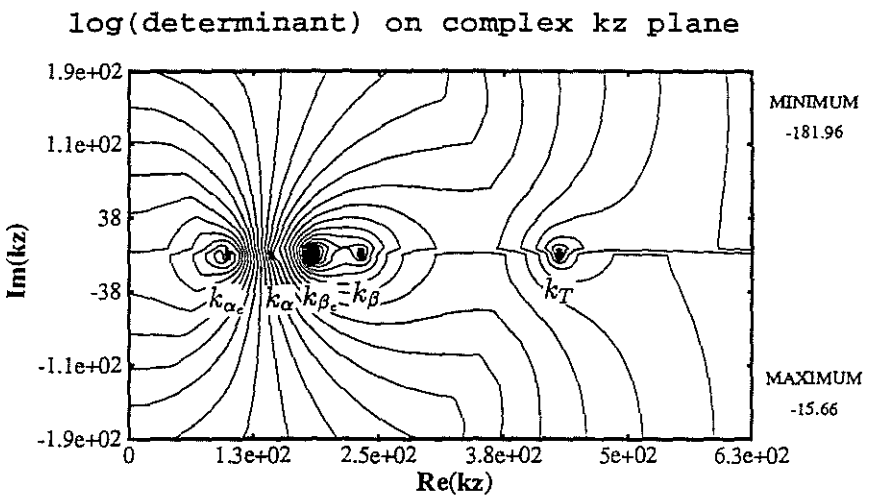

mode = 0, frequency = 2000 Hz

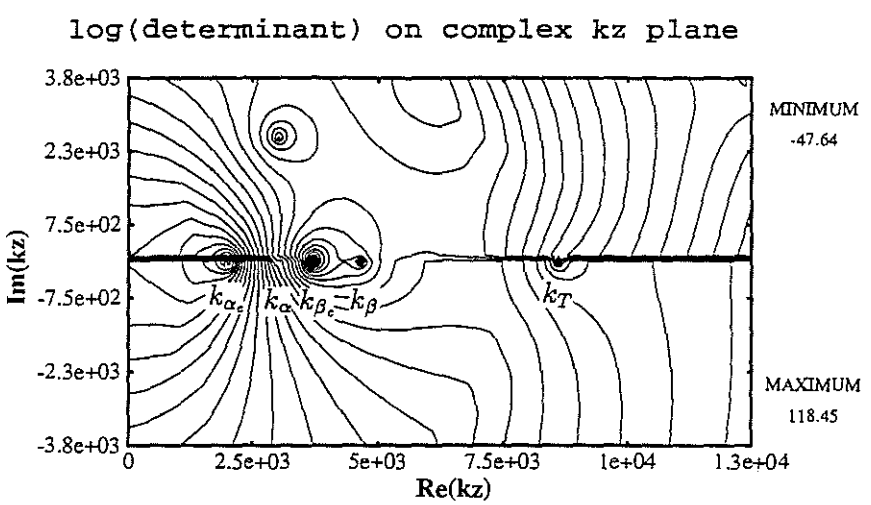

Figure 11: Contour plots of the dispersion function $F(k_z)$ for the monopole mode n = 0 for the hard formation at frequency 100 Hz (top) and 2000 Hz (bottom). The horizontal axis is the real part of k_z, the vertical axis is the imaginary part. The surface mode and branch cuts on the real axis are labeled.

Radius(cm)	VP(km/s)	VS(km/s)	RHO(g/cm3)
10.16	1.50	0.0	1.00
12.09	6.10	3.35	7.50
infinity	4.206	2.664	2.14

mode = 1, frequency = 100 Hz

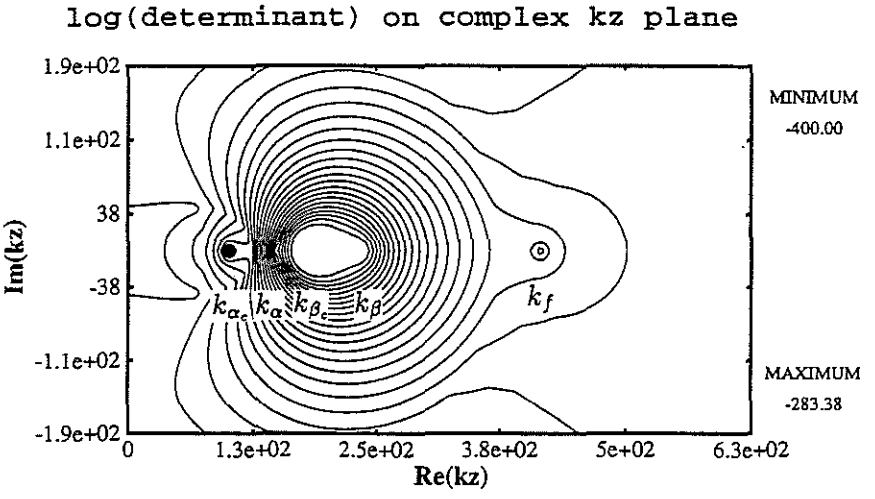

mode = 1, frequency = 2000 Hz

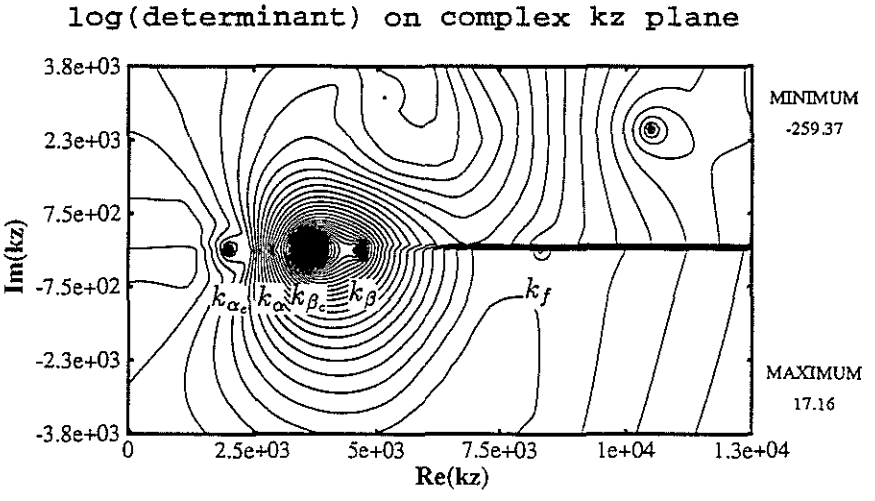

Figure 12: Same as Figure 11 except for the dipole mode n = 1.

Radius(cm)	VP(km/s)	VS(km/s)	RHO(g/cm3)
10.16	1.50	0.0	1.00
12.09	6.10	3.35	7.50
infinity	2.074	0.869	2.00

mode = 0, frequency = 100 Hz

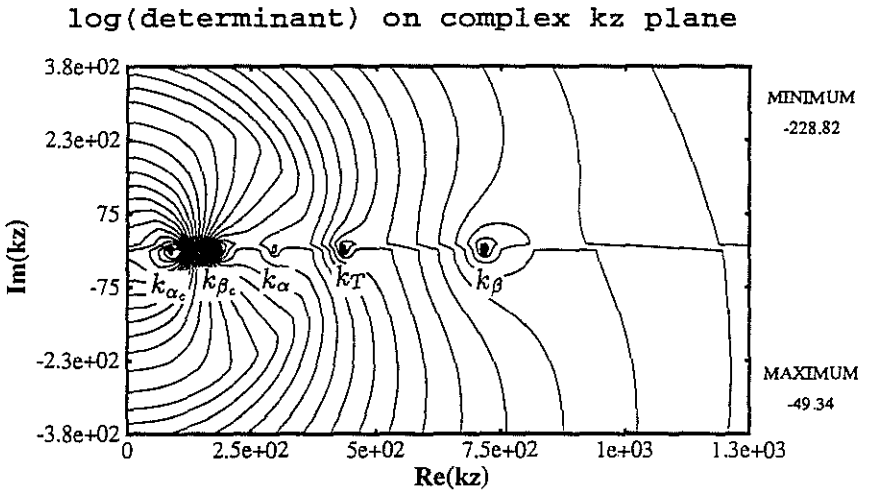

mode = 0, frequency = 2000 Hz

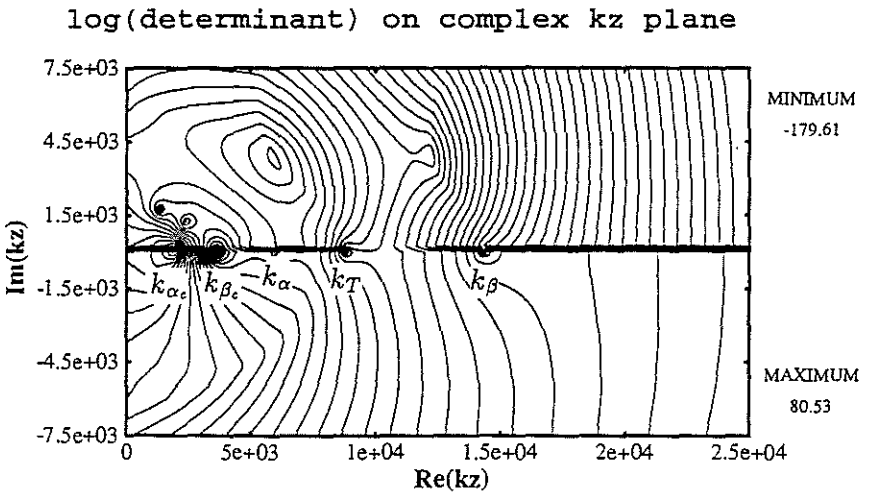

Figure 13: Same as Figure 11 except for the soft formation.

Radius(cm)	VP(km/s)	VS(km/s)	RHO(g/cm3)
10.16	1.50	0.0	1.00
12.09	6.10	3.35	7.50
infinity	2.074	0.869	2.00

mode = 1, frequency = 100 Hz

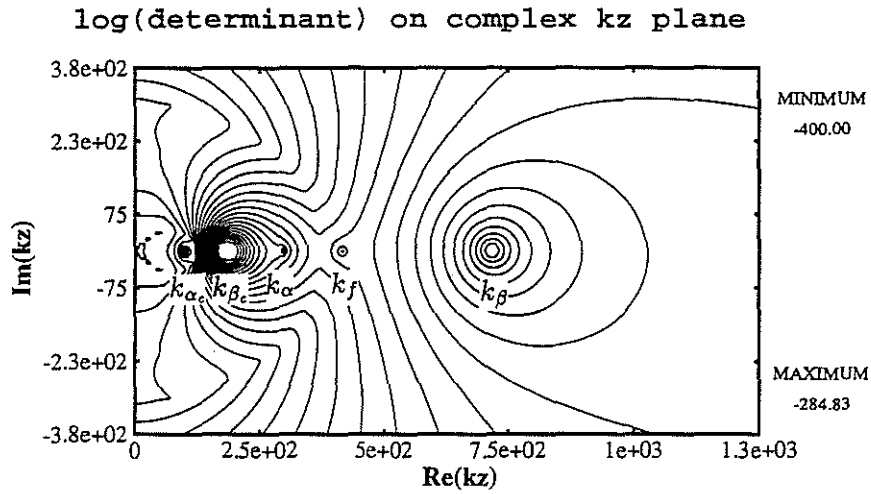

mode = 1, frequency = 2000 Hz

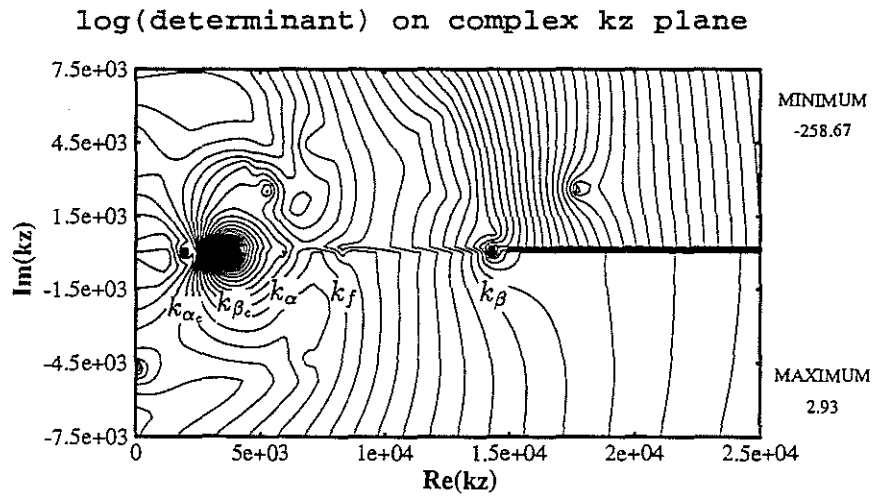

Figure 14: Same as Figure 13 except for the dipole mode n = 1.

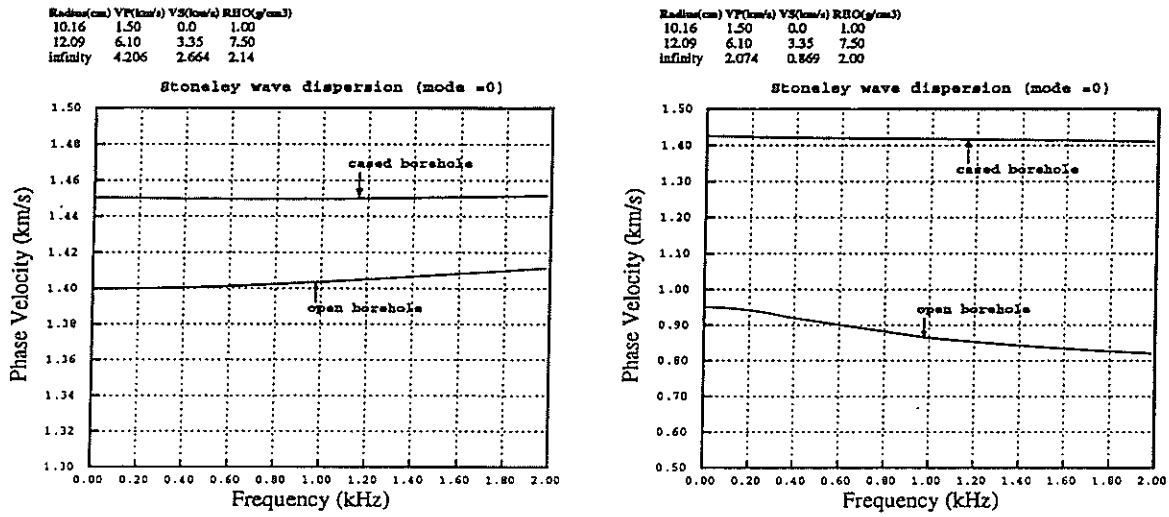

Figure 15: Dispersion of the Stoneley wave in a cased or an open borehole. The left panel is for the hard formation. The right panel is for the soft formation.

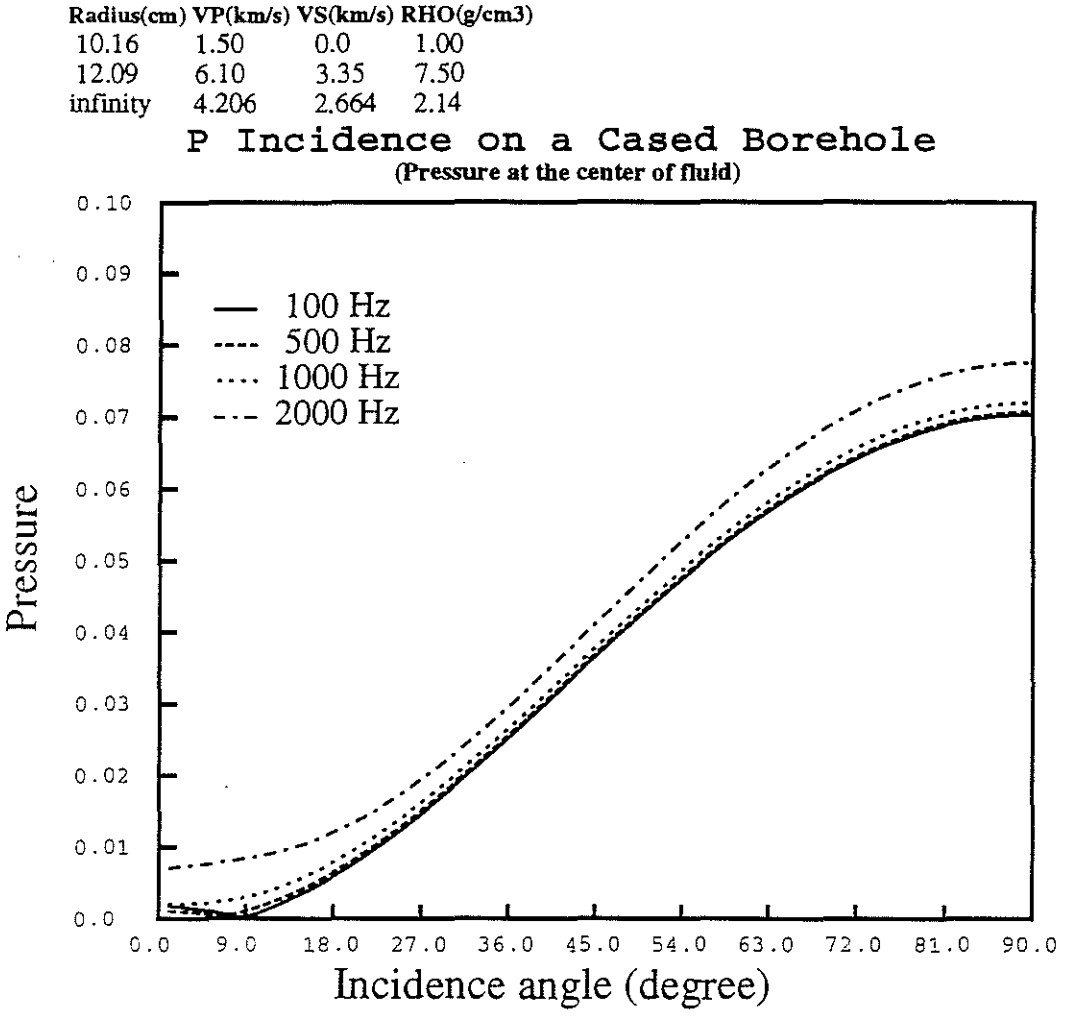

Figure 16: Pressure in a cased borehole as a function of incidence angle. The formation is Berea sandstone (hard). The incident wave is a plane P wave. Calculations are made at frequencies 100 Hz, 500 Hz, 1000 Hz, and 2000 Hz.

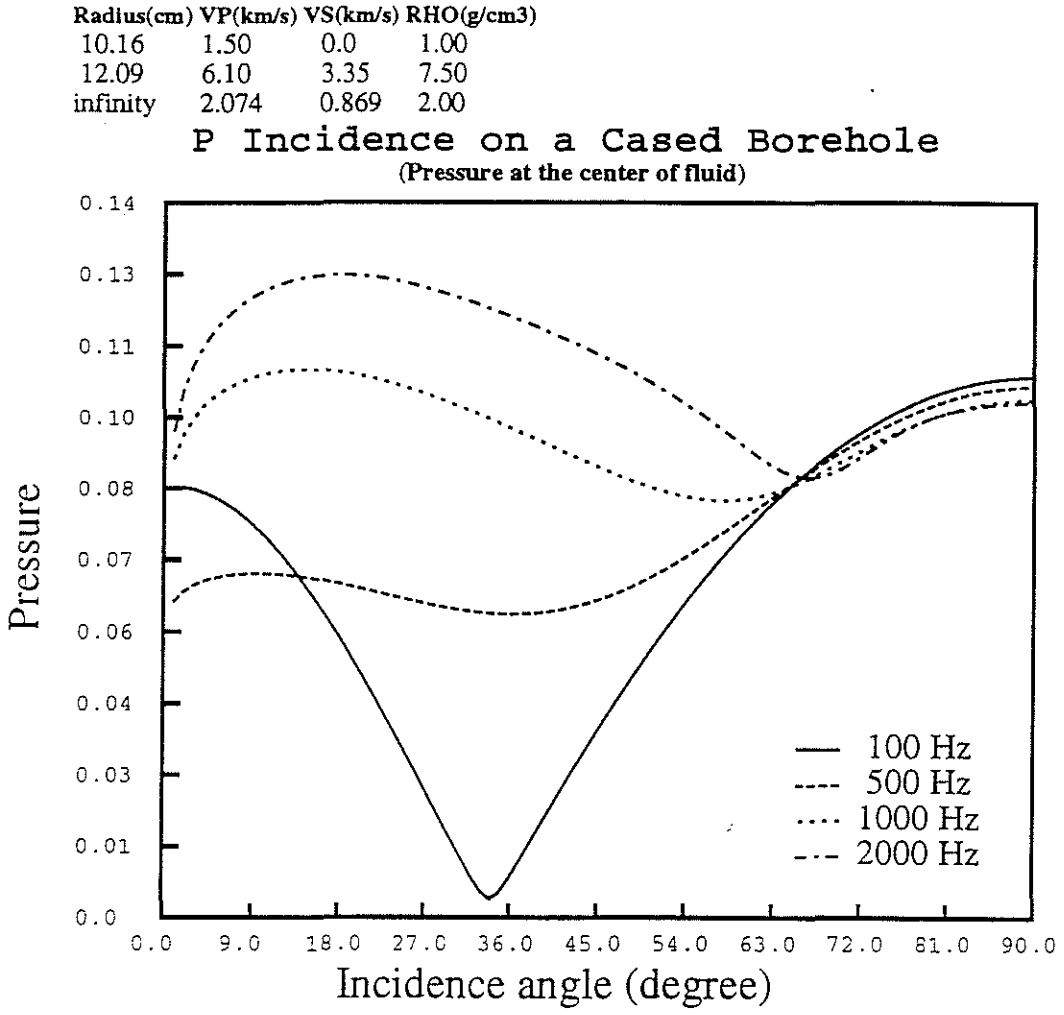

Figure 17: Same as Figure 16 except for the soft formation (Pierre shale).

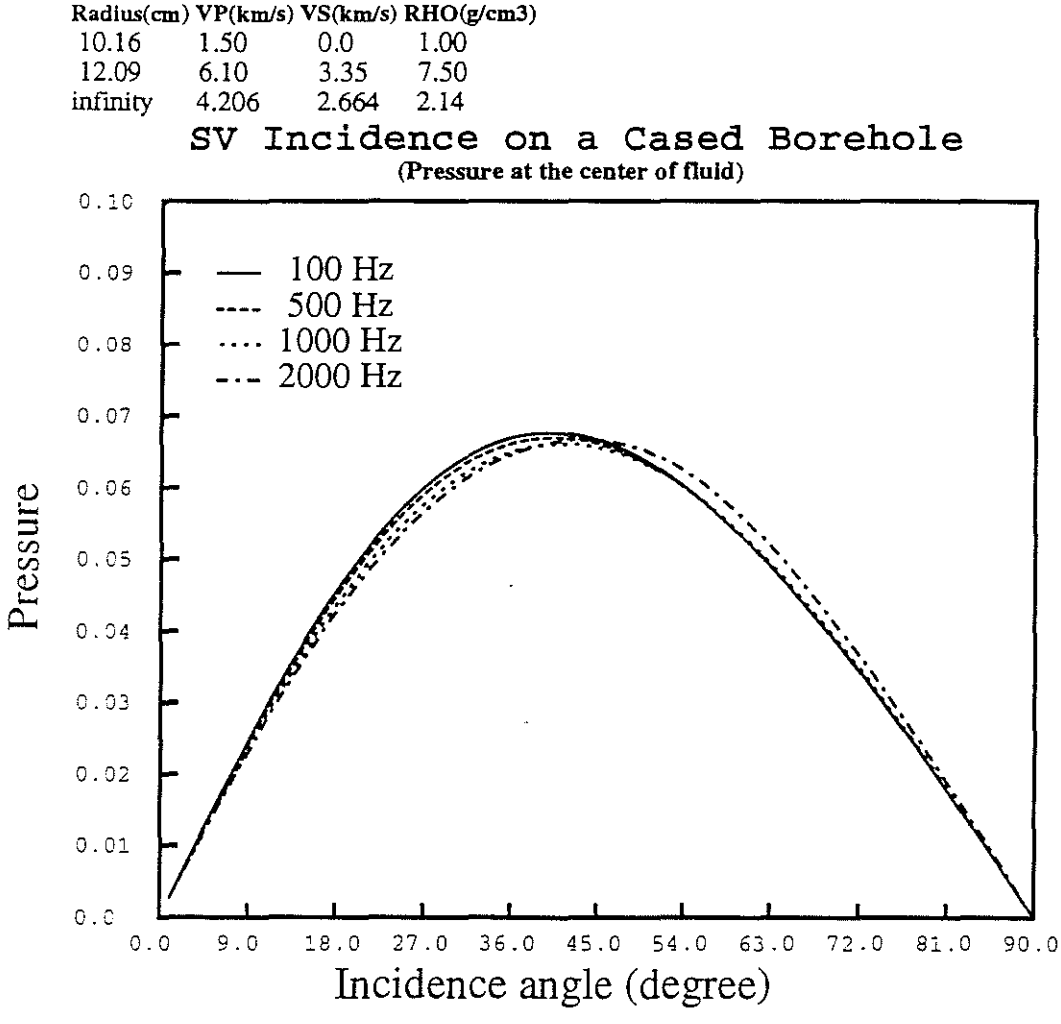

Figure 18: Same as Figure 16 except for a plane SV wave incidence.

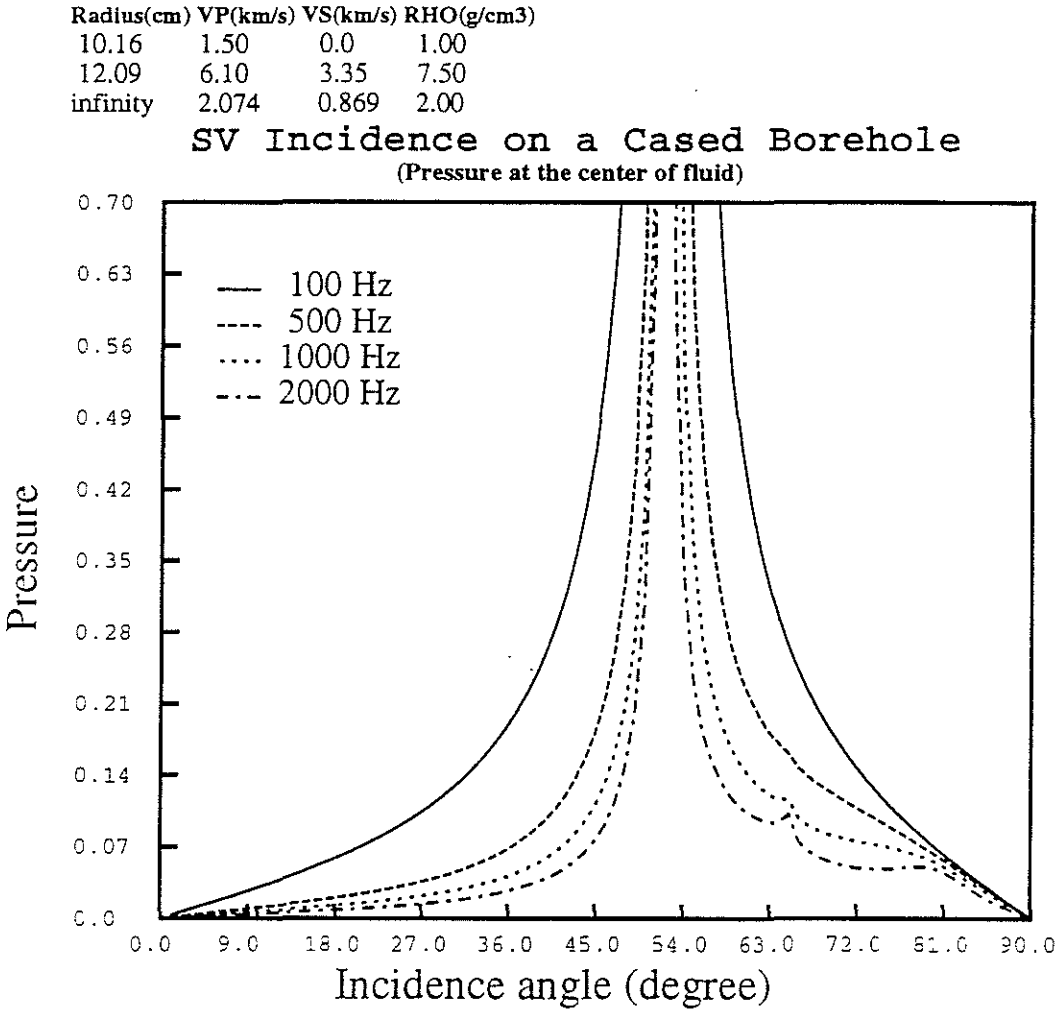

Figure 19: Same as Figure 17 except for a plane SV wave incidence.

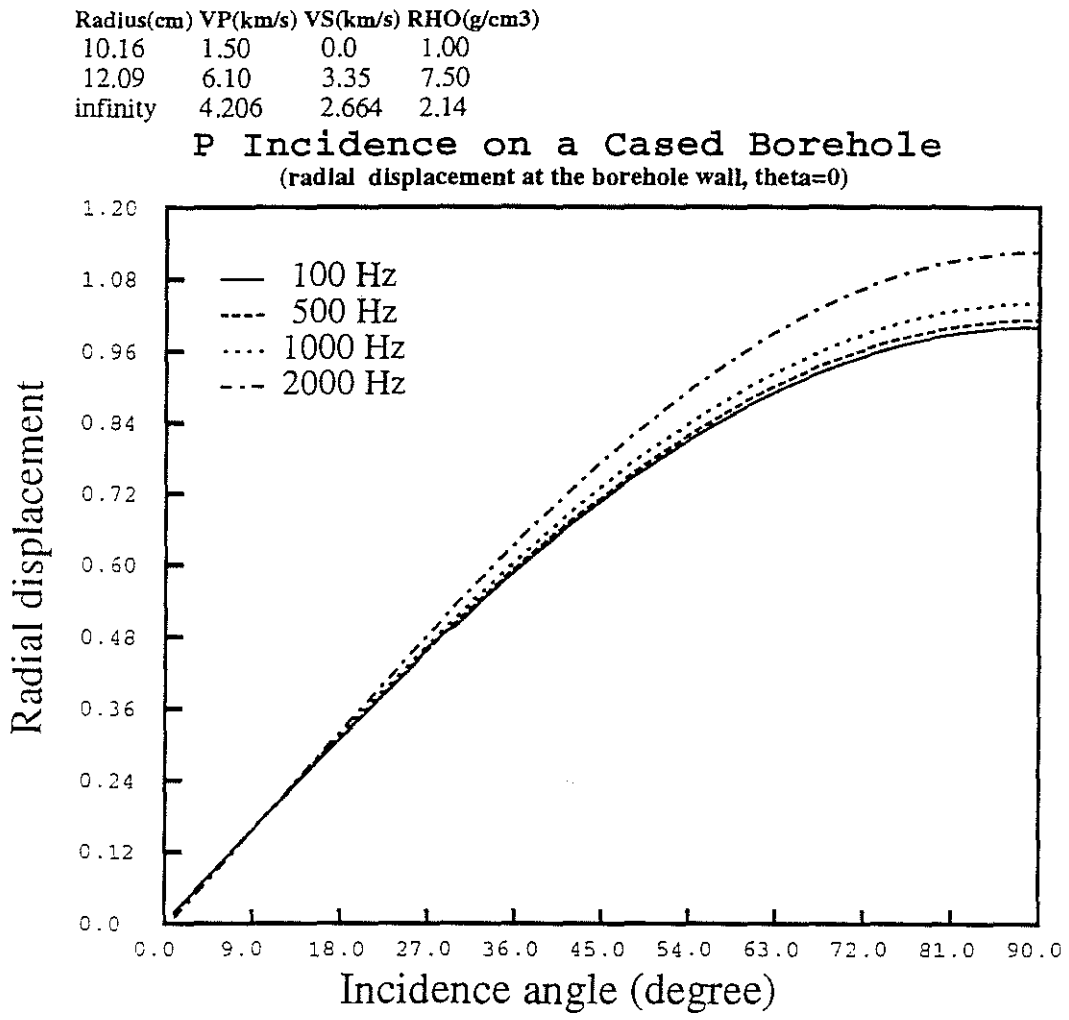

Figure 20: Radial component of solid displacement on the borehole wall for an incident plane P wave. The formation is Berea sandstone (hard). Calculations are made at frequencies 100 Hz, 500 Hz, 1000 Hz, and 2000 Hz.

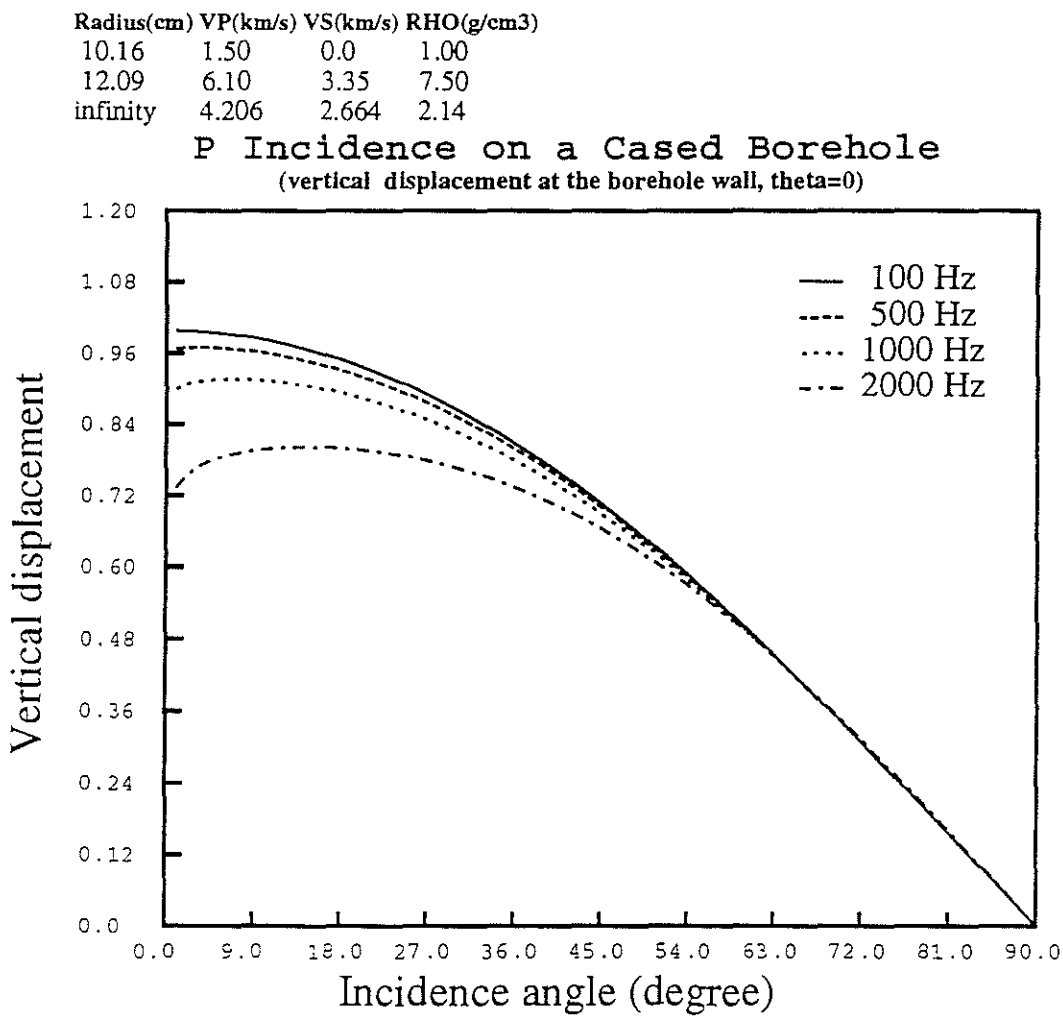

Figure 21: Vertical component of solid displacement on the borehole wall for an incident plane P wave. Others are the same as Figure 20.

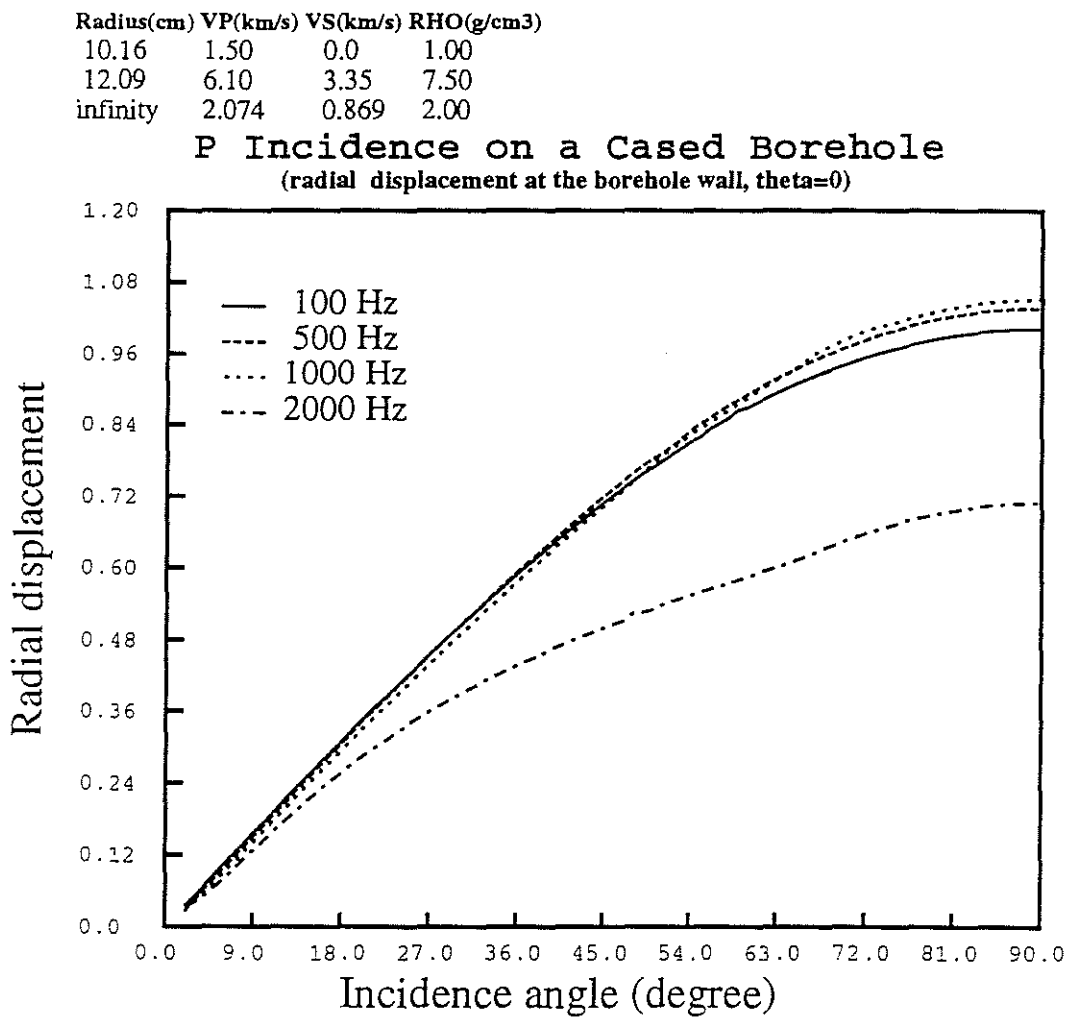

Figure 22: Radial component of solid displacement on the borehole wall for an incident plane P wave. The formation is Pierre shale (soft).

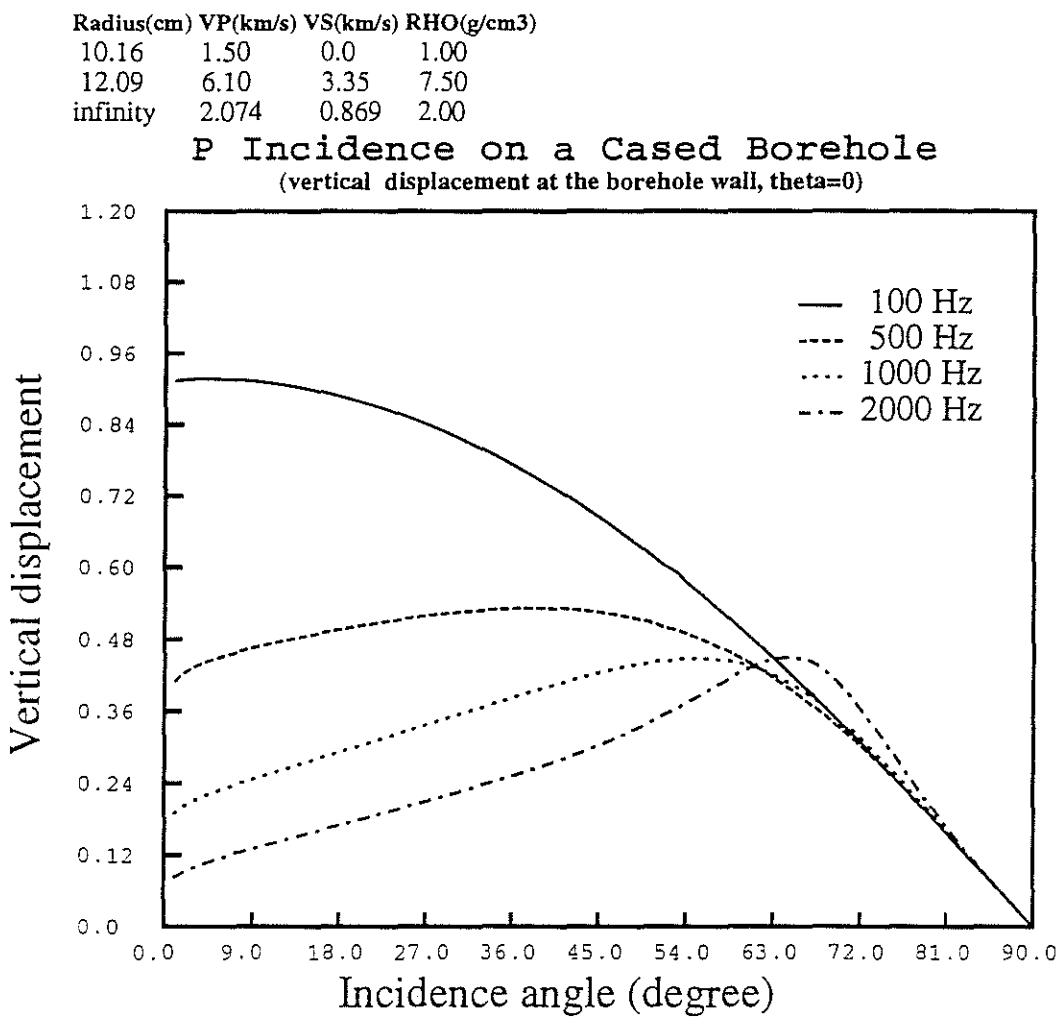

Figure 23: Vertical component of solid displacement on the borehole wall for an incident plane P wave. The formation is Pierre shale (soft).

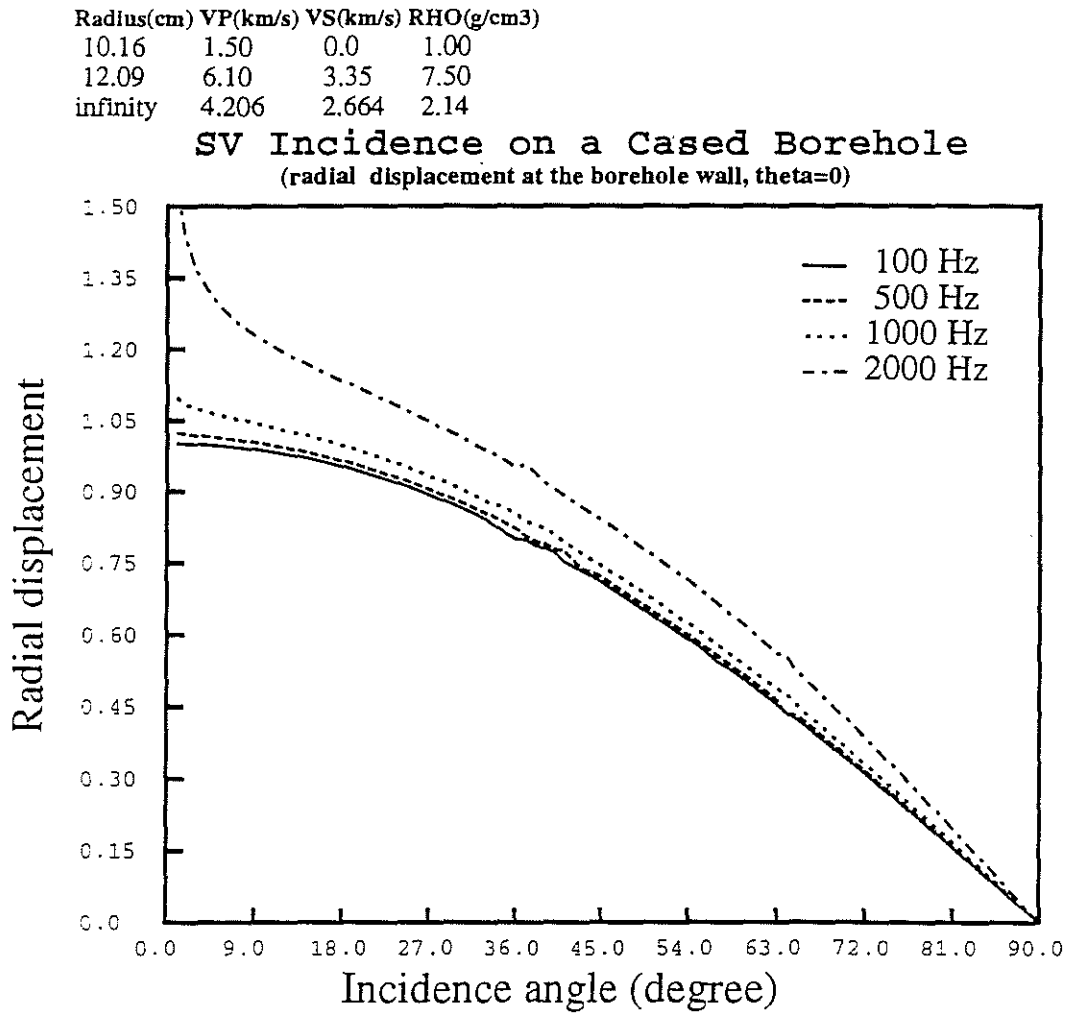

Figure 24: Same as Figure 20 except for an incident plane SV wave.

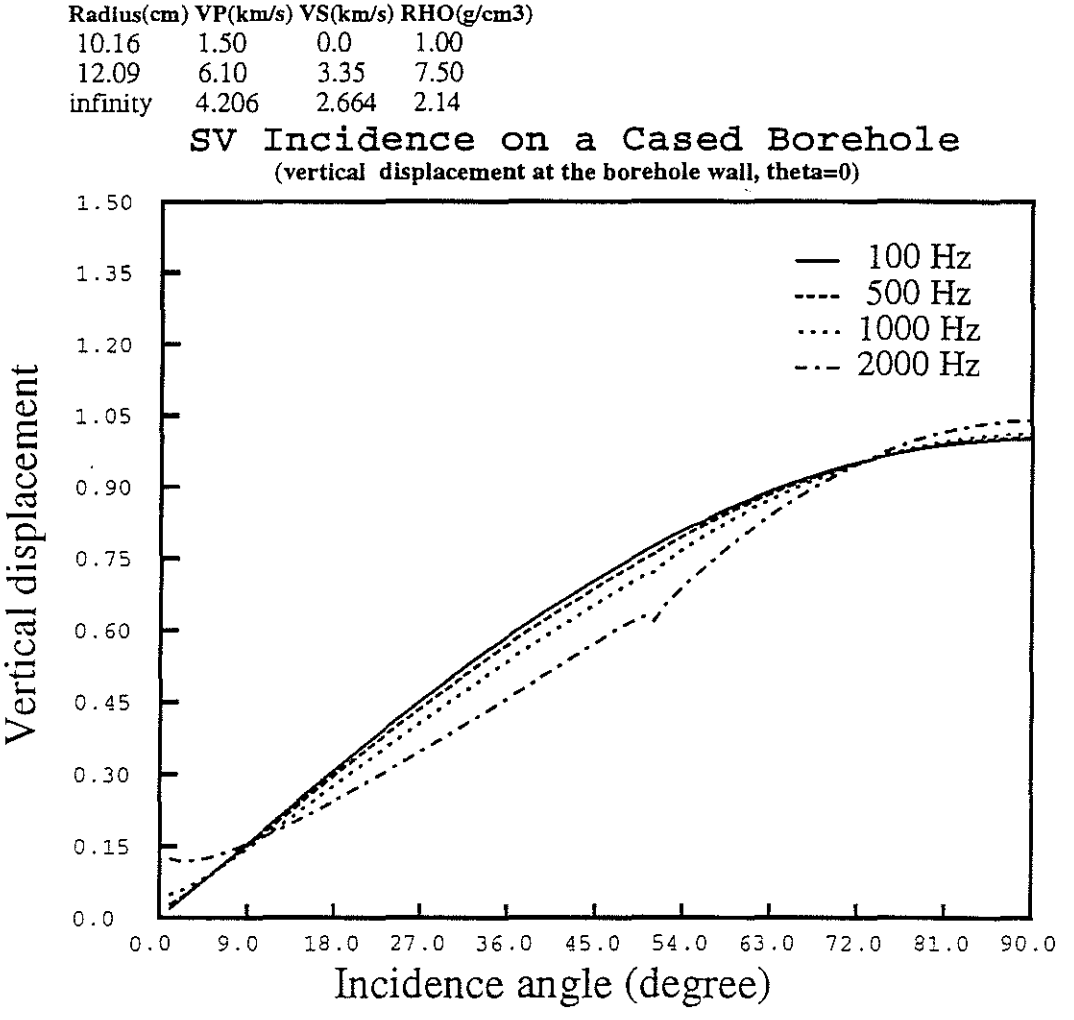

Figure 25: Same as Figure 21 except for an incident plane SV wave.

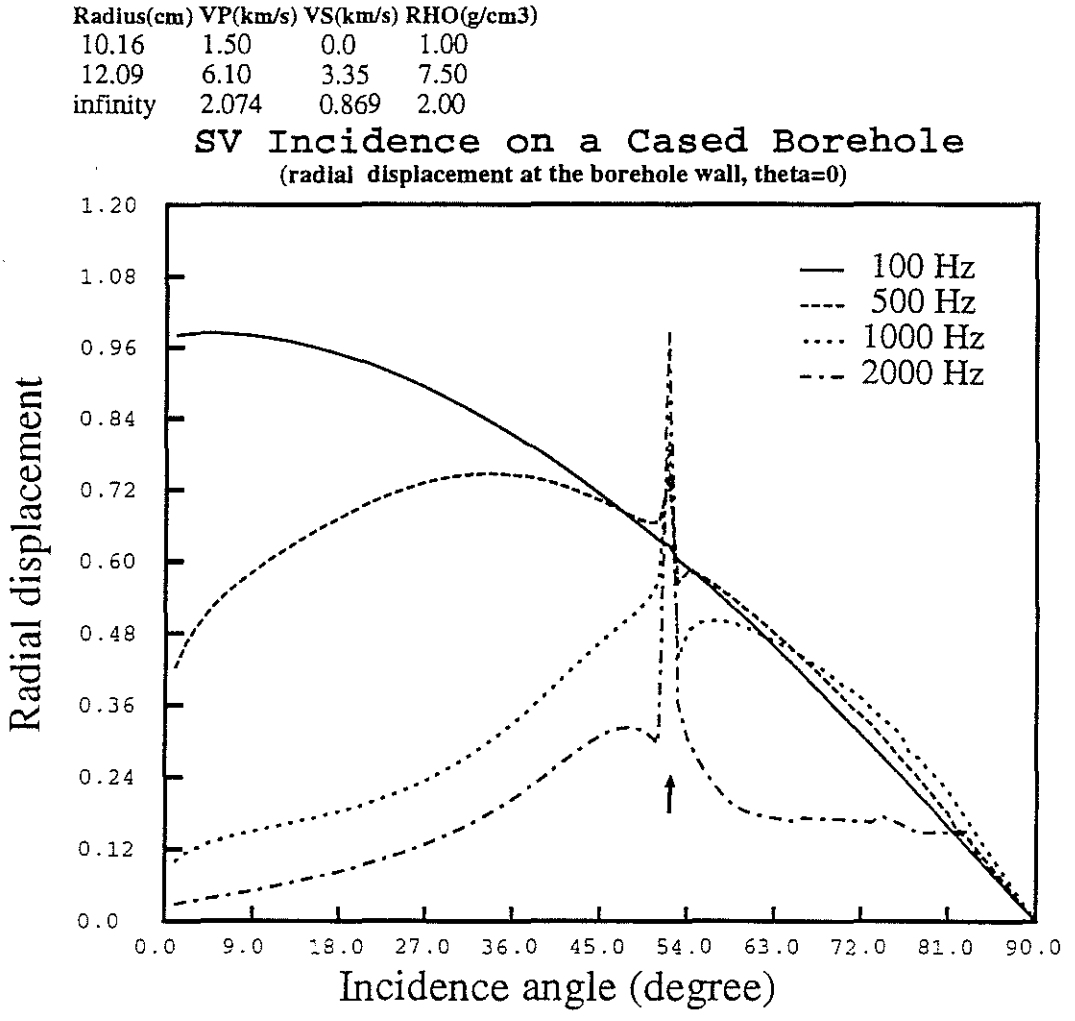

Figure 26: Same as Figure 22 except for an incident plane SV wave.

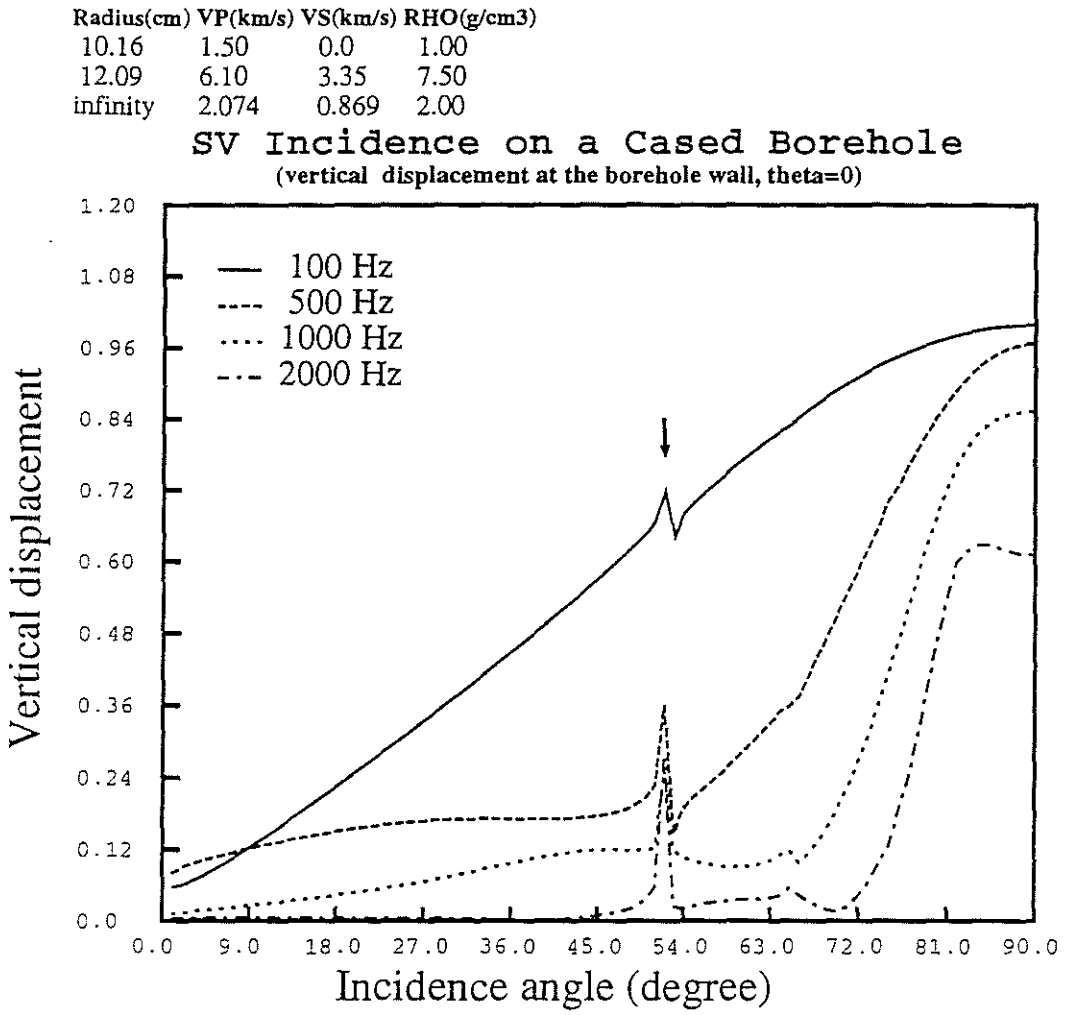

Figure 27: Same as Figure 23 except for an incident plane SV wave.

Radius(cm)	VP(km/s)	VS(km/s)	RHO(g/cm3)
10.16	1.50	0.0	1.00
12.09	6.10	3.35	7.50
infinity	4.206	2.664	2.14

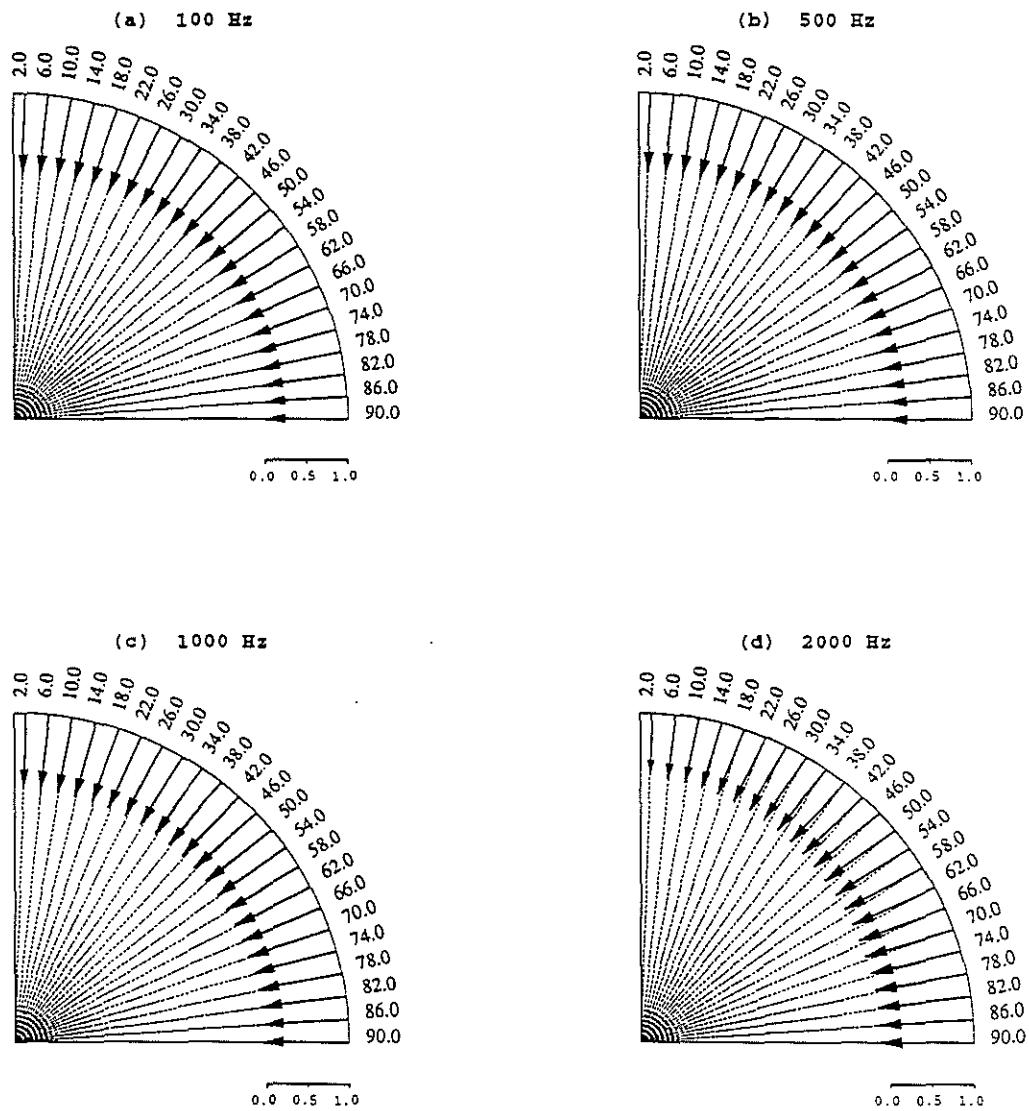

Figure 28: Particle motion on the borehole wall as a function of angle of incidence for an incident plane P wave. The formation is Berea sandstone (hard). Calculations are made at frequencies 100 Hz, 500 Hz, 1000 Hz, and 2000 Hz.

Radius(cm)	VP(km/s)	VS(km/s)	RHO(g/cm3)
10.16	1.50	0.0	1.00
12.09	6.10	3.35	7.50
infinity	2.074	0.869	2.00

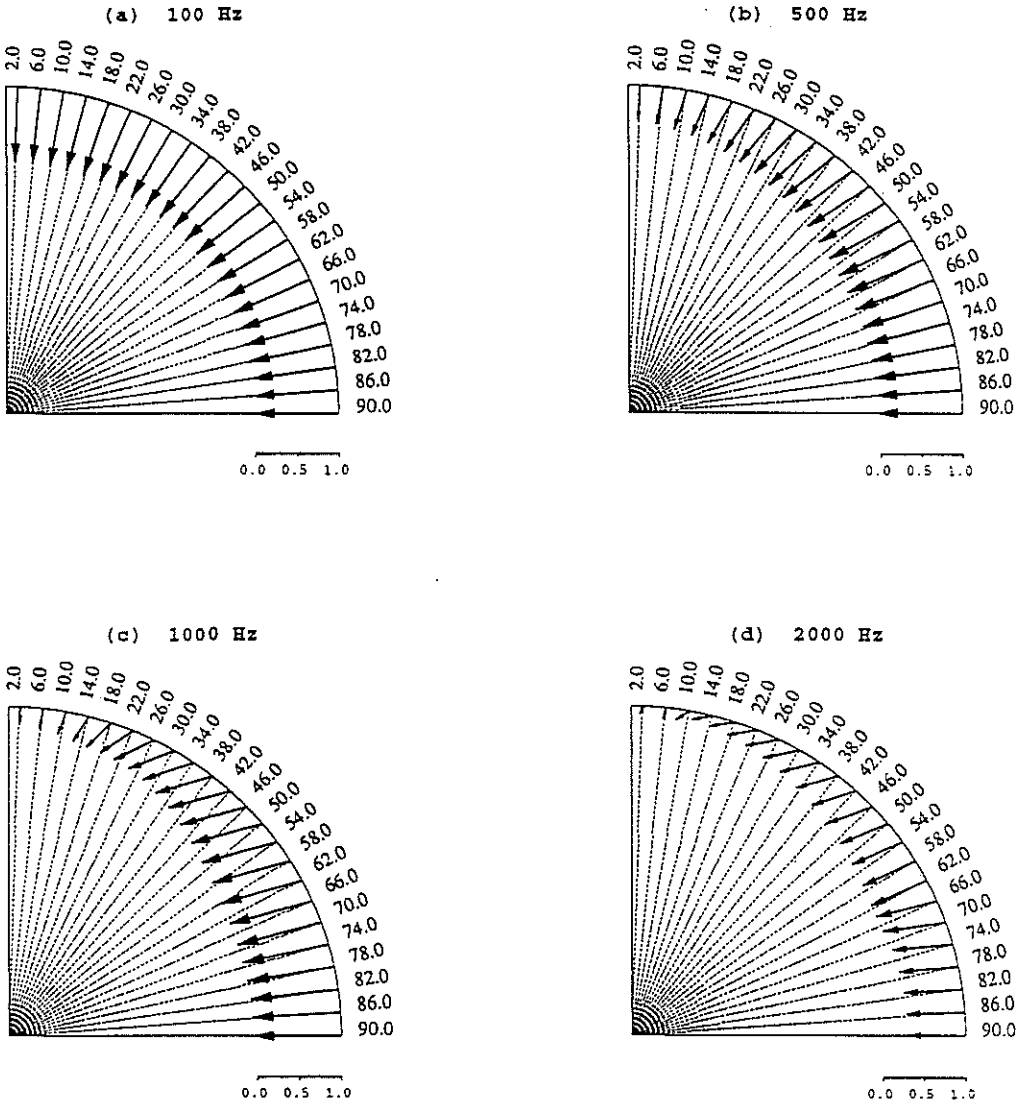

Figure 29: Same as Figure 28 except for the soft formation (Pierre shale).

Radius(cm)	VP(km/s)	VS(km/s)	RHO(g/cm3)
10.16	1.50	0.0	1.00
12.09	6.10	3.35	7.50
infinity	4.206	2.664	2.14

SV Incidence on a Cased Borehole
(90 degree rotation applied)

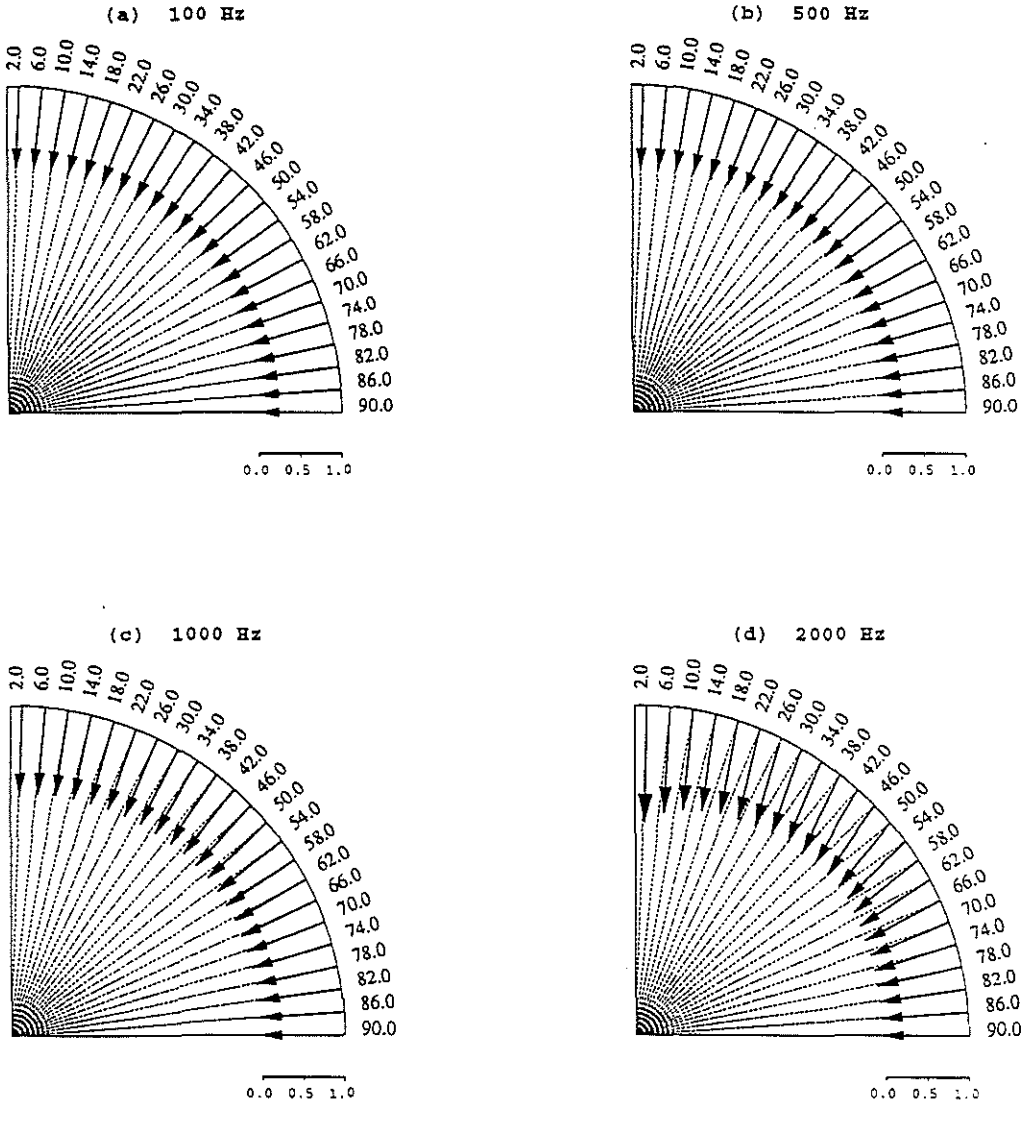

Figure 30: Same as Figure 28 except for an incident plane SV wave.

Radius(cm)	VP(km/s)	VS(km/s)	RHO(g/cm3)
10.16	1.50	0.0	1.00
12.09	6.10	3.35	7.50
infinity	2.074	0.869	2.00

SV Incidence on a Cased Borehole
(90 degree rotation applied)

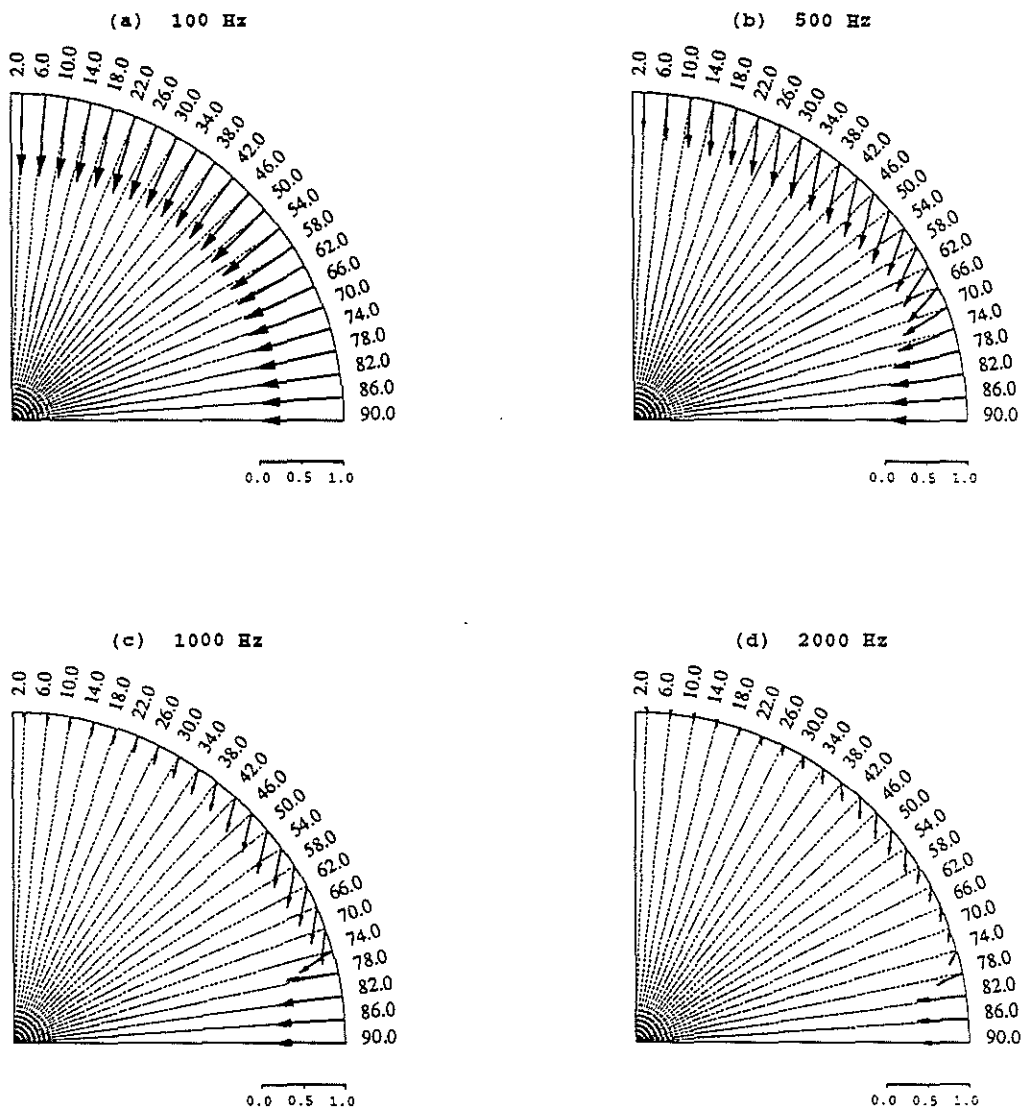

Figure 31: Same as Figure 30 except for the soft formation (Pierre shale).

Radius(cm)	VP(km/s)	VS(km/s)	RHO(g/cm3)
10.16	1.50	0.0	1.00
12.09	6.10	3.35	7.50
infinity	4.206	2.664	2.14

Frequency: 1000 Hz, P incidence at: 45 degree

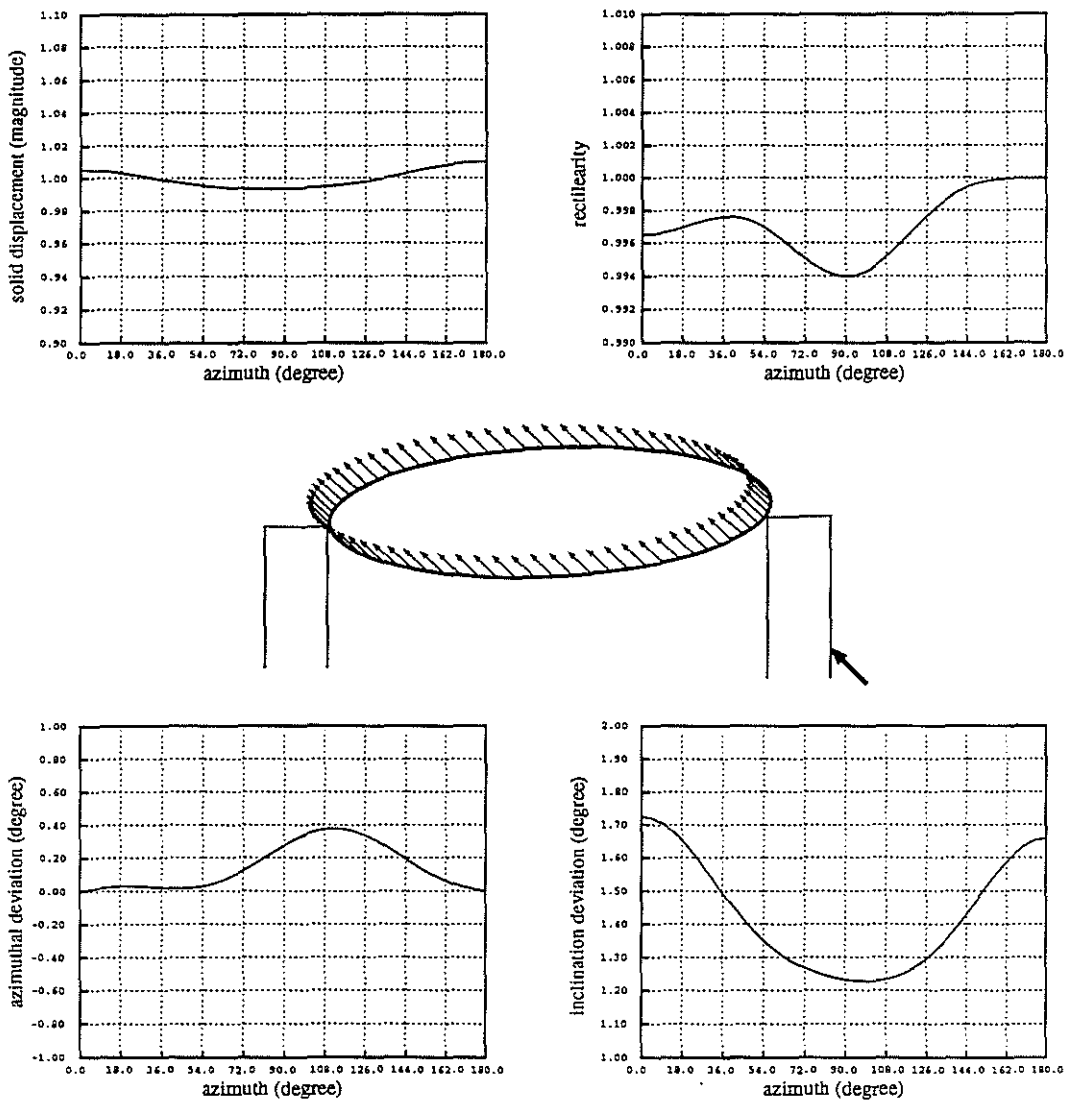

Figure 32: Solid displacement on the borehole wall as a function of the azimuthal orientation of the geophone for an incident plane P wave. The formation is Berea sandstone (hard). Calculation is made with $\delta = 45^o$ and frequency 1000 Hz.

Radius(cm)	VP(km/s)	VS(km/s)	RHO(g/cm3)
10.16	1.50	0.0	1.00
12.09	6.10	3.35	7.50
infinity	2.074	0.869	2.00

Frequency: 1000 Hz, P incidence at: 45 degree

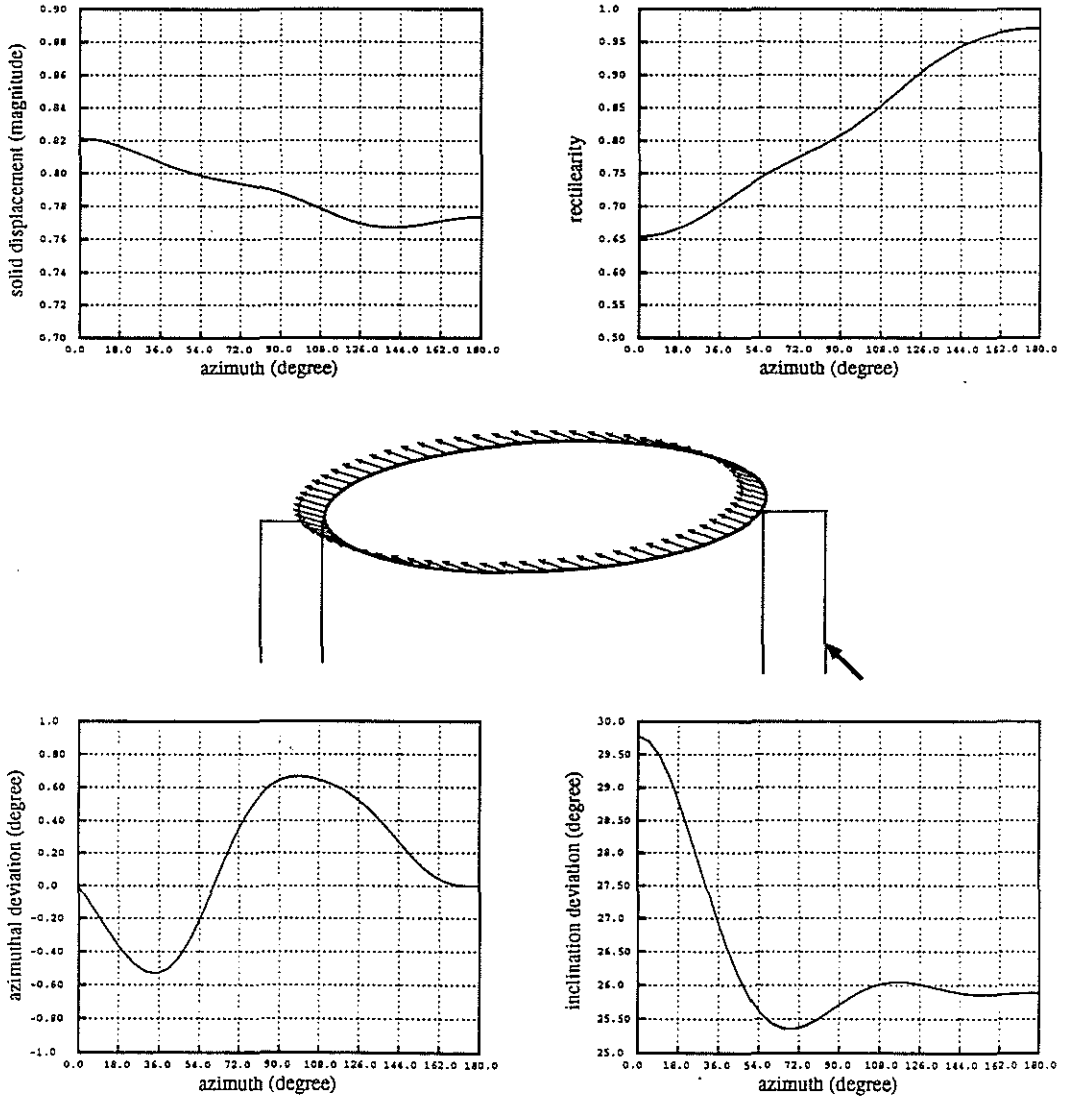

Figure 33: Same as Figure 32 except for the soft formation (Pierre shale).

Radius(cm)	VP(km/s)	VS(km/s)	RHO(g/cm3)
10.16	1.50	0.0	1.00
12.09	6.10	3.35	7.50
infinity	4.206	2.664	2.14

Frequency: 1000 Hz, SV incidence at: 45 degree

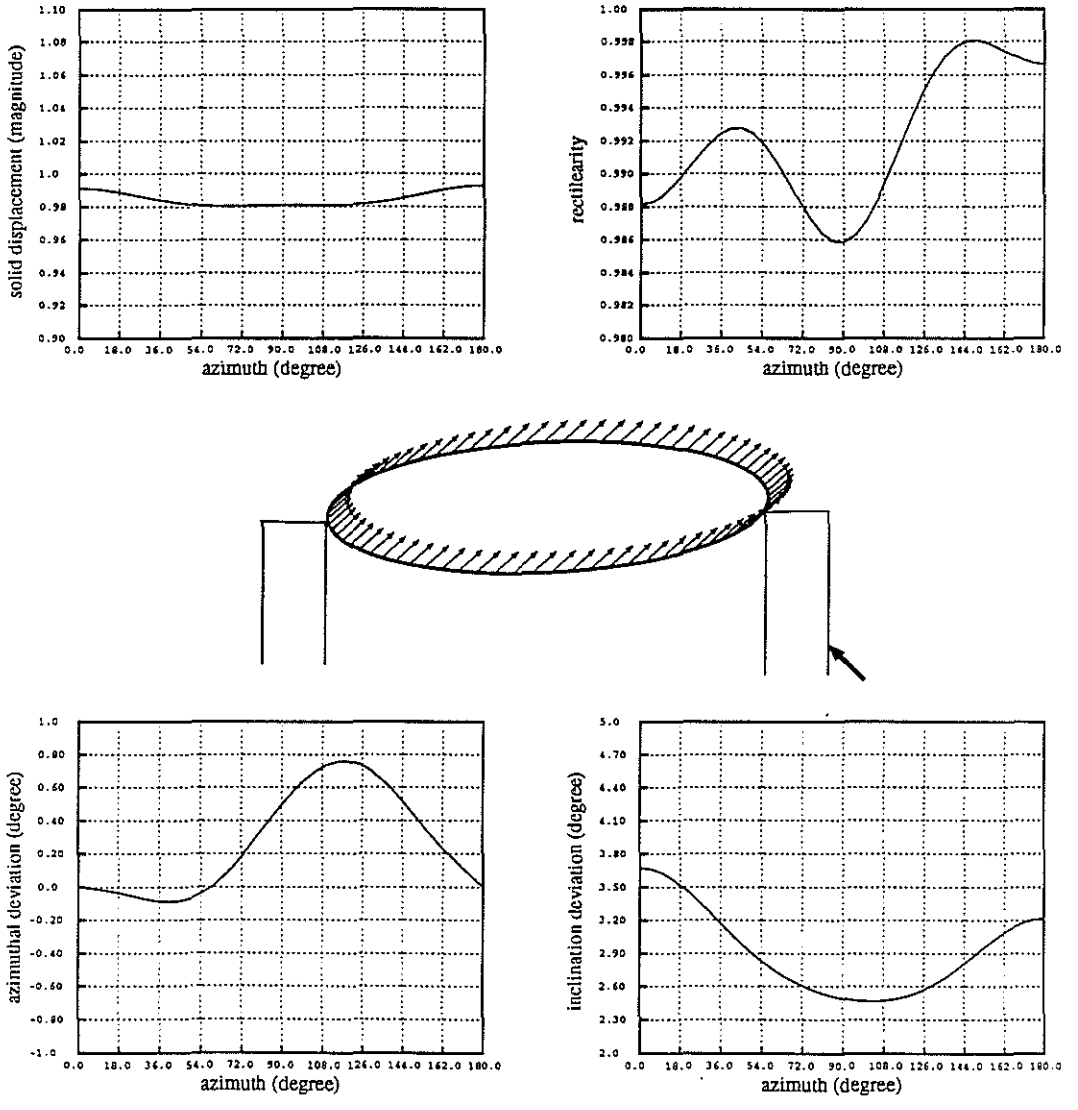

Figure 34: Same as Figure 32 except for an incident plane SV wave.

Radius(cm)	VP(km/s)	VS(km/s)	RHO(g/cm3)
10.16	1.50	0.0	1.00
12.09	6.10	3.35	7.50
infinity	2.074	0.869	2.00

Frequency: 1000 Hz, SV incidence at: 45 degree

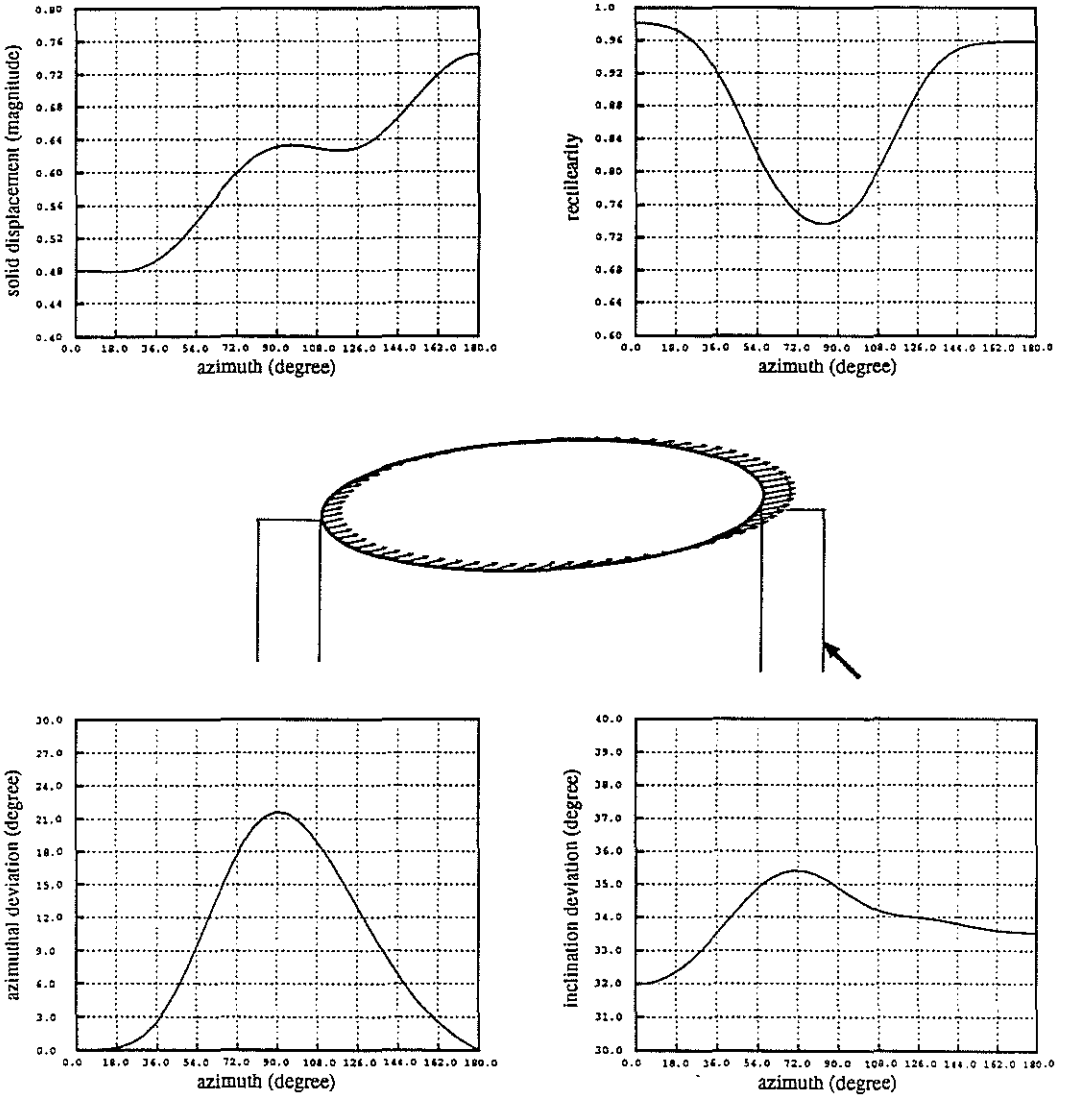

Figure 35: Same as Figure 34 except for the soft formation (Pierre shale).

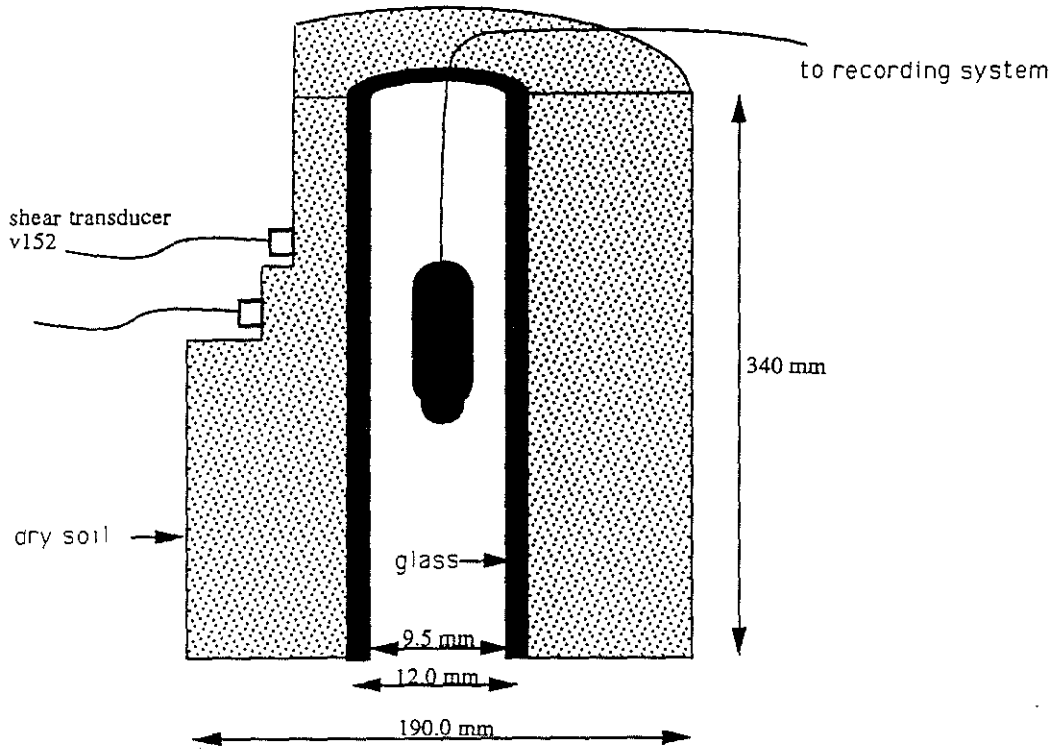

Figure 36: A laboratory setup for measuring the pressure in the fluid borehole due to a shear source in the formation. The glass pipe is buried in the soil and is dried for years.

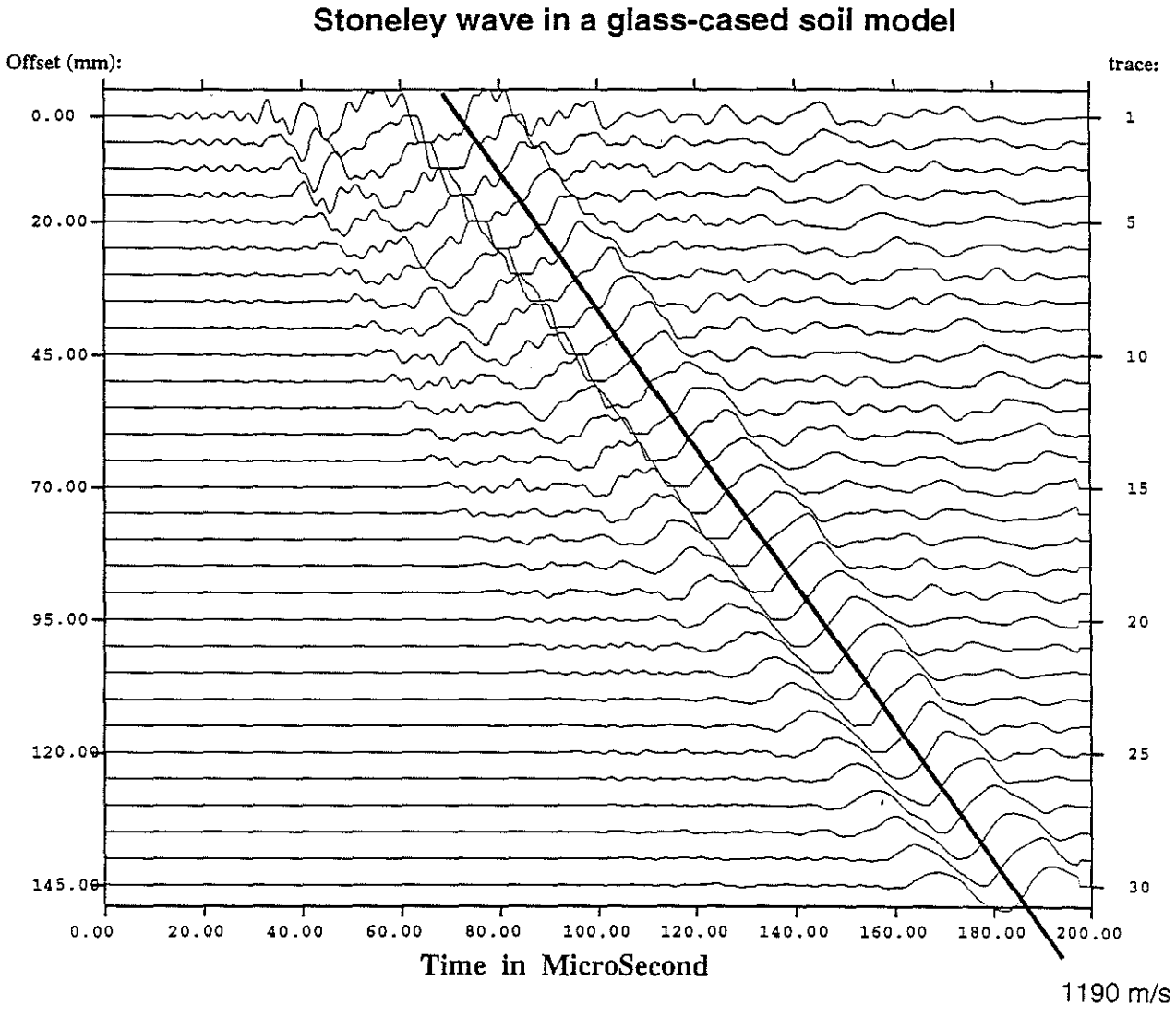

Figure 37: Stoneley waves in the glass-cased soil model.

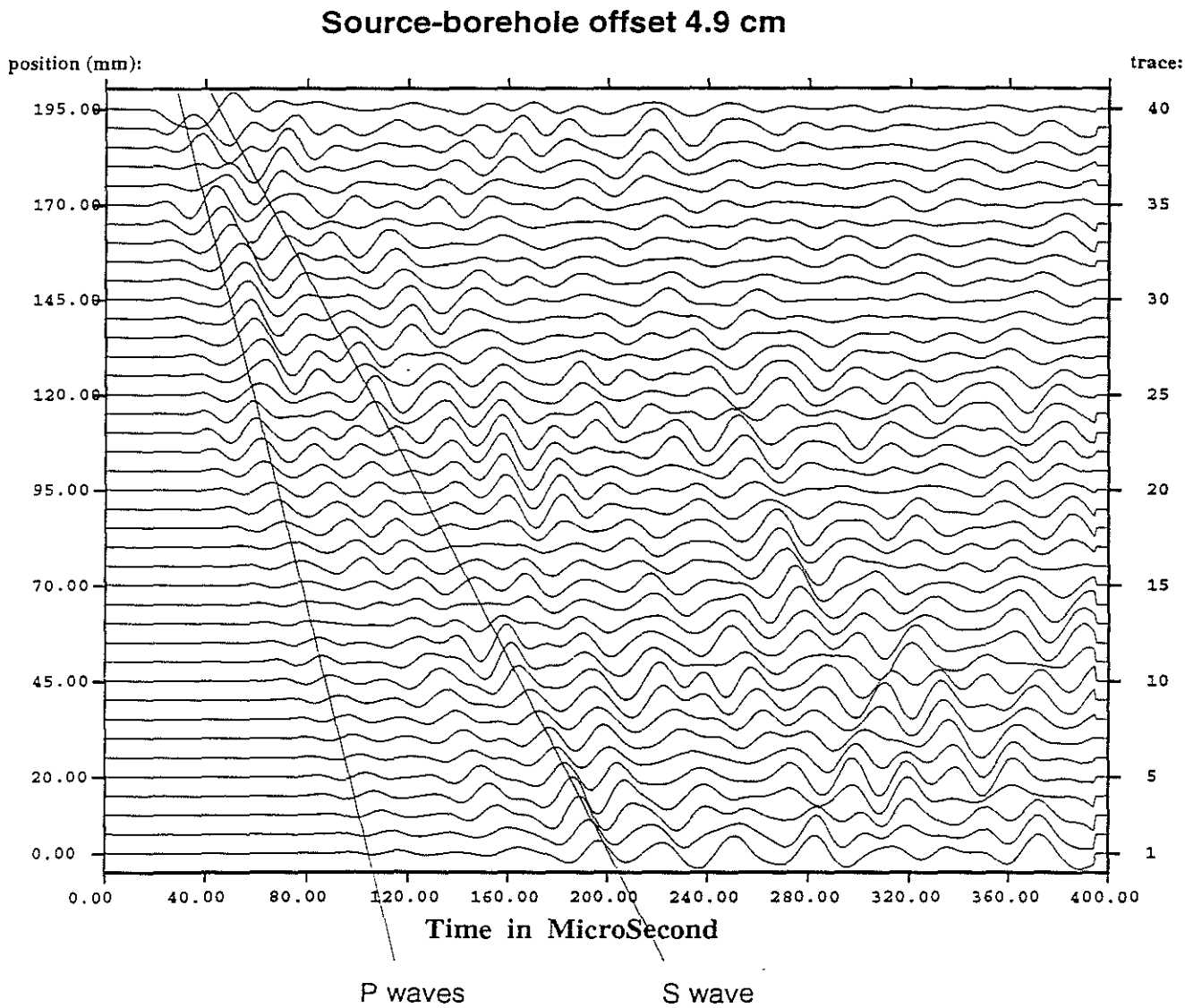

Figure 38: Measured pressure in the borehole fluid with the source-borehole offset 4.9 cm. The source frequency is centered at 50 kHz. The P and S waves are marked on the seismograms.

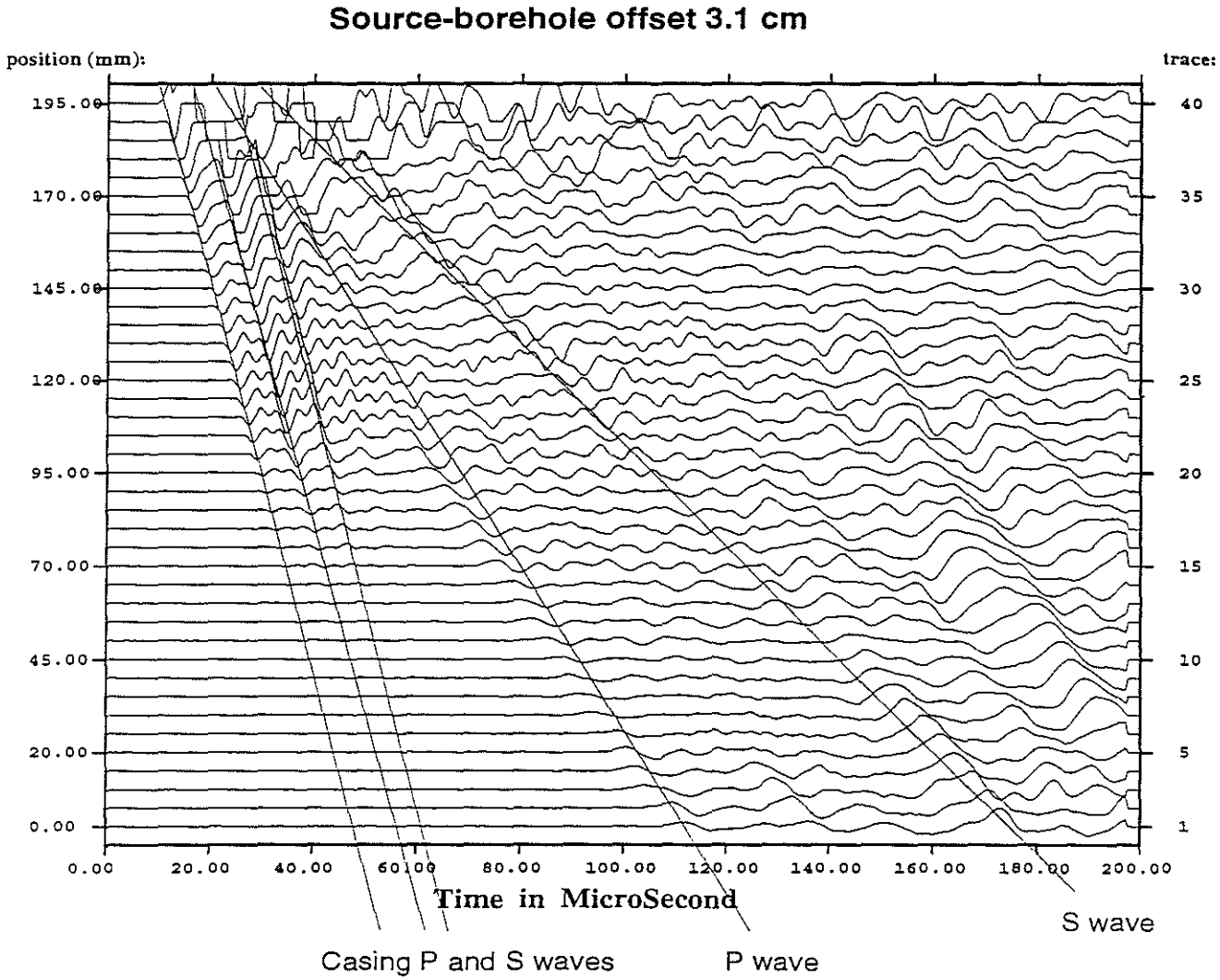

Figure 39: Measured pressure in the borehole fluid with the source-borehole offset 3.1 cm. The source frequency is centered at 100 kHz. The P and S waves, as well as the casing P and S waves, are marked on the seismograms.

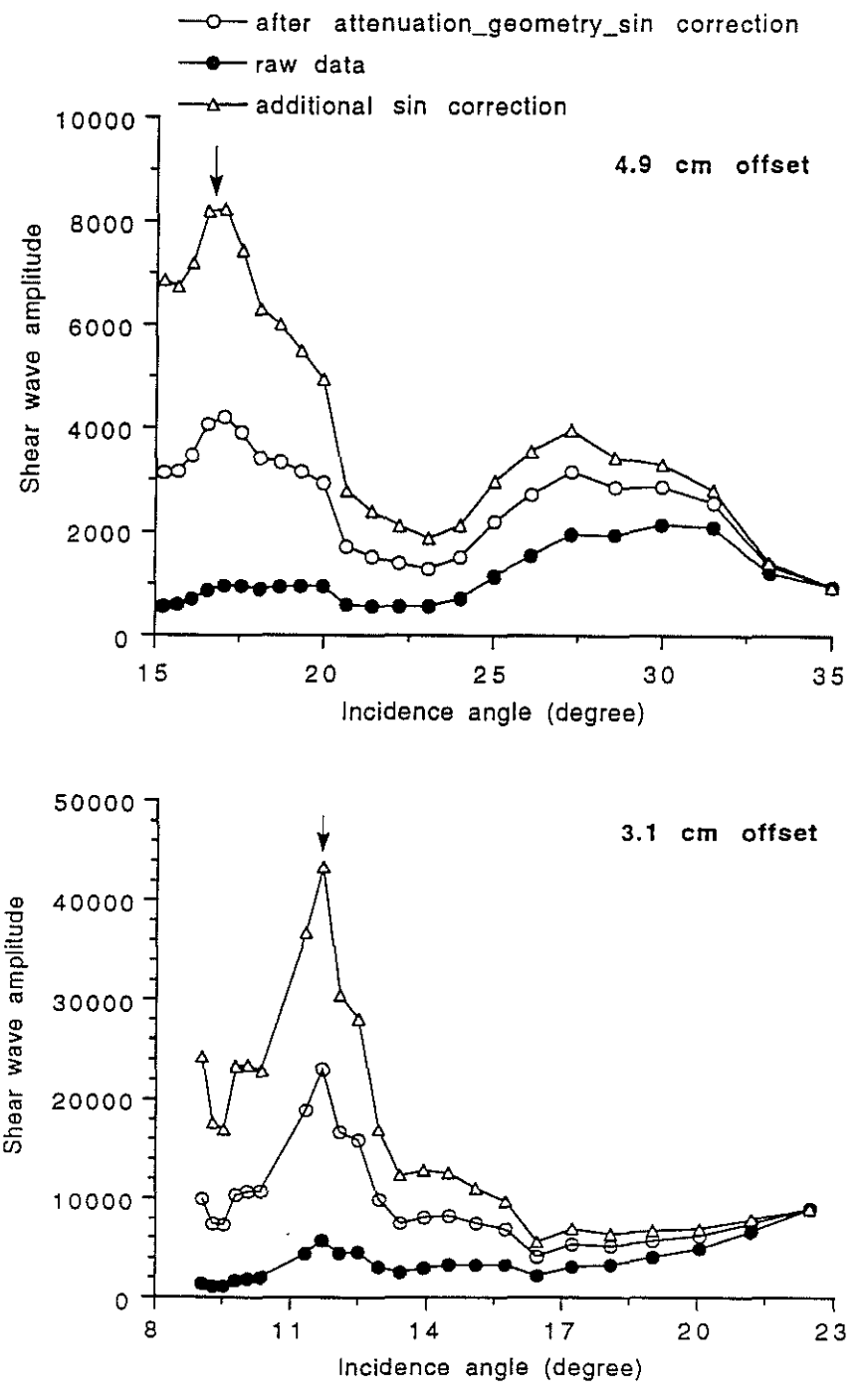

Figure 40: Shear wave amplitude versus the angle of incidence. The solid circle represents the raw data from the experiment. The open circle is that after attenuation, geometrical spreading, and radiation pattern ($\sin\delta$) correction. The open triangle is that after an additional $\sin\delta$ correction.